The Effect of the Packing Density on the Indentation Hardness of Cohesive-Frictional Porous Materials

by

Sophie Cariou

Diplômée de l'Ecole Polytechnique (2002)
Ingénieur de l'ENPC (2004)

Submitted to the Department of Civil and Environmental Engineering
in partial fulfillment of the requirements for the degree of

Master of Science in Civil and Environmental Engineering

at the

MASSACHUSETTS INSTITUTE OF TECHNOLOGY

June 2006

Signature of Author ....
Department of Civil and Environmental Engineering
May 12, 2006

Certified by ....
Franz-Josef Ulm
Professor of Civil and Environmental Engineering
Thesis Supervisor

Accepted by ....
Andrew J. Whittle
Chairman, Departmental Committee for Graduate Students

The Effect of the Packing Density on the Indentation Hardness of Cohesive-Frictional Porous Materials

by

Sophie Cariou

Submitted to the Department of Civil and Environmental Engineering
on May 12, 2006, in partial fulfillment of the
requirements for the degree of
Master of Science in Civil and Environmental Engineering

Abstract

Natural composites in general and sedimentary rocks in particular are highly heterogeneous materials which defy a straightforward implementation of the materials science paradigm of microstructure-properties-performance correlation. The application of nanoindentation to natural composites has provided the geomechanics community with a new versatile tool to test in situ phase properties and structures of geomaterials that cannot be recapitulated ex situ in bulk form. But it requires a rigorous indentation analysis to translate indentation data into meaningful mechanical properties. The development and implementation of such an indentation analysis for the strength properties of cohesive-frictional porous materials is the focus of this thesis. We report the development and implementation of a multi-scale indentation analysis based on limit analysis, which makes it possible to infer from an experimental hardness value and the solid's packing density the strength properties of the cohesive-frictional porous material. Making use of most recent advances in non-linear strength homogenization theory, we implement a homogenized cohesive Cam-Clay type elliptical strength criterion which takes into account the strength properties of the constituents (cohesion and friction), the porosity and the microstructure, into a yield design approach to indentation analysis. Making use of the strong duality of the lower and upper bound theorem, we identify the resulting upper bound problem as a Second-Order Conical optimization problem, for which advanced solvers such as MOSEK became recently available. The originality of our approach lies in the combination of finite element discretization and advanced optimization techniques, which is readily implemented in standard tools of computational mechanics, such as MATLAB. The upper bound yield design solutions are benchmarked against solutions from comprehensive elastoplastic contact mechanics finite element solutions and compared with lower bound solutions, which all show an excellent agreement. Furthermore, from a detailed parameter study based on intensive computational simulations, we show that it is possible to condense the indentation hardness-material properties relation of cohesive-frictional porous materials into a single hardness-packing density scaling relation. On this basis, it is possible to use the hardness-packing density scaling relation for reverse analysis of the strength parameters of cohesive-frictional solids from indentation. The procedure is illustrated for shale materials. From hardness values of six shale materials of different packing density and mineralogy, we deduce that the clay fabric in highly compacted shales is most likely a purely cohesive (friction-less) nano-granular material, having a uniaxial strength of roughly 440 MPa.

Thesis Supervisor: Franz-Josef Ulm
Title: Professor of Civil and Environmental Engineering

Contents

List of Figures

Acknowledgements

This work would have never been possible without the support of many people that I would like to thank. First of all, I want to express my deep thanks to Prof. Franz-Joseph Ulm who permitted me to live this wonderful experience at MIT. I am grateful to him for his enthusiasm about my work and his financial support throughout my Master. I would like to thank as well Yann who identified my optimization problem as a second order conic problem and Emilio who enabled my code to run much faster than expected. I can not think about these months here without remembering some faces: my labmates: Matthieu-Marina, Chris, Alberto-Carenina, Matt-Cara, Georgios-Angelina, Emilio, JongMin-Eunkiung; Maria and the geotech team; some friends: Thibault, Chia, Mihaï, Henry and Alexandre. From France, Raphaël shared my daily excitement about my work and my life here. His enthusiasm and support contributed to make my stay here very pleasant. Last, I am very thankful to my parents and my brother who always encourage me. They shared with delight my path in the US. This work was made possible by the Schoettler Scholarship Fund and I am very thankful to the GeoGenome Industry Consortium (G2IC).

Part I

General Presentation

Chapter 1

Introduction

Is it possible to break down natural composite material, such as shales, clays, clay-bearing sedimentary rocks, carbonates, sandstones, even salt rock down to a scale where rock mechanical characteristics no longer change from one type to another, and upscale ("nanoengineer") the behavior from the nanoscale to the macroscale of engineering rock behavior?

The question here raised is at the core of a new approach to geomechanics in experimental nano- and micromechanics of geomaterials, known as the GeoGenome project [1]. This thesis aims at contributing to this project with a particular focus on the assessment of strength properties of porous geomaterials by nanoindentation. This Chapter provides an introduction to the topic, research motivation and objectives, and an outline of this report.

1.1 Industrial Context

The strength properties of geomaterials in general and of sedimentary rocks in particular are of critical importance for many fields of oil and gas exploitation engineering, ranging from hydraulic fracturing and well bore stability to the appropriate choice of the drilling fluid chemistry and density and unwanted sand production phenomena. Measuring and predicting the strength properties is of utmost importance. Classically, strength properties are estimated using macroscopic triaxial testing methods. However, this classical technique requires expensive macroscopic material sampling often from very high depths. Furthermore, all rocks exhibit a high degree of heterogeneity, which makes it difficult to extrapolate strength values from one horizon to another.

Very recently, a new approach has been suggested to deal with the intrinsic diversity of earth materials. Coined the GeoGenome project [1], this approach aims at identifying a fundamental unit of material invariant behavior of sedimentary rocks. Once this scale is identified, it is possible to upscale the intrinsic material behavior from the nano-scale to the macro-scale, and quantify macroscopic diversity on the basis of a few material invariant properties. The work presented in this thesis is part of this 'genoming' effort of geomaterials.

1.2 Research Motivation and Objectives

One of the main experimental tools in the GeoGenome project is nanoindentation, that is the nano-scale deformation of a material surface by a rigid indenter[1]. The nanoscale mechanical contact approach overcomes two main restrictions of macroscopic testing: (1) it can be carried out on small material volumes; (2) it allows testing of in situ phase properties and structures of geomaterials that cannot be recapitulated ex situ in bulk form. Nanoindentation alone, however, does not directly provide a measurement of the material properties, but provides a snapshot of them embedded into the measured indentation data. Indeed, it requires an appropriate indentation analysis to translate indentation data into meaningful material properties.

This thesis deals with the indentation analysis of the hardness of porous materials. The hardness is obtained by dividing the applied load P by the projected contact area A_c (see Fig. 1-1):

$$H \overset{def}{=} \frac{P}{A_c} \tag{1.1}$$

Our aim is to relate this measured quantity to meaningful strength properties and morphology of porous materials.

The hardness of materials is a fundamental quantity used in Materials Science and Engineering for materials property characterization. For purely cohesive materials like metals, the

---

[1] A detailed description of this technique is given in Chapter 2.

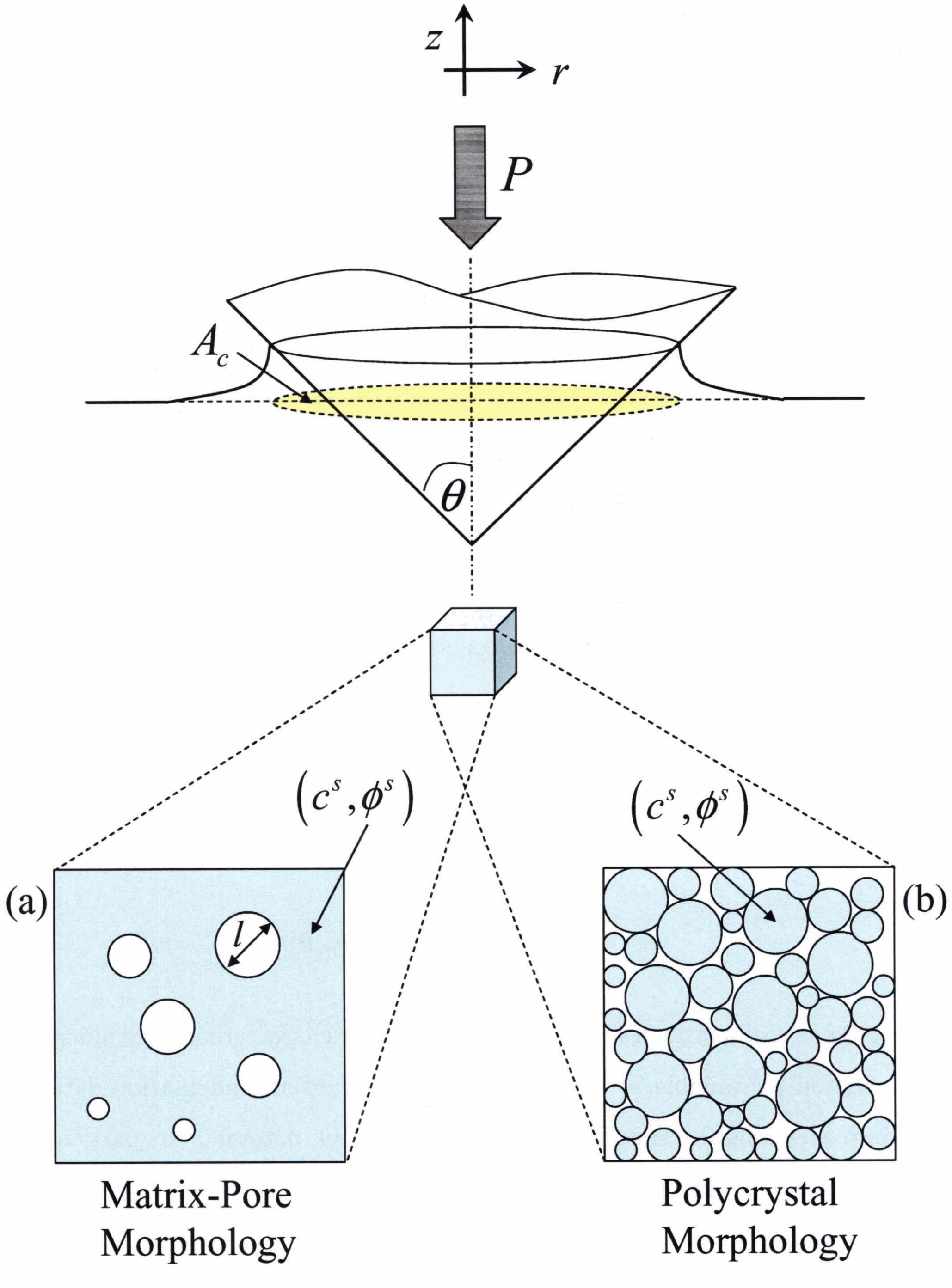

Figure 1-1: Schematic of an indentation test on a porous material. Two possible pore morphologies of an *rev* are displayed: (a) matrix pore morphology ($\eta_0 = 0$); (b) disordered polycrystal morphology ($\eta_0 = 0.5$).

rule-of-thumb is that the hardness is roughly three times the uniaxial yield strength of the material, i.e. $H/Y \approx 3$ [73]. This rule-of-thumb fails for cohesive-frictional materials for which it was recently recognized that the hardness-to-cohesion ratio depends as well on the friction angle ϕ and other parameters relating to the geometry of the indenter (for instance cone angle θ), i.e. $H/C = \mathcal{F}(\phi, \theta)$ [37]. However, those relations are restricted to monolithic material systems, and cannot be applied to *porous* materials, the class of materials composing the majority of natural composites, including shales, clays, clay-bearing sedimentary rocks, carbonates, sandstones, etc. This motivates the research presented in this thesis. More specifically, making use of recent progress in non-linear micromechanics [30] we seek for the relation between the indentation hardness (1.1) and the following properties characterizing the isotropic strength behavior of a two phase solid-pore composite (see Fig. 1-1):

1. Cohesion c^s and friction angle ϕ^s of the solid phase;
2. The porosity φ respectively the solid concentration or solid packing density $\eta = 1 - \varphi$;
3. The connectivity of the solid phase captured by a percolation threshold η_0, below which the porous material looses its mechanical performance.

Thus, we are interested in determining the following relation:

$$\frac{H}{c^s} = \mathcal{F}(\phi^s, \varphi = 1 - \eta, \eta_0, \theta) \tag{1.2}$$

where θ represents a dimensionless geometrical parameter characterizing the indenter geometry. Once this relation is available, it becomes possible to translate indentation data, namely the hardness, into meaningful strength properties of a porous material. In particular, it should enable us to answer the following two questions:

- If information about porosity and pore morphology (i.e. percolation threshold η_0) of a material is available, is it possible to deduce from hardness measurements the cohesion and friction angle of the solid phase? The answer to this question is of critical importance for indentation analysis of porous materials, providing a quantitative means to estimate from a nanoscale contact approach the in situ nano-strength properties of the solid phase of porous materials.

- If a large range of hardness measurements on materials of different compositions and porosities is available, is it possible to infer the link between composition, microstructure and mechanical properties of a class of materials, like shales? The answer to this question is of critical importance for the GeoGenome project. Indeed, it would put the problem of natural porous materials on par with other monolithic materials systems such as intermetallic alloys and ceramics and semiconductor materials.

1.3 Chosen Approach

To reach our goal, we break down the problem in three different tasks.

The first task consists of analyzing the micromechanics of strength properties of porous materials, and of translating those relations into a workable model for analyzing the composite strength behavior of porous materials on the basis of constituent properties (c^s, ϕ^s) and microstructure (φ, η_0). We will achieve this task by a combination of strength homogenization and yield design theory, to arrive at expressions of the dissipation potential of a porous material composed of a purely cohesive and a cohesive-frictional solid phase, captured by the Von-Mises and Drucker-Prager strength model, respectively. In addition, two limit cases of the microstructure of porous materials are considered, namely a matrix-pore inclusion morphology and a disordered polycrystal morphology (see Fig. 1-1).

The second task consists in the computational implementation of the yield design theory for the determination of the hardness-to-cohesion relation (1.2). In particular, we will focus on the implementation of the Upper Bound Limit Theorem of yield design as a non-linear minimization problem, combining the meanwhile classical discrete formulation of the Upper Bound Limit Theorem with second-order conical constraints that are solved with the solver MOSEK.

This computational implementation is put to work for the analysis of indentation tests of different cone angles θ. Normalized hardness-to-solid cohesion relations of the form (1.2) are determined through intensive computational simulations. The use of those relations for practical indentation analysis of porous materials is illustrated through the application to indentation data of shale materials of different mineralogy and packing density.

1.4 Thesis Outline

This report is divided in four parts:

Following this Introduction Chapter, the second Chapter of this first part provides an introduction to indentation testing and a review of existing indentation analysis of strength properties. This will be achieved by means of a dimensional analysis of the involved quantities, culminating in the derivation of the dimensionless relation (1.2) which is at the core of our investigation.

Part II of this thesis is devoted to the determination of this hardness-to-cohesion ratio for cohesive-frictional porous materials. It is composed of two Chapters: Chapter 3 starts out with a brief introduction to strength homogenization theory of porous composites composed of a cohesive or cohesive-frictional solid and a pore space. Using both the Lower and Upper Bound Limit Theorem, we show how this homogenized strength criterion can be put to work for indentation analysis. Chapter 4 is devoted to the computational mechanics implementation of the Upper Bound Theorem of Yield Design as a minimization problem for indentation analysis of the strength properties of a porous material. This will be achieved by identifying first the type of optimization problem, and by a reformulation of the problem that makes it possible to solve the minimization problem with advanced solver software.

Part III is devoted to the determination of the dimensionless relation (1.2) based on intensive computational simulations. In particular, Chapter 5 is devoted to the validation of the computational method developed in Part II, and also studies the sensitivity of the numerical results with regard to the mesh size. Chapter 6 presents a detailed parameter study of the different dimensionless numbers that affect the hardness-to-cohesion ratio (1.2), and summarizes the results in terms of characteristic curves that can be used for indentation analysis.

Finally, Chapter 7 in Part IV is devoted to the application of the method to shale materials, from which we provide estimates of the solid's cohesion c^s and friction angle ϕ^s, together with some preliminary conclusions regarding the morphological arrangement of this nano-granular material.

The main findings and contributions of this study are summarized in Chapter 8, which also suggests perspectives for future research.

1.5 Research Significance

The research presented in this thesis aims at contributing to the GeoGenome project, by providing an innovative means for the assessment of nano-strength properties of porous composites from indentation data. This assessment is of critical importance for both the identification of material invariant properties of such materials, and for the development of quantitative up-scaling rules that ultimately shall allow the prediction of macroscopic strength properties of geomaterials. In fact, the determination of nano-strength properties (c^s, ϕ^s) from nanoindentation provides for the first time access to properties of the solid phase of a porous material at the nanometer scale. Those values can directly be employed for the prediction of the strength domain of the porous material at larger scales, provided the pore volume fraction φ and the pore morphology, expressed for instance by the solid percolation threshold η_0, are known. Vice versa, if the strength properties are known, it is possible to identify the mechanical performance of porous materials in terms of strength-packing density relations and solid percolation thresholds. The tools developed in this thesis, therefore, contribute to materials science research of natural composites, that aims at correlating nano- and microstructure of porous materials with properties and performance. It is on this basis that we expect progress in nanotechnology to impact everyday engineering applications and society.

Chapter 2

Nanoindentation Technique and Indentation Analysis

The advent of instrumented indentation techniques has provided the mechanics community with an unprecedented opportunity to explore mechanical properties of materials at multiple length and force scales. Indeed, thanks to the self-similarity possible in indentation tests and the resulting mechanical response of the materials system, one single experimental technique is able to provide access to mechanical properties of materials from the nanoscale to the macroscale. Most of the developments in the last decade concentrated on indentation testing of metals, which are atomically cohesive materials. In contrast, natural composites, like shales, clays, clay-bearing sedimentary rocks, carbonates, sandstones, even salt rock, are porous materials that exhibit macroscopically a pronounced cohesive-frictional behavior. Following a short introduction to the nanoindentation technique, the aim of this Chapter is to review recent developments, strength and limitations of indentation methods for the determination of strength properties. Based on this review and dimensional analysis, we will define the focus of this study: the indentation hardness-to-solid cohesion ratio H/c^s of a porous material.

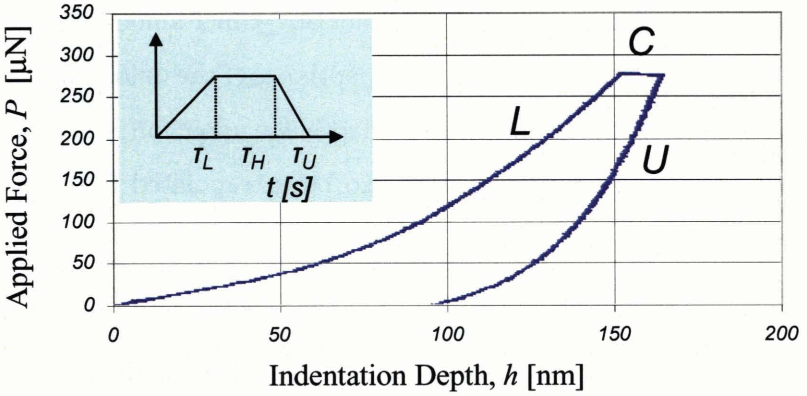

Figure 2-1: A typical $P-h$ curve obtained on a shale material (courtesy of C. Bobko, MIT): indentation load vs. indentation depth. L = loading phase, C = creep phase, U = unloading phase.

2.1 Nanoindentation: Measured and Derived Quantities

2.1.1 $P-h$ Curve

It is now well established that the response of a material upon the reversal of contact loading provides access to the elastic properties of the intended material (for recent review see [56] and [17]). The indentation technique consists of establishing contact between an indenter of known geometry and mechanical properties (typically diamond) and the indented material for which the mechanical properties are of interest, and subsequently acquiring the continuous change in penetration depth h as a function of increasing indentation load P ($P-h$ curve, see Fig.2-1). Typically, the extraction of mechanical properties is achieved by applying a *continuum scale* mechanical model to derive two quantities, indentation hardness H and indentation modulus M:

$$H \overset{def}{=} \frac{P_{\max}}{A_c} \tag{2.1}$$

$$S = \frac{dP}{dh}|_{h=h_{\max}} \overset{def}{=} \frac{2}{\sqrt{\pi}} M \sqrt{A_c} \tag{2.2}$$

All quantities required to determine H and M are directly obtained from the $P-h$ curve, with the exception of the projected area of contact A_c. Chief among those are the maximum applied force $P_{\max}$ and corresponding maximum depth $h_{\max}$, the unloading indentation stiffness $S=(dP/dh)_{h=h_{\max}}$, and residual indentation depth h_f upon full unloading of the material surface (Fig. 2-1). The contact area A_c can also be extrapolated from the maximum depth $h_{\max}$ [55].

It should be noted that both hardness and indentation modulus are not material properties per se, but rather 'snapshots' of respectively the strength response and the elastic response of the indented material. This will be discussed in Section 2.2 below.

2.1.2 Self-Similarity of the Indentation Test

Spherical, conical and pyramidal indenters are the most common shapes used in practice[1]. In this thesis, we will focus on sharp indentation testing with conical or pyramidal indenters. The Vickers indenter is a four-sided pyramid with a semi-vertical angle of 68° (Fig.2-2). The Berkovich indenter which is commonly employed for small scale testing is a three-sided pyramid and was constructed with a semi-vertical angle of 65.3°, such as to maintain the same area-to-depth ratio as the Vickers indenter. In contrast to the four-sided pyramids, Berkovich indenters have the advantage that their three edges are more easily manufactured to meet at a point. A cube corner indenter has the same geometry as a Berkovich indenter but with a sharper face angle of 90°.

One key feature of the analysis of pyramidal or conical indentation is the self-similarity of Hertz-type contact problems. The conditions under which frictionless Hertz type contact problems possess classical self-similarity were stated by Borodich [6]; and include:

1. The shape of the indenter is described by a homogeneous function whose degree is greater or equal to unity. Using a Cartesian coordinate system $Ox_1x_2x_3$ whose origin O is at the indenter tip and x_3 is the orientation of the indentation, the shape of the indenter (height) is defined by:

$$f\left(\lambda x_1,\lambda x_2\right)=\lambda^d f\left(x_1,x_2\right) \tag{2.3}$$

---

[1] Inspired by the presentation of G. Constantinides in his Ph.D-Thesis [23].

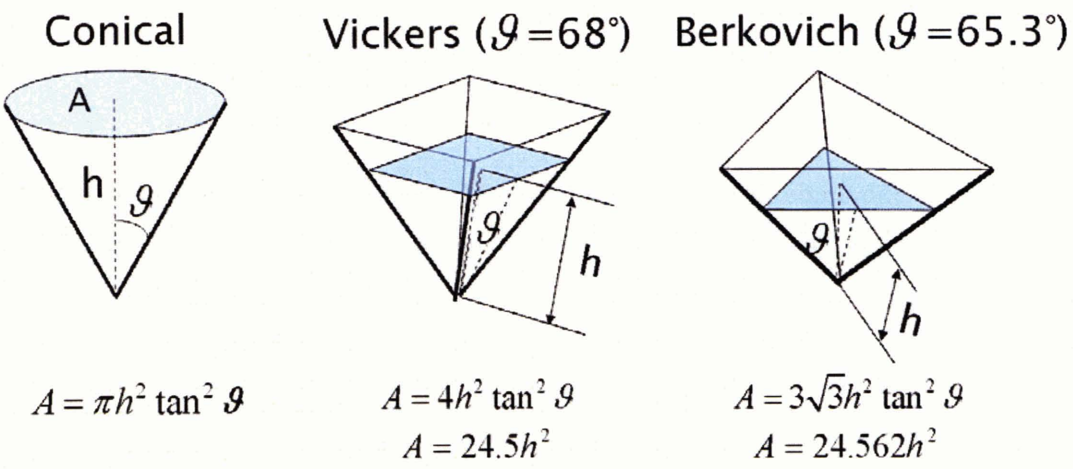

Figure 2-2: Geometrical caracteristics of conical, Vickers and Berkovich indenters (from [23]).

for arbitrary positive λ. Here d is the degree of the homogeneous function f; in particular $d = 1$ for a cone and $d = 2$ for the elliptic paraboloid considered by Hertz. Such axisymmetric indenters can be described by monomial functions of the form (first introduced by Galin, according to Borodich and Keer [7]):

$$f = f\left(x_1 = r\cos\theta, x_2 = r\sin\theta\right) = Br^d \tag{2.4}$$

where B is the shape function of the indenter at unit radius. For a conical indenter ($d = 1$), having a semi-vertical angle θ; $B = \cot\theta$. For a spherical indenter of radius R, $d = 2$ and $B = 1/\left(2R\right)$. The previous expression was recently extended to indenters of non-axi-symmetric shape, such as pyramidal indenters that are frequently employed in depth-sensing indentation tests [6]:

$$f = B\left(\phi\right) r^d \tag{2.5}$$

where $B\left(\phi\right)$ describes the height of the indenter at a point $\left(\phi, r = 1\right)$. For a three-sided pyramid, $d = 1$, and making use of the triple symmetry:

$$B(\phi) = \cot \vartheta \sin(\pi/6 + \phi) \tag{2.6}$$

where ϑ is the angle in vertical cross-sections. For a Berkovich indenter, having a face angle of 115.13°, $\vartheta = 65.3°$; and for a cube corner indenter of 90° face angle, $\vartheta = 35.26°$ (see Tab. 2.1).

2. The operator of constitutive relations F for the indented material is a homogeneous function of degree κ with respect to the components of the strain tensor $\boldsymbol{\varepsilon}$ (respectively the strain rate-tensor $\mathbf{d}$):

   $$F(\lambda\boldsymbol{\varepsilon}) = \lambda^{\kappa} F(\boldsymbol{\varepsilon}) \tag{2.7}$$

   A linear elastic law satisfies this relation since $\kappa = 1$; as does any nonlinear secant elastic formulation of the form $\boldsymbol{\sigma} = \mathbb{C}(\boldsymbol{\varepsilon}) : \boldsymbol{\varepsilon}$ for which the secant elastic stiffness tensor satisfies:

   $$\mathbb{C}(\lambda\boldsymbol{\varepsilon}) = \lambda^{\kappa-1}\mathbb{C}(\boldsymbol{\varepsilon}) \tag{2.8}$$

   A similar reasoning applies to the dissipation function $\pi(\lambda\mathbf{d}) = \lambda^{\kappa}\pi(\mathbf{d})$ applied in yield design solutions, as we will see in forthcoming Chapters.

Then provided the homogeneity of material properties and that the stress-strain relation remains the same for any depth of indentation, the whole load-displacement curve in a depth-sensing test can be scaled by [6]:

$$\frac{P}{P_1} = \left(\frac{h}{h_1}\right)^{\frac{2+\kappa(d-1)}{d}} ; \frac{h}{h_1} = \left(\frac{A_c}{A_1}\right)^{d/2} \tag{2.9}$$

It is important to note that the projected contact area A_c – in contrast to the load P – is not affected by the constitutive relation (coefficient κ). In return, from a straightforward application of (2.1), the hardness scales with the indentation depth according to:

$$\frac{H}{H_1} = \left(\frac{h}{h_1}\right)^{\frac{\kappa(d-1)}{d}} \tag{2.10}$$

	Projected Area	Semi-vertical angle, ϑ	Equivalent cone angle θ
Berkovich	$3\sqrt{3}h^2\tan^2\vartheta$	65.3°	70.32°
Vickers	$4h^2\tan^2\vartheta$	68.0°	70.32°
Cube corner	$3\sqrt{3}h^2\tan^2\vartheta$	35.26°	42.28°
Cone	$\pi h^2\tan^2\vartheta$	θ	θ

Table 2.1: Geometrical relations between projected area and equivalent half-apex cone angle.

In the case of conical and ideal (sharp) pyramidal indenters, for which $d = 1$, we readily find that the load-displacement relation is scaled by $P \propto h^2$ and that the hardness is a constant over the loading process. That is,

$$H \overset{def}{=} \frac{P_1}{A_1} = \frac{P_2}{A_2} = ... = \frac{P}{A_c} \tag{2.11}$$

Finally, the degree of the homogeneous shape function is $d = 1$ for both the three-sided pyramidal (Berkovich, corner cube) indenters and for the conical indenter. For this reason, it is common practice to consider, instead of the original three-dimensional pyramidal shape, an equivalent cone of revolution. The projected contact area of this cone w.r.t. to depth is the same as that of the real indenter; that is, according to (2.9):

$$A(h) = C_1 h^2 = \pi (h \tan\theta)^2 \Longrightarrow \tan\theta = \sqrt{\frac{C_1}{\pi}} \tag{2.12}$$

where C_1 is a constant characterizing the specific pyramidal indenter, and θ is the equivalent semi-apex cone angle (see Tab. 2.1). Using Eq. (2.12), the flat Berkovich indenter ($\vartheta = 65.3°$), for which $C_1 = 24.56$, can be assimilated to an equivalent cone of semi-apex angle $\theta = 70.32°$; and a cube corner indenter ($\vartheta = 35.26°; C_1 = 2.598$) to one with $\theta = 42.28°$. The area-to-depth relations for different sharp indenter shapes are summarized in Table 2.1.

This correspondence is very helpful since the use of a conical indenter, instead of the full 3-D three-sided pyramidal indenter, allows us to formulate the sharp indentation problem as a 2-D axisymmetric problem, which is much more computationally efficient.

2.2 Indentation Analysis

From now on, we will focus on the indentation analysis of conical indentation[2]. Indentation analysis aims at linking indentation data to meaningful material properties. As we have already noted, both the contact stiffness and the hardness, as defined by (2.2) and (2.1) are not material properties. This Section reviews some tools of *continuum* indentation analysis.

2.2.1 Contact Stiffness and Indentation Modulus

The investigation of the link between the unloading slope S and the elasticity properties of the indented material is recent[3], thanks to the development of depth sensing indentation techniques which provide a continuous record of the $P-h$ curve during loading and unloading in an indentation test. The contact stiffness $S=(dP/dh)_{h=h_{\max}}$ gives a measure of the material elastic response, as Eq. (2.2) shows, which is also known as Bulychev-Alekhin-Shoroshorov (BASh) equation [14] or Sneddon's solution [68]. It originates from the analytical solution of Heinrich Hertz (1882) [42] of the linear contact problem of two spherical surfaces (with different radii and elastic constants), which provides a means of evaluating the contact area of indentation, and which forms the basis of much experimental and theoretical work in indentation analysis based on contact mechanics. In 1885, Boussinesq published a solution for the problem of contact between a solid of revolution and an elastic continuum [9], of which the flat punch solution is the best known. In the first half of the 20th century, the elastic solutions were extended to other shapes of indenters by Love [51], Galin [35], and Harding and Sneddon [41]. Subsequently, Sneddon [68] derived general relationships among load, displacement and contact area for a punch of arbitrary axisymmetric shape. Much of the later developments [28][55] rely on these general solutions and solution methods, which constitute the basis for what is now known as (elastic) indentation analysis; that is, the translation of indentation data into meaningful elastic

---

[2] Inspired by the presentation of G. Constantinides in his Ph.D-Thesis [23].

[3] Depth sensing indentation techniques have been conceptualized by Tabor and coworkers [73], and its implementation down to the nanoscale appears to have developed first in the former Soviet Union from the mid 1950s on throughout the 1970s (for a review of the chronology of events, see, for instance, [7]). This instrumented indentation approach received considerable attention world-wide, ever since Doerner and Nix [28] and Oliver and Pharr [55] in the late 1980s and early 1990s, also identified this technique for analysis and estimation of mechanical properties of materials, such as microelectronic thin films for which few other experimental approaches were available.

mechanical properties. In fact, the indentation modulus M that is determined from the BASh equation (2.2) can be linked to the elastic constants of the indented material by applying a linear elastic model to the data. In the isotropic case, M reduces to the plane-stress elastic modulus,

$$M = \frac{E}{1-\nu^2} = 4\mu\frac{3k+\mu}{3k+4\mu} \tag{2.13}$$

where E is the Young's modulus, ν the Poisson's ratio; μ is the shear modulus and k the bulk modulus of the indented *homogeneous* isotropic material. In contrast to the isotropic case, for which the indentation modulus is the same for all directions of indentations, the indentation modulus of anisotropic materials depends on the direction of indentation. For instance, in the case of a transverse isotropic material, the indentation modulus obtained by indentation in the axis $x3$ of symmetry relates to the five independent C_{ijkl} coefficients of the material in the following way [32][40]:

$$M_3 = 2\sqrt{\frac{C_{31}^2 - C_{13}^2}{C_{11}}\left(\frac{1}{C_{44}} + \frac{2}{C_{31}+C_{13}}\right)^{-1}} \tag{2.14}$$

In turn, for indentation normal to the axis of material symmetry (direction $x1$ or $x2$) the indentation modulus reads [25]:

$$M_1 = \sqrt{\frac{C_{11}^2 - C_{12}^2}{C_{11}}\sqrt{\frac{C_{11}}{C_{33}}}\,M_3} \tag{2.15}$$

where we employ the reduced notations $C_{33} = C_{3333}, C_{13} = C_{1133} = C_{3311}$, $C_{31} = \sqrt{C_{11}\,C_{33}} > C_{13}$ and $C_{44} = C_{2323} = C_{1313}$.

2.2.2 Indentation Hardness

The indentation hardness is defined as the maximum applied force P_{max} divided by the projected contact area A_c (see Eq. (2.1)). In contrast to the contact stiffness, hardness measurements, therefore, do not require a continuous record of the indentation depth. This may explain why hardness has a much longer history in Materials Science than the contact stiffness. Indeed, the very concept of 'hardness' can be found as early as in the 18th century in the works of several prominent mineralogists: Réaumur (1683-1757), Haüy (1743-1822) and Mohs (1773-1839). Williams [81] credits the French Scientist René Reamur (1683–1757) as the father of hardness measurements, which served from this early time on as a tool for classification of materials and standardization of products. The application of indentation methods to assess material properties can be traced back to the work of the Swedish engineer Brinell (1849–1925). Pushing a small ball of hardened steel or tungsten carbide against the surface of the specimen, Brinell empirically correlated the shape of the permanent impression with the strength of metal alloys [10]. The merits of Brinell's proposal were quickly appreciated by contemporaries: Meyer, O'Neill, and Tabor suggested empirical relations to transform indentation data into meaningful mechanical properties [73]. These early studies concentrated on the evaluation of hardness of metals and on the link of hardness with strength properties. Tabor, from slip-line field solution for indentation in a rigid-plastic solids by a frictionless rigid wedge, suggested a hardness vs. yield stress relationship of the form $H/Y = 3$ [72]. This relation got under scrutiny by several researchers for elastic-perfectly plastic solid (see discussion in [46]) and more recently for work-hardening materials (see discussion in [17]), which lead to the conclusion that hardness is not a material property, but rather a snapshot of materials mechanical properties and indenter geometry dependent. These conclusions not only hold for cohesive materials (of the Von-Mises or Tresca-type), but as well for cohesive-frictional materials [37].

Given the prominent role the indentation hardness will play in our investigation, it is instructive to elucidate the meaning of hardness by means of a dimensional analysis of a conical indentation test on a homogeneous elastic perfectly plastic material halfspace (see Fig. 2-3). The analysis presented below is due to Ganneau et al. [37]. The two dependent quantities of interest that define the hardness are the force P and the projected contact area $A_c = \pi a^2$, where $a = h_c \tan\theta$ is the contact radius, and h_c is the contact depth. These two dependent quantities depend on the properties of the elastoplastic cohesive-frictional material (stiffness C_{ijkl}, cohesion C, friction angle ϕ), the indentation geometry (which in the case of conical

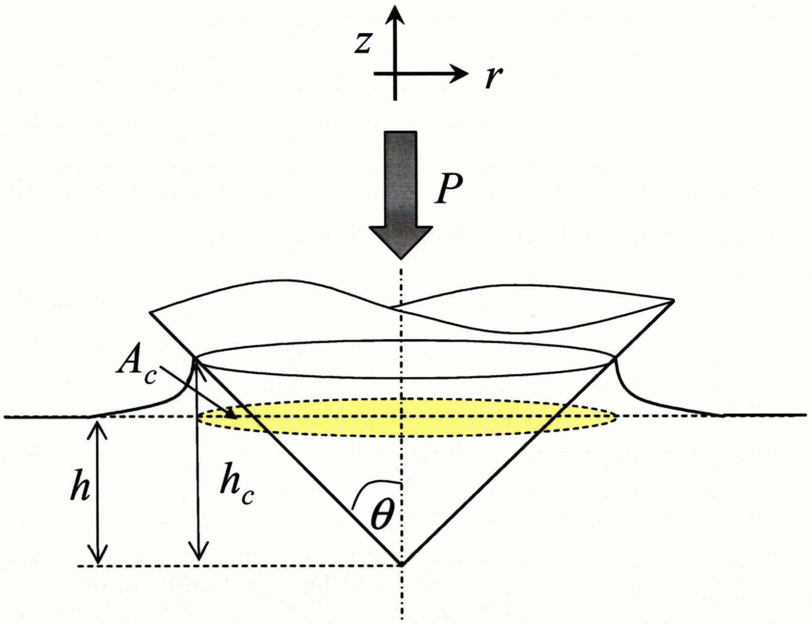

Figure 2-3: Schematic of a conical indentation test.

indentation reduces to the half-apex angle θ), and the rigid indentation depth h:

$$P = f\left(C_{ijkl}, C, \phi, \theta, h\right) \tag{2.16a}$$

$$A_c = g\left(C_{ijkl}, C, \phi, \theta, h\right) \tag{2.16b}$$

From a straightforward application of dimensional analysis (or more precisely the Pi-Theorem [3]) to relations (2.16), it is readily found that the two dimensionless relations,

$$\frac{P}{Ch^2} = \Pi_\alpha\left(\frac{C_{ijkl}}{C}, \phi, \theta\right) \tag{2.17a}$$

$$\frac{A_c}{h^2} = \Pi_\beta\left(\frac{C_{ijkl}}{C}, \phi, \theta\right) \tag{2.17b}$$

define a unique third dimensionless relation, the hardness-to-cohesion ratio as a unique function of the stiffness-to-cohesion ratio, the friction angle ϕ and the half-apex angle θ:

$$\frac{H}{C} = \frac{\Pi_\alpha}{\Pi_\beta} = \mathcal{H}\left(\frac{C_{ijkl}}{C}, \phi, \theta\right) \tag{2.18}$$

Relation (2.18) has been extensively explored for elastoplastic cohesive materials ($\phi = 0$), with and without strain hardening (see review in [17]). In particular, it has been shown, that the $H/C-$ratio for cohesive materials, for which $(C_{ijkl}/C)^{-1} \rightarrow 0$, comes close to Tabor's 1948 suggestion (noting that $Y = 2c$ for a Tresca material):

$$\frac{H}{Y} = \frac{H}{2C} = \frac{1}{2}\mathcal{H}\left(\frac{C_{ijkl}}{C} \rightarrow \infty, \phi = 0, \theta\right) \simeq 2.8 \tag{2.19}$$

It is worthwhile to note that $(C_{ijkl}/C)^{-1} \rightarrow 0$ comes close to the assumption of yield design approaches, which can be found early on in the indentation literature. For instance, Lockett [50] and Chitkara and Butt [18] developed yield design solutions for conical indentations in cohesive rigid-plastic solids (without and with friction at the indenter-material interface). More recently, using the Upper Bound Theorem of Yield Design, Ganneau et al. [37] determined the hardness-to-cohesion relations for conical indentation into a cohesive-frictional material of the Mohr-Coulomb type:

$$\frac{H}{C} = \mathcal{H}\left(\frac{C_{ijkl}}{C} \rightarrow \infty, \phi, \theta\right) \tag{2.20}$$

Figure 2-4 displays the H/C ratio as a function of the friction angle for two indenter geometries, the Berkovich indenter corresponding to an equivalent cone half-angle of $\theta_B = 70.32°$, and a Cube Corner corresponding to an equivalent cone half-angle of $\theta_{CC} = 42.28°$. An interesting observation is that the H/C value for small friction angles comes very close to the value given in (2.19) for a purely cohesive material (for a Tresca material), i.e. $H/C = 2H/Y \simeq 5.6$. However, as the friction angle increases, we observe a strong deviation from this 'rule-of-thumb' value, generally admitted for metallic materials. In fact, internal friction kinematically impedes the 45° slip lines commonly observed for frictionless materials and as a consequence increases the plastic yield volume and thus the overall dissipation capacity of the system, which translates into a higher hardness value of cohesive-frictional materials. Furthermore, based on the observation that the activation of internal friction gives rise to a strong dependence of the H/C on the cone half-angle θ, Ganneau et al. [37] propose a Dual-Indentation technique based on the ratio of

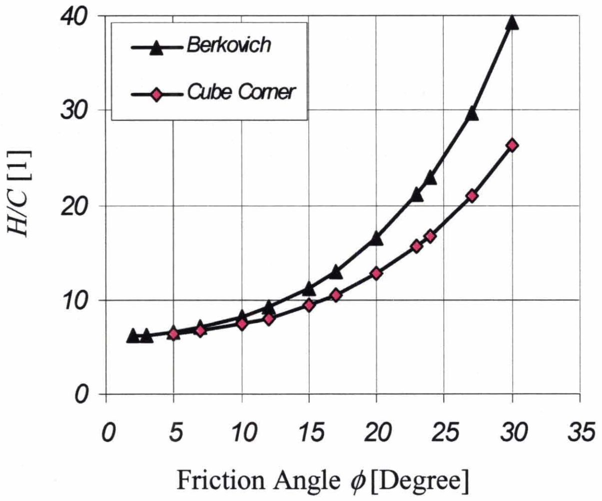

Figure 2-4: Upper bound solutions for the hardness-to-cohesion ratio for two conical indenter geometries: Berkovich indenter ($\theta_B = 70.32°$) and Cube Corner indenter ($\theta_{CC} = 42.28°$) (Data from [37]).

two hardness measurements:

$$\frac{H_B}{H_{CC}} = \frac{\mathcal{H}(\phi, \theta_B = 70.32°)}{\mathcal{H}(\phi, \theta_{CC} = 42.28°)} \tag{2.21}$$

Figure 2-5 displays the hardness ratio for the Berkovich and Corner-Cube indenters as a function of the friction angle in the interval $\phi \in [5°, 30°]$. As expected from the dimensionless relation (2.20), there exists a unique relation between the hardness ratio H_B/H_{CC} and the friction angle, which provides a means of assessing ϕ from the contrast in hardness between a Berkovich indentation test and a Cube Corner indentation test. While small for very small friction angles, the hardness ratio becomes significant for greater friction angles, for which the ratio appears to increase almost linearly with the friction angle in the interval considered. Once the friction angle is determined, it is possible to determine the cohesion from the H/C curves displayed in Figure 2-4.

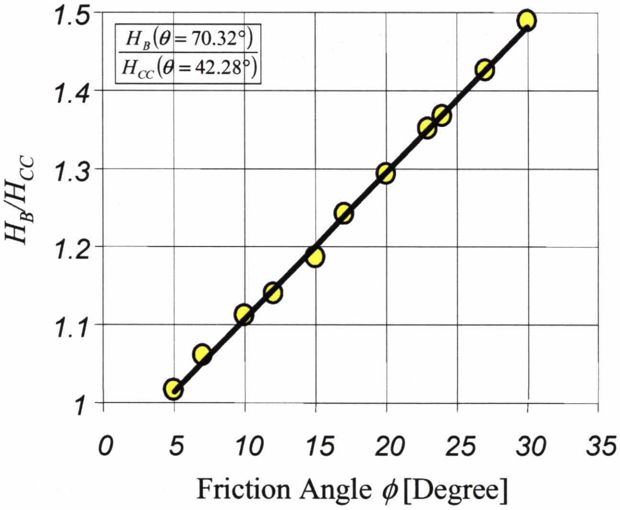

Figure 2-5: Hardness-ratio (Berkovich / Cube Corner) vs. friction angle (from [37]).

2.2.3 Limitations of Existing Tools of Indentation Analysis

The existing models employed in indentation analysis are restricted to monolithic systems, and little has been reported for indentation on heterogenous materials, a category composing the majority of natural solids, including shales, clays, clay-bearing sedimentary rocks, carbonates, sandstones, etc. Indeed, the application of relations (2.13) to (2.20) is based on two assumptions:

1. The representative elementary volume (*rev*) satisfies the separation of scale condition:

$$d \ll \mathcal{L} \ll h \tag{2.22}$$

   where $\mathcal{L}$ is the characteristic size of the *rev*, which must be much greater than the size of the largest heterogeneity of size d contained in the *rev*; and much smaller than the indentation depth h, which defines the order of length magnitude of the strain gradient variation in the microstructure induced during an indentation test.

2. The behavior of the indented halfspace is composed of a monophasic homogeneous mate-

rial defined by spatially invariant material properties; that is:

$$\forall \underline{x};\ \left(C_{ijkl}\left(\underline{x}\right), C\left(\underline{x}\right), \phi\left(\underline{x}\right)\right) = const \tag{2.23}$$

Those two assumptions impose severe restrictions on the applicability of the indentation technique for heterogeneous materials. The following section shows some recent extension of the nanoindentation technique for heterogeneous materials in general, and particularly for materials in which the dominating heterogeneity is the pore space in between a solid matrix or solid particles. It is on this basis that we will define the research focus of this thesis.

2.3 Indentation Analysis of Heterogeneous Materials

Recent extensions to continuum indentation analysis can be classified as follows:

- Thin-Film Indentation Analysis;
- Statistical Indentation Analysis of Multiphase Materials (Grid-Indentation Technique);
- Multi-scale Indentation Analysis.

2.3.1 Thin-Film Indentation Analysis

Indentation on thin films is one of the most popular current applications that aim at overcoming the limitations of classical continuum indentation analysis based on the infinite half-space model. The heterogeneity is due to the presence of a thin film of thickness t on a (infinite) substrate of known mechanical properties. In order to determine the indentation properties (M_f, H_f) of the thin film, the majority of thin-film models rely on phenomenological arguments or finite element simulations to subtract from the overall (or effective) indentation properties (M_{eff}, H_{eff}), extracted from an indentation test by means of Eqs. (2.2) and (2.1) the substrate effects (M_s, H_s):

$$M_{eff} = M_f + (M_f - M_s)\,\mathcal{I}_M \tag{2.24a}$$

$$H_{eff} = H_f + (H_f - H_s)\,\mathcal{I}_H \tag{2.24b}$$

where $\mathcal{I}_M$ and $\mathcal{I}_H$ are weight functions for stiffness and hardness, which depend on the indentation depth-to-film thickness ratio, h/t. As $\mathcal{I}_M \rightarrow 0$ and $\mathcal{I}_H \rightarrow 0$, the effect of the substrate is eliminated. Several models have been proposed in the literature to estimate the weighting functions for thin-film stiffness [38], [47], [82], [49], [60], [16] and thin-film hardness [13], [5], [31]. This type of approach extends the domain of application of indentation to problems where the size of the heterogeneity (here thin film thickness) is of a similar order of the indentation depth, thus overcoming the restriction of strict scale separability (2.22). On the other hand, the approach is restricted to layered material systems for which the size of the heterogeneity is known, and does not cover random heterogeneous material systems.

2.3.2 Statistical Indentation Analysis of Multiphase Materials (Grid Indentation Technique)

Indentation on multiphase materials became recently popular in the particular context of indentation on cementitious materials [21], [22], which culminated in the development, validation and implementation of the so-called 'grid-indentation technique' [23], [24]. The experimental basis of this method is a large series of indentation tests carried out on a surface grid (grid indentation technique). The indentation depth is chosen in a way so to satisfy in an average sense the scale separability condition (2.22), allowing for the application of the tools of continuum indentation analysis. Each indentation test is considered a single statistical event, and the mechanical properties extracted from continuum indentation analysis are considered as random variables. Those data are then analyzed by deconvoluting the empirical frequency densities or response distributions of the mechanical indentation properties, $x = M, H$, by means of a theoretical theoretical probability density function (PDF):

$$\begin{gathered}\text{For } x = (M, H) \text{ find } (\mu_J, s_J, f_J) \text{ from } \min \frac{1}{m} \sum_{i=1}^{m} \left(P_i - P\left(x_i\right)\right)^2 \\ \text{subjected to:} \\ \sum_{J=1}^{n} f_J = 1\end{gathered} \tag{2.25}$$

where μ_J, s_J are the mean value and standard deviation of $x = M, H$ of phase $J = 1, n$, and f_J is the volume fraction of this phase present in the multiphase material; P_i is the observed value of the experimental frequency density; m is the number of intervals (bins) chosen to construct the histogram, and $P(x_i)$ is the value of the theoretical probability density function at point x_i (assumed to be Gaussian):

$$P(x_i) = \sum_{J=1}^{n} \frac{f_J}{\sqrt{2\pi s_J^2}} \exp\left(-\frac{(x_i - \mu_J)^2}{2s_J^2}\right) \tag{2.26}$$

Figure 2-6 illustrates this deconvolution technique for the indentation modulus M and hardness H obtained from 300 indentation tests on a shale material operated to maximum indentation force of $P_{\max} = 285\,\mu\mathrm{N}$ and maximum indentation depths of $h_{\max} = 102 \pm 39\,\mathrm{nm}$. As the figures show, two characteristic phases can be identified mechanically at this scale in terms of mean values, standard deviations and volume fractions. We will come back to this technique in Chapter 8 devoted to the nano-strength properties of shale materials.

2.3.3 Multi-Scale Indentation Analysis

Multi-scale indentation analysis incorporates into the indentation analysis information about the microstructure of the indented material. Similar to the thin-film indentation analysis, it considers the indentation properties as effective or composite material properties that are functions of the constituent properties and their morphologies that manifest themselves at a scale situated below the characteristic scale of nanoindentation. With a focus on porous material, Ulm et al. [78] and Constantinides and Ulm [24] determined the effective indentation modulus from application of the tools of continuum micromechanics [83], [30] for:

- An isotropic matrix-pore morphology, for which the matrix remains continuous for the entire solid concentration range $\eta = 1 - \varphi \in [0, 1]$ [78]:

$$\frac{M}{m^s} = \frac{1}{4} \frac{\eta (8 + 9r^s) \left(32 + 300r^s + 207 (r^s)^2 - 3\eta r^s (56 + 33r^s)\right)}{(3r^s + 1) (24r^s - 15\eta r^s + 8) (20 + 15r^s - 6\eta (2 + r^s))} \tag{2.27}$$

where $r^s = k^s/\mu^s = 2(1 + \nu^s)/3(1 - 2\nu^s) > 0$ is the solid's bulk-to-shear modulus ratio,

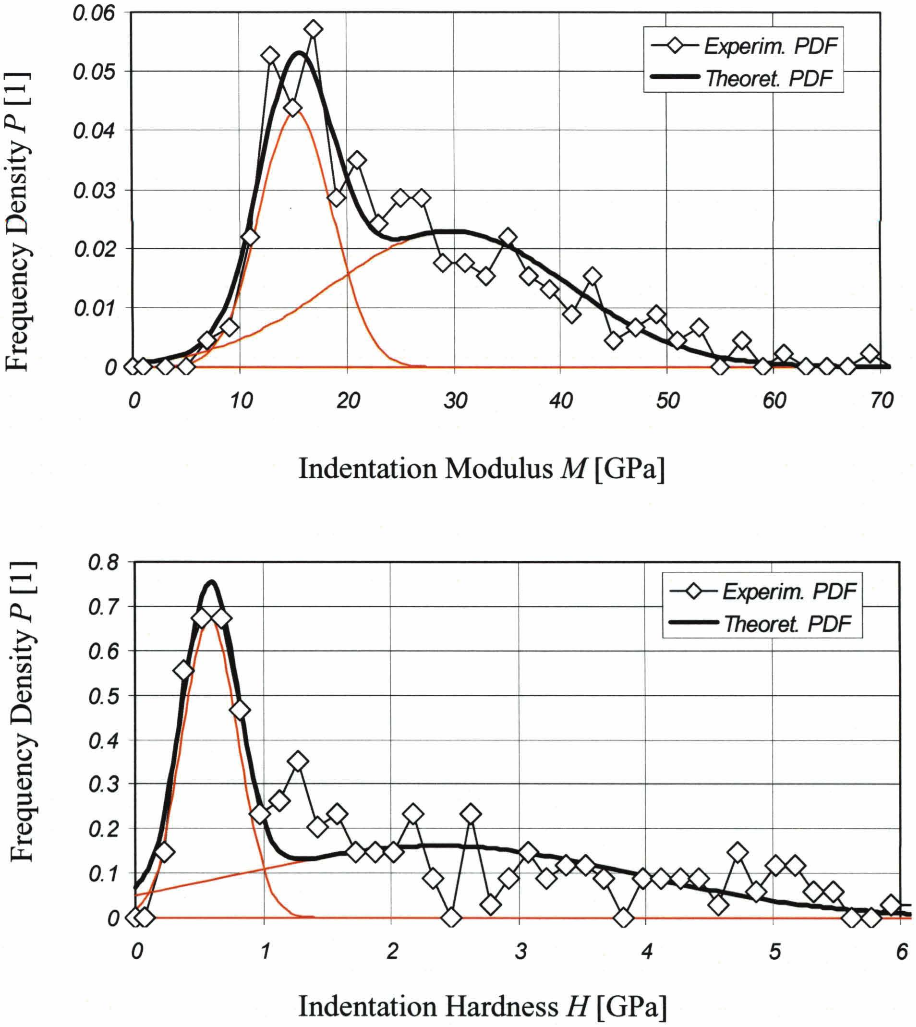

Figure 2-6: Frequency distributions for indentation modulus M and indentation hardness H of a shale material, together with best fitted normal distributions for phase properties. (Shale #3, indentation normal to bedding $x3$; courtesy of Chris Bobko, MIT).

and m^s is the solid's (isotropic) plane stress modulus (see Eq. (2.13)):

$$m^s = 4\mu^s \frac{3r^s + 1}{3r^s + 4} \tag{2.28}$$

- An isotropic Polycrystal (or self-consistent) morphology of solid particles that loose continuity below a solid percolation threshold of $\eta_0 = 1/2$ [24]:

$$\frac{M}{m^s} = \frac{\mu^{\text{hom}}}{\mu^s} \frac{\left(9\eta r^s + 4\mu^{\text{hom}}/\mu^s + 3r^s\right)(3r^s + 4)}{4\left(4\mu^{\text{hom}}/\mu^s + 3r^s\right)(3r^s + 1)} \tag{2.29}$$

where μ^{hom}/μ^s is the macro-to-micro shear modulus ratio:

$$\begin{aligned} \frac{\mu^{\text{hom}}}{\mu^s} &= \frac{1}{2} - \frac{5}{4}(1-\eta) - \frac{3}{16} r^s (2+\eta) \\ &+ \frac{1}{16}\sqrt{144(1-r^s) - 480\eta + 400\eta^2 + 408 r^s \eta - 120 r^s \eta^2 + 9(r^s)^2 (2+\eta)^2} \end{aligned} \tag{2.30}$$

The focus of a multi-scale indentation analysis of porous materials is two-fold: (1) investigation of the microstructure of a heterogeneous material, by analyzing the scaling relations of the experimental indentation properties (M), with the porosity φ or the solid's packing density $\eta = 1 - \varphi$; and (2) determination of the solid's intrinsic material properties (m^s, r^s) by means of (2.27) and (2.29). Figure 2-7 illustrates this approach in form of a plot of the indentation modulus ratio M/m^s vs. packing density.

In summary, the dimensionless expressions (2.27) and (2.29) provide a means to determine from measurements of the indentation modulus M (within the context of continuum indentation analysis, i.e. Eq. (2.2)) the solid stiffness and the solid morphology. Such scaling relations are currently not available for hardness measurements of porous materials, linking the hardness to the strength properties of the solid phase of the porous material, the porosity and the pore morphology.

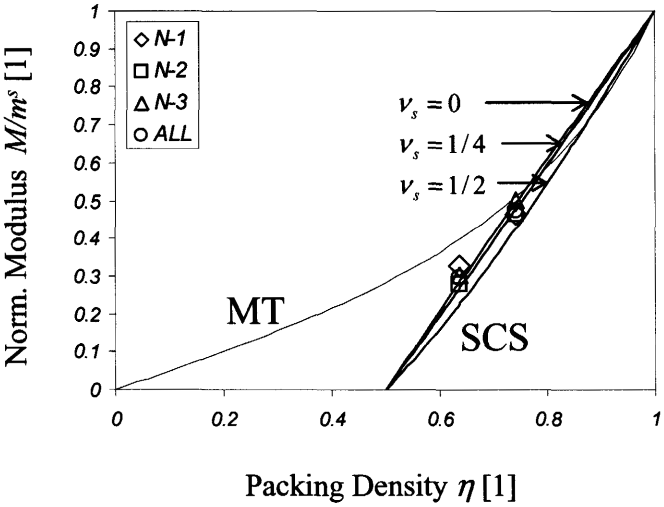

Figure 2-7: Multi-scale indentation analysis: the effective-to-solid stiffness ratio vs. solid packing density: 'MT' stands for 'Mori-Tanaka scheme', which captures a matrix-pore morphology, and which has been used to derive Eq. (2.27). 'SCS' stands for 'Self-Consistent Scheme', which captures a polycrystal morphology, and which has been used to derive Eq. (2.29). (From [24]; data is from Calcium-Silica Hydrates of cement-based materials).

2.4 Conclusion: Problem Formulation

An indentation test is a surface test which provides access to bulk properties of the indented material. This requires the tools of continuum indentation analysis to translate indentation data into meaningful mechanical properties. The application of indentation analysis to porous materials faces several challenges. Porous materials are by nature heterogeneous, as they are composed of a solid phase and a pore space. This heterogeneity may itself influence the indentation response, and may eventually lead to a break of the self-similarity of the indentation test, if the pore size is of a similar order as the indentation depth. In return, if the pore size is much smaller than the indentation depth, which is the case in most geomaterials dominated by nanoporosity, then an indentation test provides access to the homogenized composite properties of a porous material. This is the case we consider in this thesis. The task of indentation analysis then is to link those composite indentation properties (H, M) to properties and microstructure of the constituents. This is the goal of the multi-scale indentation analysis (see Section 2.3.3). While elastic multi-scale indentation analysis are well advanced, a multi-scale indentation strength approach has yet to be developed. This is the focus of this thesis.

To summarize the problem, let us return to the dimensional analysis of Section 2.2.2. The two dependent quantities of interest are still the indentation force P and the projected contact area A_c (respectively the contact depth h_c). However, in the case of indentation into a microhomogeneous porous material composed of a solid phase and the pore space, the two variables now depend on the following set of independent variables (see Fig. 2-8):

1. Constituent parameters: In the case of a microhomogeneous two-phase solid-pore composite, this includes the elastic stiffness properties of the solid phase, C^s_{ijkl}, and the strength properties of the solid phase, which we capture by the solid's cohesion c^s and the solid's friction angle ϕ^s, or friction coefficient α.

2. Volume fractions of the constituents: In the case of a two-phase solid-pore composite this is the porosity φ , respectively the solid concentration $\eta = 1 - \varphi$.

3. Pore morphology. As in the elastic multi-scale indentation model reviewed in Section 2.3.3, we will consider an isotropic pore morphology (spherical pores) and two pore mor-

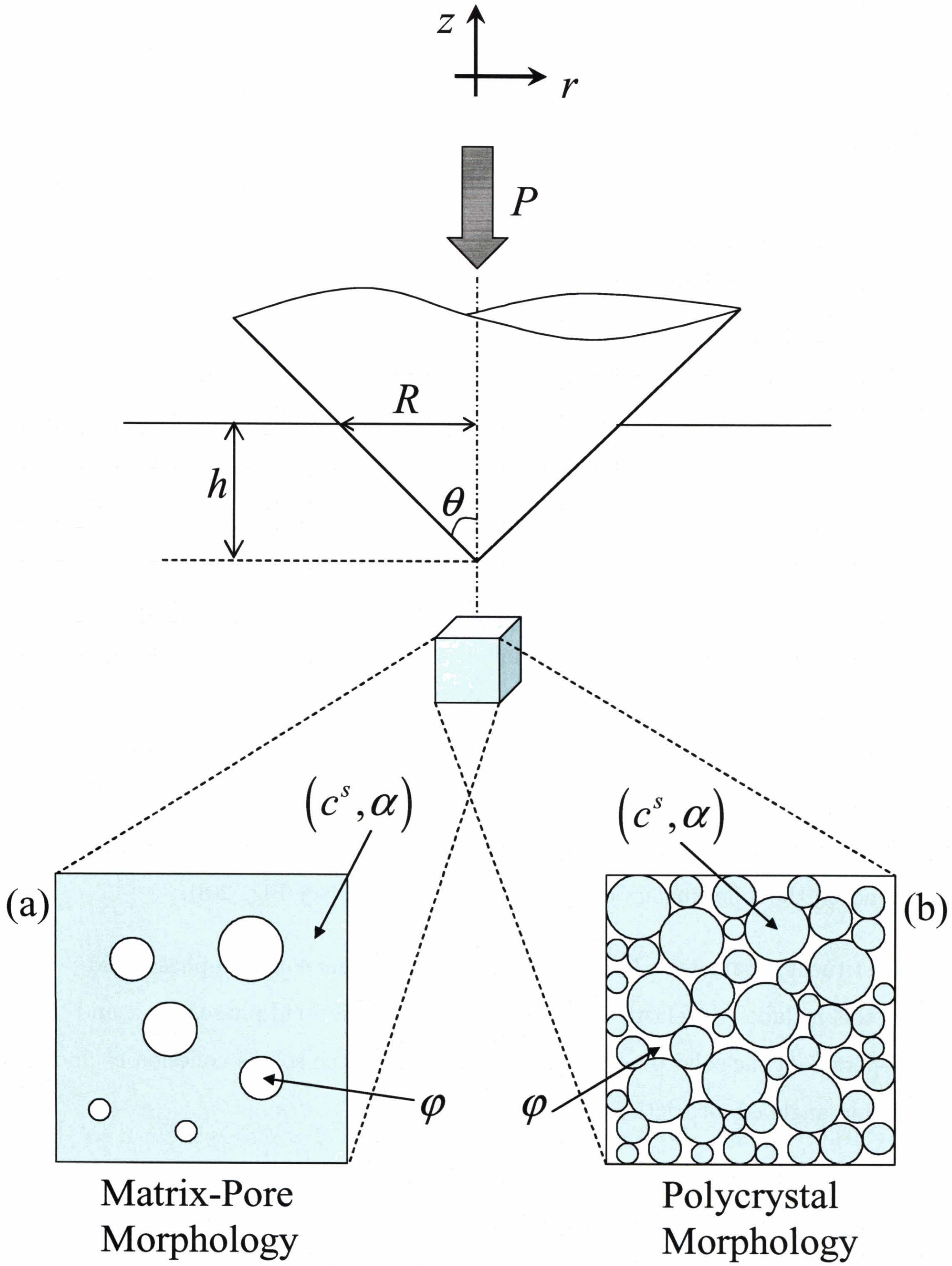

Figure 2-8: Indentation variables for indentation into a cohesive-frictional porous material.

phologies: a matrix-pore morphology and a polycrystal (or self-consistent) morphology. As shown in Figure 2-8, these two pore morphologies represent two limit cases. The case of a matrix-pore morphology captures the continuity of the matrix, while the polycrystal morphology is characterized by a solid percolation threshold below which the solid particles loose the continuity. This adds another variable to our set of independent quantities: the solid percolation threshold, η_0.

4. Indenter geometry, which in the case of conical indentation (see Section 2.1.2) reduces to the semi-apex angle θ.

5. Indentation depth h

Thus formally, instead of (2.16):

$$P = f\left(C_{ijkl}^{s}, c^{s}, \alpha, \varphi, \eta_0, \theta, h\right) \tag{2.31a}$$

$$A_c = g\left(C_{ijkl}^{s}, c^{s}, \alpha, \varphi, \eta_0, \theta, h\right) \tag{2.31b}$$

From the point of view of dimensional analysis, the difference between (2.16) and (2.31) are only two dimensionless parameters, φ, η_0, which need to be added to the dimensionless expressions (2.17):

$$\frac{P}{c^s h^2} = \Pi_\alpha\left(\frac{C_{ijkl}^{s}}{c^s}, \alpha, \varphi, \eta_0, \theta\right) \tag{2.32a}$$

$$\frac{A_c}{h^2} = \Pi_\beta\left(\frac{C_{ijkl}^{s}}{c^s}, \alpha, \varphi, \eta_0, \theta\right) \tag{2.32b}$$

and (2.18):

$$\frac{H}{c^s} = \frac{\Pi_\alpha}{\Pi_\beta} = \mathcal{H}\left(\frac{C_{ijkl}^{s}}{c^s}, \alpha, \varphi, \eta_0, \theta\right) \tag{2.33}$$

In return, there is a fundamental difference between (2.16)–(2.18) and (2.31)–(2.33). Similar to the elastic case (2.27) and (2.29), the material properties in the multi-scale hardness-strength analysis (2.33) are the one of the solid, not the composite.

The aim of the next Part of this thesis is the development of a method that allows the determination of the normalized hardness-to-solid cohesion ratio H/c^s. To achieve this goal we will employ the tools of yield design, assuming that $\left(C^s_{ijkl}/c^s\right)^{-1} \rightarrow 0$. In particular, by means of an original computational implementation of the upper bound limit theorem of yield design, we will develop such solutions for cohesive and cohesive frictional *solids*, of the form:

$$\boxed{\frac{H}{c^s} = \mathcal{F}\left(\alpha, \varphi, \eta_0, \theta\right)} \tag{2.34}$$

Part II

Multi-Scale Indentation Analysis of a Porous Cohesive-Frictional Material

Chapter 3

Multi-Scale Yield-Design Approach

In the Second Part of this thesis we develop and implement a multi-scale yield design approach for the indentation analysis of the strength properties of a porous material composed of a solid phase and a pore space. The model we develop is based on the scale separability condition: the characteristic size of the pore space is much smaller than the indentation depth. This assumption of scale separability allows us to separate the problem in two scales: at the scale of the indentation operation, we consider an *rev* that has a homogenous strength behavior. At a scale below, the *rev* is composed of a solid phase and a pore space. The strength behavior of the solid phase is assumed to follow a pure shear strength criterion, namely a Von-Mises Criterion, and a pressure-dependent strength criterion of the Drucker-Prager type. A first homogenization step thus consists in determining the strength domain of the porous media at the scale of the *rev*. Implementation of this homogenized strength criterion in a yield design approach of the indentation test then provides a means to link the hardness to the strength properties of the solid and to properties characterizing the microstructure, as outlined in Chapter 2. This Chapter develops in details this multi-scale yield design approach, and illustrates the approach through the development of an analytical lower bound. Chapter 4 then shows the computational implementation of the upper bound approach.

3.1 Yield Design Approach for Conical Indentation

Our starting point is the scale of conical indentation into an infinite half-space composed of *revs* of a characteristic length scale $\mathcal{L}$, satisfying the scale separability condition (2.22), which we recall:

$$d \ll \mathcal{L} \ll h \tag{3.1}$$

where d is the characteristic size of the microstructure, roughly the porosity. The indentation depth h which is the only relevant length scale of the indentation operation in the infinite half-space (which by its very nature has no length scale), characterizes the order of magnitude of the variation of the position vector $\underline{x}$, and therefore determines the characteristic length scale of the application of differential calculus necessary for indentation analysis.

3.1.1 Problem Formulation

Consider an indentation test of a rigid conical indenter (semi-apex angle θ) into an infinite half-space oriented in the $-z$ direction (see Fig. 3-1).

The indenter is at an indentation depth h, the projected contact area A_c is assumed to be known, and a force P is applied. The work rate provided from the outside to the (half-space materials) system is [37]:

$$\delta W = P\overset{\circ}{h} = \int_{A_M} \underline{T}\left(\underline{n}\left(\underline{x}\right)\right) \cdot \underline{U}\left(\underline{x}\right)\, da \tag{3.2}$$

where $\overset{\circ}{h}$ is the rate of indentation depth, $A_M = A_c/\sin\theta$ is the contact area of the cone mantel with the material (A_c being the projection of this surface on the $z-$axis); $\underline{T}\left(\underline{n}\right) = \mathbf{\Sigma} \cdot \underline{n}$ is the stress vector on A_M oriented by the unit outward normal $\underline{n}$ (positive outward to the material domain; i.e. in a cylinder coordinate frame $\underline{n} = -\cos\theta\, \underline{e}_r + \sin\theta\, \underline{e}_z$), $\mathbf{\Sigma}$ is the macroscopic stress tensor; and $\underline{U}$ is the velocity field of the material on A_M.

In elastoplastic problems, a part of the external work rate (3.2) is stored into recoverable elastic energy (incl. hardening) into the material system. By contrast, limit analysis is based on the assumption, that a materials system, at plastic collapse, has exhausted, in response to the prescribed force P, its capacities, (i) to develop stress fields that are both statically compatible

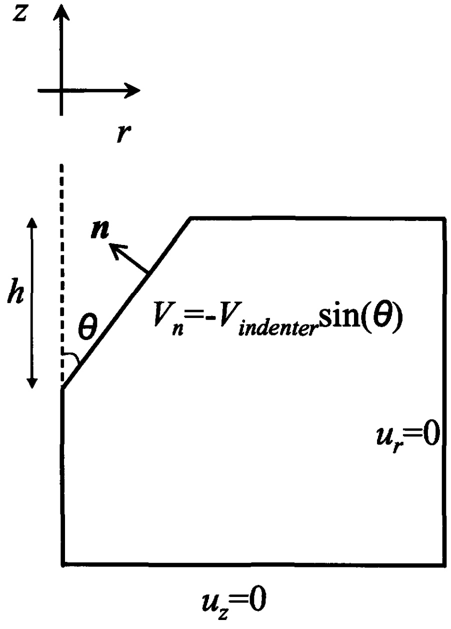

Figure 3-1: Yield Design Approach for conical indentation.

(i.e. in equilibrium) with the external loading and compatible with the local strength domain of the constitutive materials; and (ii) to store the externally supplied work rate (3.2) into recoverable elastic energy. As a consequence, the work rate δW is entirely dissipated in the material bulk (and eventually along surfaces of discontinuity, which will not be pursued in this study); hence from an application of the divergence theorem to (3.2) (see, for instance, [63],[77]):

$$P\overset{\circ}{h} = \int_{\Omega} \mathbf{\Sigma} : \mathbf{D}\, d\Omega \tag{3.3}$$

where $\mathbf{\Sigma} : \mathbf{D}$ represents the maximum dissipation capacity the homogenized material can develop in the material bulk for the solution fields ($\mathbf{\Sigma}$,$\underline{U}$). The solution stress field $\mathbf{\Sigma}$ is statically and plastically admissible, satisfying:

$$\mathbf{\Sigma} = {}^t\mathbf{\Sigma};\ \operatorname{div}\mathbf{\Sigma} = 0;\ [\underline{T}] = [\mathbf{\Sigma}\cdot\underline{n}] = 0 \tag{3.4a}$$

$$F(\mathbf{\Sigma}) \leq 0 \tag{3.4b}$$

where superscript t stands for transpose; and $F(\boldsymbol{\Sigma})$ is the yield function defining the strength domain of the material system in continuous material sub-domains; while $\mathbf{D}$ is the solution strain rate field in continuous material sub-domains, which is kinematically compatible with the velocity field $\underline{U}$ and compatible with the plastic flow rule of the material:

$$\mathbf{D} = \frac{1}{2}\left(\operatorname{grad}\underline{U} + {}^{t}\operatorname{grad}\underline{U}\right) = \mathring{\lambda}\frac{\partial F(\boldsymbol{\Sigma})}{\partial \boldsymbol{\Sigma}} \tag{3.5}$$

Provided that $(\boldsymbol{\Sigma},\underline{U})$ is related through (3.5) by the normality rule of plastic flow, it is readily understood that the maximum dissipation capacity $\boldsymbol{\Sigma} : \mathbf{D}$ can be expressed as a unique function of the strain rate. This function is called dissipation function [77] or support functions [63]:

$$\Pi(\mathbf{D}) = \sup\left(\boldsymbol{\Sigma} : \mathbf{D};\ F(\boldsymbol{\Sigma}) \leq 0\right) \tag{3.6}$$

Some background on the properties of the Π function is given in Appendix A.2. What we retain here is that the yield design approach requires the determination of the yield function $F(\boldsymbol{\Sigma})$ and the associated dissipation function $\Pi(\mathbf{D})$. As we will see below, this requires us to choose an appropriate strength criterion for a cohesive-frictional *porous* material.

3.1.2 Lower and Upper Bound Theorem

The limit theorems of yield design approach the actual dissipation capacity (3.3) by a lower and an upper bound estimate. The lower estimate is based on statically and plastically admissible stress fields $\boldsymbol{\Sigma}'$ satisfying (3.4). Such a lower bound approach leads to underestimating the actual dissipation capacity:

$$\int_{\Omega} \boldsymbol{\Sigma}' : \mathbf{D}\, d\Omega = P'\mathring{h} \leq P\mathring{h} \tag{3.7}$$

The upper bound approach is based on kinematically and plastically admissible strain rate fields $\mathbf{D}'$, satisfying (3.5). Such an upper bound approach leads to overestimating the actual dissipation capacity:

$$P\mathring{h} \leq \int_{\Omega} \boldsymbol{\Sigma} : \mathbf{D}'\, d\Omega \leq \int_{\Omega} \Pi(\mathbf{D}')\, d\Omega \tag{3.8}$$

For the actual limit load solution ($\mathbf{\Sigma}$,$\underline{U}$), both the lower and upper bound give the same result: the problems are 'dual'[1] to each other. In return, the lower and the upper bound define two formidable optimization problems:

- Lower Bound Theorem (or static principle of limit analysis): Among all statically admissible (SA) stress fields $\mathbf{\Sigma}'$, find the one which maximizes the indentation load P. Letting $\overset{\circ}{h} = 1$, the lower bound (3.7) of an indentation test can be expressed in terms of a lower bound of the hardness $H^- = P'/A_c$:

$$H^- \leq H = \frac{1}{A_c} \sup_{\substack{\mathbf{\Sigma}' SA \\ F(\mathbf{\Sigma}')\leq 0}} \int_\Omega \mathbf{\Sigma}' : \mathbf{D}\, d\Omega;\ \overset{\circ}{h} = 1 \tag{3.9}$$

- Upper Bound Theorem (or kinematic principle of limit analysis): Among all kinematically admissible (KA) velocity fields $\underline{U}'$, find the one which minimizes the maximum dissipation capacity the system can afford. This can be expressed in terms of an upper bound H^+ of the hardness:

$$H = \frac{1}{A_c} \inf_{\underline{U}' KA} \int_\Omega \Pi\left(\mathbf{D}'\right) d\Omega \leq H^+;\ \overset{\circ}{h} = 1 \tag{3.10}$$

3.1.3 Frictionless Contact Condition

To complete the problem formulation for either lower or upper bound, we need to define boundary conditions, or more precisely contact conditions at the indenter-material interface (see Fig. 3-1). For a frictionless contact condition, all shear stresses at the interface are zero, i.e. $\forall \underline{t} \cdot \underline{n} = 0;\ \underline{t} \cdot \underline{T}'(\underline{n}) = 0 \Leftrightarrow \underline{T}'(\underline{n}) = \Sigma' \underline{n}$:

$$\forall (r,z) \in A_M;\ \left\{ \begin{array}{c} \underline{t} \cdot \underline{T}'(\underline{n}) = \frac{1}{2}\left(\Sigma'_{zz} - \Sigma'_{rr}\right)\sin 2\theta + \Sigma'_{rz}\cos 2\theta = 0 \\ \\ \underline{n} \cdot \underline{T}'(\underline{n}) = \Sigma'_{rr}\sin^2\theta + \Sigma'_{zz}\cos^2\theta - \Sigma'_{rz}\sin 2\theta \end{array} \right\} \tag{3.11}$$

$$\forall r \geq a; z = 0 : \underline{T}'(\underline{n}) = 0$$

---

[1] More details about the duality of the limit theorems are given in Appendix A.1.

In the upper bound approach, a velocity field is kinematically admissible, if it satisfies the zero-velocity boundary conditions at infinity. On the other hand, there is an additional interface condition, which arises from a frictionless contact condition, which a priori permits a tangential slip (without dissipation), while the normal velocity $\underline{U}' \cdot \underline{n}$ is the one of the rigid indenter [37]:

$$\begin{aligned} &\forall\,(r,z) \in A_M;\ \underline{U}' \cdot \underline{n} = -\overset{\circ}{h} \sin\theta \\ &(r,z) \to \infty;\ \underline{U}' = 0 \end{aligned} \tag{3.12}$$

3.2 Homogenized Strength Criteria of Porous Cohesive-Frictional Materials

In this section we review some elements of strength homogenization theory of porous materials based on the contributions of Dormieux and co-workers [30]. Thanks to the scale separability condition (3.1) we can separate the scale of the *rev* from the one of its constituents, i.e. the solid phase and the pore space. The 'effective' behavior of the composite defined at the scale of the *rev*, intervenes in the indentation analysis. In the chosen Yield Design Approach (see Section 3.1), this 'effective' strength behavior is captured by the yield criterion (3.4b) and by the corresponding dissipation functions (3.6), which represent dual definitions of the (macroscopic) strength behavior (see Appendix A.1). The focus of this section is the determination of both for a porous material composed at a microscale of a solid phase and an empty pore space. What we aim to derive is the macroscopic expression of the strength criterion, based on the strength properties of the solid phase, and on information relating to the pore morphology. This will be achieved within the framework of nonlinear homogenization theory of strength properties, which was pioneered by Suquet [69][70], and further developed and implemented for porous materials by Dormieux and co-workers [30].

We consider an *rev* positioned at the macroscale at point $\underline{x}$ (Fig. 3-2). The *rev* is composed, at the microscale, of a solid phase and a pore space. We denote by $\underline{z}$ the position vector that locates each point within the microstructure, so that the overall position is defined by $\underline{x} + \underline{z}$. Depending on $\underline{z}$, the microscopic particle located at point $\underline{z}$ belongs either to the solid phase (V^s) or to the pore space (V^p). As a consequence the microscopic stress-field is heterogeneous

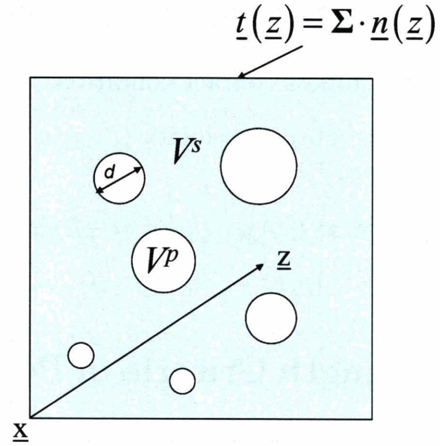

Figure 3-2: *rev* composed of a solid phase and a pore space, sujected to a uniform stress at its boundary.

within the *rev*:

$$\boldsymbol{\sigma}(\underline{z}) = \begin{cases} \neq 0 & \underline{z} \in V^s \\ = 0 & \underline{z} \in V^p \end{cases} \tag{3.13}$$

Note that we employ here a 'small' $\boldsymbol{\sigma}$ instead of a 'capital' $\mathbf{\Sigma}$, in order to indicate that the stress-field is defined at the microscale. On the other hand, the micro- and the macro stress are related by the stress averaging relation:

$$\mathbf{\Sigma} = \overline{\boldsymbol{\sigma}(\underline{z})} = (1-\varphi)\,\overline{\boldsymbol{\sigma}(\underline{z})}^s \tag{3.14}$$

where an 'overbar' stands for volume averaging; $\varphi = 1 - \eta$ is the porosity (η is the solid concentration); and the superscript s adjacent to the 'overbar' in (3.14) stands for the volume average over the solid phase:

$$\overline{\boldsymbol{\sigma}(\underline{z})}^s = \frac{1}{V^s}\int_{V^s} \boldsymbol{\sigma}(\underline{z})\, dV_z \tag{3.15}$$

3.2.1 Strength Domain of the Solid Phase

In what follows, we will consider only the micro- and macro- isotropic strength situation. This implies two conditions:

1. The strength behavior of the solid phase is defined by an isotropic strength criterion, that is, it depends only on the micro-stress invariants:

$$f^{s}(\boldsymbol{\sigma})=\mathcal{F}\left(I_1=\operatorname{tr}\boldsymbol{\sigma};I_2=\frac{1}{2}\operatorname{tr}(\boldsymbol{\sigma}\cdot\boldsymbol{\sigma});I_3=\frac{1}{3}\operatorname{tr}(\boldsymbol{\sigma}\cdot\boldsymbol{\sigma}\cdot\boldsymbol{\sigma})\right) \tag{3.16}$$

   where $f^{s}(\boldsymbol{\sigma})$ stands for the strength criterion of the solid phase. Among all possible isotropic strength criteria for solids, we will consider two strength criteria which depend only on the first two stress invariants, and which appear to us representative for a large range of isotropic solid strength criteria. These are:

   (a) The Von-Mises Criterion which is an isotropic shear strength criterion:

$$f^{s}(\boldsymbol{\sigma})=\sqrt{J_2}-c^{s}\leq 0 \tag{3.17}$$

   where $J_2=\frac{1}{2}s_{ij}s_{ij}$ is the 2nd invariant of the stress deviator $s_{ij}=\sigma_{ij}-\frac{1}{3}I_1\delta_{ij}$ (δ_{ij} is the Kronecker delta), and where c^{s} is the solid's cohesion. As an alternative to the 'direct' definition of the solid's strength domain in form of a strength criterion, we will employ here below the dual definition, expressed by the dissipation function. For a Von-Mises solid, the dissipation function reads [63]:

$$\pi^{s}(\mathbf{d})=\begin{cases}2c^{s}\sqrt{J_2'} & \text{if } I_1'=0\\ \infty & \text{if } I_1'\neq 0\end{cases} \tag{3.18}$$

   where $I_1'=\operatorname{div}_z\underline{v}=\operatorname{tr}\mathbf{d}$ is the volume strain rate, and $J_2'=\frac{1}{2}\boldsymbol{\delta}:\boldsymbol{\delta}$ is the deviatoric strain rate invariant of the strain rate tensor $\mathbf{d}(\underline{z})=\frac{1}{3}I_1'\mathbf{1}+\boldsymbol{\delta}$. Similarly to the micro-stress field, we here employ a 'small' π and a 'small' $\mathbf{d}$ to indicate the microscopic origin of the dissipation function and of the strain rate. The latter is the symmetric part of the gradient of the micro-velocity field $\underline{v}=\underline{v}(\underline{z})$:

$$\mathbf{d}(\underline{z})=\frac{1}{2}\left(\operatorname{grad}\underline{v}+{}^{t}\operatorname{grad}\underline{v}\right)=\overset{\circ}{\lambda}\frac{\mathbf{s}}{2\sqrt{J_2}} \tag{3.19}$$

   (b) The Drucker-Prager Criterion which is an isotropic pressure-dependent strength criterion:

$$f^s(\boldsymbol{\sigma}) = \sqrt{J_2} + \alpha\left(\frac{1}{3}I_1 - h^s\right) \leq 0 \tag{3.20}$$

where α is the solid's friction coefficient and $h^s = c^s/\alpha$ is the cohesion pressure (or isotropic tensile strength). The corresponding dissipation function reads [77]:

$$\pi^s(\mathbf{d}) = \begin{cases} h^s I_1' & \text{if } I_1' \geq 2\alpha\sqrt{J_2'} \\ \infty & \text{else} \end{cases} \tag{3.21}$$

where the microscopic strain rate $\mathbf{d}$ is given by the flow rule:

$$\mathbf{d}\left(\underline{z}\right) = \frac{1}{2}\left(\operatorname{grad}\underline{v} + {}^t\operatorname{grad}\underline{v}\right) = \overset{\circ}{\lambda}\left(\frac{\mathbf{s}}{2\sqrt{J_2}} + \frac{\alpha}{3}\mathbf{1}\right) \tag{3.22}$$

An associated flow rule yields $I_1' = 2\alpha\sqrt{J_2'} \geq 0$, exhibiting thus a plastically dilating behavior.

2. The pore morphology or the solid particle morphology is isotropic, having no directional bias that introduces strength anisotropy. A representative isotropic morphology is the sphere (representative of spherical pores and/or spherical solid particles).

3.2.2 Elements of Strength Homogenization Theory

In order to link the microscopic strength behavior to macroscopic strength behavior, consider the *rev* to be subjected to a uniform stress boundary condition:

$$\text{on } \partial V : \underline{t}\left(\underline{z}\right) = \boldsymbol{\Sigma} \cdot \underline{n}\left(\underline{z}\right) \tag{3.23}$$

where $\boldsymbol{\Sigma}$ is the macroscopic stress related to the microscopic stress field $\boldsymbol{\sigma}\left(\underline{z}\right)$ by (3.14). The external work rate induced by this loading is:

$$\delta W = \int_{\partial V} \underline{t}\left(\underline{z}\right) \cdot \underline{v}\left(\underline{z}\right)\, da = V\,\boldsymbol{\Sigma} : \mathbf{D} \tag{3.24}$$

where $\mathbf{D}$ is the macroscopic strain rate tensor which is the volume average of the microscopic strain rates $\mathbf{d}(\underline{z})$:

$$\mathbf{D} = \frac{1}{2V}\int_{\partial V} \left(\underline{v}(\underline{z}) \otimes \underline{n}(\underline{z}) + \underline{n}(\underline{z}) \otimes \underline{v}(\underline{z})\right) da_z = \overline{\mathbf{d}(\underline{z})} \tag{3.25}$$

Using the Hill Lemma (which applies provided uniform boundary condition), we note that:

$$\mathbf{\Sigma} : \mathbf{D} \equiv \overline{\boldsymbol{\sigma}(\underline{z}) : \mathbf{d}(\underline{z})} \tag{3.26}$$

Within the context of yield design, the left hand side of (3.26) representing the external work rate (3.24), is readily identified as the macroscopic dissipation function (3.6). According to yield design theory, this external work rate is entirely dissipated in heat form as expressed by the right hand side of (3.26) which in turn is readily identified as the volume average of the microscopic dissipation function. The Hill Lemma (3.26), therefore, provides the link between the macroscopic and the microscopic dissipation function [69], and reads for an empty porous material [39], [30]:

$$\Pi(\mathbf{D}) \equiv \overline{\pi(\underline{z}, \mathbf{d}(\underline{z}))} = (1-\varphi)\, \overline{\pi^s(\mathbf{d}(\underline{z}))}^s \tag{3.27}$$

where π^s is the dissipation function of the solid, as specified by (3.18) and (3.21) for a Von-Mises and a Drucker-Prager solid; that is:

1. For a Von-Mises solid, ensuring the incompressibility of the micro-velocity field (see Eq. (3.18)):

$$\Pi(\mathbf{D}) = 2(1-\varphi)\, c^s \overline{\sqrt{J_2'}}^s \tag{3.28}$$

2. For a Drucker-Prager solid, provided that $I_1' \geq 2\alpha^s \sqrt{J_2'}$ (see Eq. (3.21)):

$$\Pi(\mathbf{D}) = (1-\varphi)\, \frac{c^s}{\alpha} \overline{I_1'}^s \tag{3.29}$$

In summary, the key to the homogenization of the solid's strength properties is an appropriate representation of the microscopic strain rate fields $\mathbf{d}(\underline{z})$ that develop within the solid phase at plastic collapse, and which are related to the macroscopic strain rate $\mathbf{D}$ by (3.25).

Those strain fields are used as input for calculating the solid's dissipation function (3.18) and (3.21); and finally volume averaging yields the macroscopic dissipation function. The procedure appears straightforward; however, its simplicity belies its complexity due to the highly heterogeneous strain rate fields that develop around the elementary heterogeneities in a porous material at plastic collapse: the pores. The approach developed by Dormieux and coworkers [30] for cohesive-frictional porous materials circumvents this difficulty by introducing an effective strain rate.

3.2.3 Average and Effective Strain (Rates) in the Solid

As we have seen, all comes down, in the strength homogenization theory, to evaluating the average dissipation rate (3.27) associated with plastic collapse of the solid phase in functions of the macroscopic strain rate $\mathbf{D}$. The question therefore is how to relate $\mathbf{d}(\underline{z})$ to $\mathbf{D}$, or, in the case of an isotropic solid strength behavior (3.28) and (3.29), $I_1'(\underline{z}) = \operatorname{tr}\mathbf{d}(\underline{z})$ and $J_2'(\underline{z}) = \frac{1}{2}\boldsymbol{\delta}(\underline{z}) : \boldsymbol{\delta}(\underline{z})$ to $\operatorname{tr}\mathbf{D}$ and $\frac{1}{2}\boldsymbol{\Delta} : \boldsymbol{\Delta}$.

To this end, an interesting parallel can be made with the micro-macro strain relations in linear micromechanics. For a micro- and macro linear isotropic porous material, the first-order volume averages over the solid phase of the volume strain $\operatorname{tr}\boldsymbol{\varepsilon}(\underline{z})$ and deviator strain $\mathbf{e}(\underline{z}) = \boldsymbol{\varepsilon}(\underline{z}) - \frac{1}{3}(\operatorname{tr}\boldsymbol{\varepsilon}(\underline{z}))\,\mathbf{1}$ are given by [29]:

$$(1-\varphi)\,\overline{\operatorname{tr}\boldsymbol{\varepsilon}(\underline{z})}^{s} = \frac{k^{\mathrm{hom}}}{k^{s}}\operatorname{tr}\mathbf{E} \tag{3.30a}$$

$$(1-\varphi)\,\overline{\mathbf{e}(\underline{z})}^{s} : \overline{\mathbf{e}(\underline{z})}^{s} = \frac{\mu^{\mathrm{hom}}}{\mu^{s}}\mathbf{E}_d : \mathbf{E}_d \tag{3.30b}$$

with $\mathbf{E}_d = \mathbf{E} - \frac{1}{3}(\operatorname{tr}\mathbf{E})\,\mathbf{1}$ the macroscopic strain deviator tensor. k^{hom} and μ^{hom} are the macroscopic bulk and shear moduli, and k^{s} and μ^{s} are the bulk and shear moduli of the solid phase. The linear averages display a de-coupling between the volume and deviator strain: a macroscopic volume strain $\operatorname{tr}\mathbf{E}$ provokes on-average only a microscopic volume strain in the solid phase $\overline{\operatorname{tr}\boldsymbol{\varepsilon}(\underline{z})}^{s}$, and a macroscopic strain deviator $\mathbf{E}_d$ provokes on-average only a microscopic strain average. A link of this form is readily recognized to be limited when it comes to evaluating strain (resp. strain rates) level in the plastic limit state. It suffices to consider a hollow sphere subjected to an isotropic loading at its outer surface. In the solid adjacent to the solid, micro-shear strains govern the behavior, which are expected to influence the overall strength behavior.

Higher order averages capture those coupled volume-shear strain conditions. The quadratic averages of the volume and deviator strain of the solid are given by [29]:

$$\begin{aligned} \frac{1}{2}(1-\varphi)\overline{(\operatorname{tr}\boldsymbol{\varepsilon}(\underline{z}))^2}^s &= \frac{1}{2}\frac{\partial k^{\text{hom}}}{\partial k^s}(\operatorname{tr}\mathbf{E})^2 + \frac{\partial \mu^{\text{hom}}}{\partial k^s}\mathbf{E}_d : \mathbf{E}_d & (3.31\text{a}) \\ (1-\varphi)\overline{\mathbf{e}(\underline{z}) : \mathbf{e}(\underline{z})}^s &= \frac{1}{2}\frac{\partial k^{\text{hom}}}{\partial \mu^s}(\operatorname{tr}\mathbf{E})^2 + \frac{\partial \mu^{\text{hom}}}{\partial \mu^s}\mathbf{E}_d : \mathbf{E}_d & (3.31\text{b}) \end{aligned}$$

Higher order averages can be seen as 'effective' strains in the sense that they appear to be a better approximation to capture the heterogeneity of the strain field in the microstructure. In order to use expressions (3.31) for strength homogenization in the sense of (3.27), (3.28) and (3.29), it is necessary to make the link $(\boldsymbol{\varepsilon}, \mathbf{E}) \rightarrow (\mathbf{d}, \mathbf{D})$ and give a 'plastic' meaning to the stiffness properties.

3.2.4 Von-Mises Solid

Consider a Von-Mises solid, which deforms plastically in an incompressible way (i.e. (3.19)). Incorporating this plastic incompressibility condition into (3.31) requires:

$$\frac{\partial k^{\text{hom}}}{\partial k^s} = 0; \ \frac{\partial \mu^{\text{hom}}}{\partial k^s} = 0 \tag{3.32}$$

Hence, k^{hom} and μ^{hom} can be seen as the homogenized bulk and shear moduli of a porous material composed of an incompressible solid, $k^s \rightarrow \infty$. Under this condition, it is readily understood from a dimensionless analysis that k^{hom} and μ^{hom} are linear functions of the solid's shear modulus; hence:

$$\frac{\partial k^{\text{hom}}}{\partial \mu^s} = \frac{k^{\text{hom}}}{\mu^s} = \mathcal{K}(\varphi; \eta_0); \ \frac{\partial \mu^{\text{hom}}}{\partial \mu^s} = \frac{\mu^{\text{hom}}}{\mu^s} = \mathcal{M}(\varphi; \eta_0) \tag{3.33}$$

Functions $\mathcal{K}(\varphi; \eta_0)$ and $\mathcal{M}(\varphi; \eta_0)$ which will be given later on depend only on the porosity φ and the pore morphology captured here through a solid percolation threshold η_0. Then, transposing (3.31) to estimate the 'effective' strain rate in the solid phase at plastic collapse, we let:

$$\begin{aligned}\frac{1}{2}(1-\varphi)\overline{(\operatorname{tr}\mathbf{d}\,(\underline{z}))^2}^s &\approx 0 &(3.34a)\\ (1-\varphi)\overline{\boldsymbol{\delta}\,(\underline{z}):\boldsymbol{\delta}\,(\underline{z})}^s &= \frac{1}{2}\mathcal{K}\,(\operatorname{tr}\mathbf{D})^2+\mathcal{M}\,\boldsymbol{\Delta}:\boldsymbol{\Delta} &(3.34b)\end{aligned}$$

The effective deviatoric strain rate (3.34a) now provides an estimate of $\overline{\sqrt{J_2'}}^s$ in (3.28), and thus an estimate of the macroscopic dissipation function of a porous material composed of a Von-Mises solid:

$$\begin{gathered}\overline{\sqrt{J_2'}}^s \equiv \sqrt{\frac{1}{2}\overline{\boldsymbol{\delta}\,(\underline{z}):\boldsymbol{\delta}\,(\underline{z})}^s}\\ \Downarrow\\ \boxed{\Pi^{est}\,(\mathbf{D})=c^s\sqrt{(1-\varphi)\,(\mathcal{K}\,(\operatorname{tr}\mathbf{D})^2+2\mathcal{M}\,\boldsymbol{\Delta}:\boldsymbol{\Delta})}\geq 0}\end{gathered} \qquad (3.35)$$

Finally, we seek for the expression of the yield criterion that corresponds to the dissipation function (3.35). We remind ourselves that the macro-stress $\boldsymbol{\Sigma}$ corresponding to the plastic dissipation rate $\Pi\,(\mathbf{D})=\boldsymbol{\Sigma}:\mathbf{D}$ is situated at the boundary of the macroscopic strength domain, and that the dependence of $\Pi^{est}\,(\mathbf{D})$ on the two strain rate invariants, $\operatorname{tr}\mathbf{D}$ and $\frac{1}{2}\boldsymbol{\Delta}:\boldsymbol{\Delta}$, implies that the homogenized strength criterion depends on the two macro-stress invariants $\Sigma_m=\frac{1}{3}\operatorname{tr}\boldsymbol{\Sigma}$ and $\Sigma_d=\sqrt{\frac{1}{2}\boldsymbol{\Sigma}_d:\boldsymbol{\Sigma}_d}$:

$$\Pi^{est}\,(\mathbf{D})=\boldsymbol{\Sigma}_d:\boldsymbol{\Delta}+\Sigma_m\operatorname{tr}\mathbf{D};\;F\,(\Sigma_m,\Sigma_d)=0 \qquad (3.36)$$

It follows:

$$\begin{aligned}\Sigma_m &= \frac{\partial\Pi^{est}}{\partial\,(\operatorname{tr}\mathbf{D})}=(1-\varphi)\,\mathcal{K}\frac{(c^s)^2}{\Pi^{est}}\,(\operatorname{tr}\mathbf{D}) &(3.37a)\\ \Sigma_d &= \sqrt{\frac{1}{2}\frac{\partial\Pi^{est}}{\partial\boldsymbol{\Delta}}:\frac{\partial\Pi^{est}}{\partial\boldsymbol{\Delta}}}=(1-\varphi)\,\mathcal{M}\frac{(c^s)^2}{\Pi^{est}}\sqrt{2\,\boldsymbol{\Delta}:\boldsymbol{\Delta}} &(3.37b)\end{aligned}$$

Finally, using (3.37) to replace in (3.35) $\left(\operatorname{tr}\mathbf{D},\frac{1}{2}\boldsymbol{\Delta}:\boldsymbol{\Delta}\right)$ by (Σ_m,Σ_d) yields the macroscopic

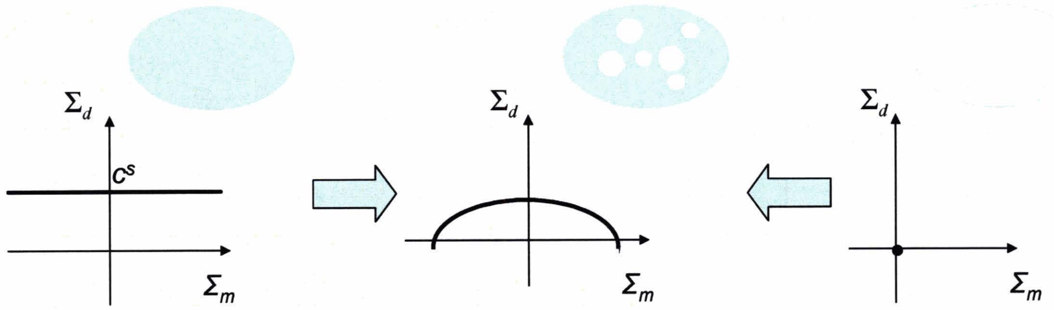

Figure 3-3: Strength homogenization of a porous material composed of a Von-Mises solid and an empty pore space.

strength criterion of a porous material whose solid phase is a Von-Mises solid:

$$\boxed{F\left(\Sigma_m, \Sigma_d\right) = \frac{1}{\mathcal{K}}\Sigma_m^2 + \frac{1}{\mathcal{M}}\Sigma_d^2 - (1-\varphi)\left(c^s\right)^2 = 0} \tag{3.38}$$

The strength domain of the porous composite is found to be a closed elliptic domain centered at the origin of the (Σ_m, Σ_d) plane (Fig. 3-3).

3.2.5 Drucker-Prager Solid

On a similar basis, one can derive the homogenized strength criterion of a porous material composed of a plastically dilating Drucker-Prager solid, $I_1' \geq 2\alpha\sqrt{J_2'}$. The derivation can be found in [30]. Here we illustrate the dual application of yield design theory and determine from the macroscopic strength criterion $F\left(\Sigma_m, \Sigma_d\right)$ the corresponding macroscopic dissipation function $\Pi^{est}\left(\mathbf{D}\right)$. The homogenized strength criterion reads [30]:

$$\boxed{F\left(\Sigma_m, \Sigma_d\right) = \left(\frac{1}{\mathcal{K}} - \frac{\alpha^2}{1-\varphi}\right)\left(\Sigma_m - \Sigma_m^c\right)^2 + \frac{1}{\mathcal{M}}\Sigma_d^2 - (1-\varphi)\left(c^s\right)^2\frac{1-\varphi}{1-\varphi-\alpha^2\mathcal{K}} = 0} \tag{3.39}$$

where $\mathcal{K} = \mathcal{K}\left(\varphi;\eta_0\right)$ and $\mathcal{M} = \mathcal{M}\left(\varphi;\eta_0\right)$ are the same functions as in the Von-Mises case (see relations (3.33). The strength domain of the porous composite is an ellipse centered at the

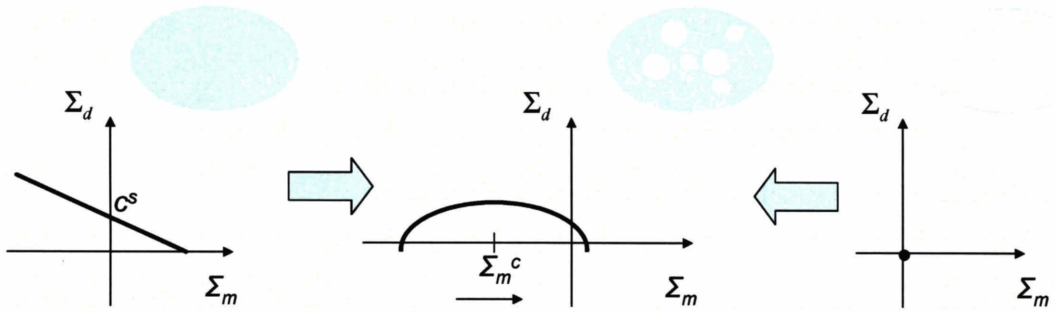

Figure 3-4: Strength homogenization of a porous material composed of a Drucker Prager solid and an empty pore space.

point $(\Sigma_m = \Sigma_m^c, \Sigma_d = 0)$ in the (Σ_m, Σ_d) plane (see Fig. 3-4):

$$\Sigma_m^c = -\frac{c^s \alpha}{1/\mathcal{K} - \alpha^2/(1-\varphi)} \tag{3.40}$$

Hence, in contrast to the symmetrical porous cohesive material (see Fig. 3-3), the cohesive frictional porous material is not symmetric w.r.t. the origin. This is due to the fact that the Drucker-Prager solid is sensitive to the confining pressure.

What we aim to derive is the macroscopic dissipation function, $\Pi(\mathbf{D}) = \Sigma_m \operatorname{tr} \mathbf{D} + \boldsymbol{\Sigma}_d : \boldsymbol{\Delta}$. To simplify the expressions, let us rewrite the elliptical strength criterion (3.39) in the form:

$$F(\Sigma_m, \Sigma_d) = \left(\frac{\Sigma_m - C}{A}\right)^2 + \left(\frac{\Sigma_d}{B}\right)^2 - 1 = 0 \tag{3.41}$$

where A, B, C are constants that are readily derived from (3.39). Next, recalling that the macroscopic strain rate $\mathbf{D}$ is parallel to the normal to the boundary of the strength domain allows us to use the normality rule:

$$\mathbf{D} = \overset{\circ}{\lambda} \frac{\partial F}{\partial \boldsymbol{\Sigma}} = \boldsymbol{\Delta} + \frac{1}{3} \operatorname{tr} \mathbf{D}; \begin{cases} \boldsymbol{\Delta} = \overset{\circ}{\lambda} \dfrac{\boldsymbol{\Sigma}_d}{B^2}; \ \sqrt{\dfrac{1}{2} \boldsymbol{\Delta} : \boldsymbol{\Delta}} = \overset{\circ}{\lambda} \dfrac{\Sigma_d}{B^2} \\ \\ \operatorname{tr} \mathbf{D} = 2 \overset{\circ}{\lambda} \dfrac{(\Sigma_m - C)}{A^2} \end{cases} \tag{3.42}$$

where $\overset{\circ}{\lambda}$ is the plastic multiplier. The plastic dissipation therefore reads:

$$\Pi^{est} = 2\overset{\circ}{\lambda}\left(\Sigma_m\frac{(\Sigma_m - C)}{A^2} + \left(\frac{\Sigma_d}{B}\right)^2\right) \tag{3.43}$$

or equivalently, after a substitution of (3.41) in (3.43):

$$\Pi^{est} = 2\overset{\circ}{\lambda}\left(1 + C\frac{(\Sigma_m - C)}{A^2}\right) \tag{3.44}$$

Moreover, to determine $\overset{\circ}{\lambda}$ as a function of the strain rate invariants $\left(\operatorname{tr}\mathbf{D}, \sqrt{\frac{1}{2}\mathbf{\Delta}:\mathbf{\Delta}}\right)$, we substitute (3.42) in the yield criterion $F(\Sigma_m, \Sigma_d) \equiv 0$ (!):

$$\begin{gathered} F(\Sigma_m, \Sigma_d) = \left(\frac{A\operatorname{tr}\mathbf{D}}{2\overset{\circ}{\lambda}}\right)^2 + \left(\frac{B\sqrt{\frac{1}{2}\mathbf{\Delta}:\mathbf{\Delta}}}{\overset{\circ}{\lambda}}\right)^2 - 1 \equiv 0 \\ \Downarrow \\ \overset{\circ}{\lambda} \equiv \frac{1}{2}\sqrt{A^2(\operatorname{tr}\mathbf{D})^2 + 2B^2\mathbf{\Delta}:\mathbf{\Delta}} \end{gathered} \tag{3.45}$$

Finally, a substitution of (3.42) and (3.45) in (3.44) yields the sought expression of the macroscopic dissipation function:

$$\boxed{\Pi^{est}(\mathbf{D}) = 2\overset{\circ}{\lambda} + C\operatorname{tr}\mathbf{D} = \sqrt{A^2(\operatorname{tr}\mathbf{D})^2 + 2B^2\mathbf{\Delta}:\mathbf{\Delta}} + C\operatorname{tr}\mathbf{D}} \tag{3.46}$$

By design, the dissipation function (3.46) is sufficiently general to be used for both the Drucker-Prager and the Von-Mises porous material. The coefficients A, B and C are given in Table 3.1. A straightforward comparison of the coefficients for the Von-Mises (superscript VM) and the Drucker-Prager solid (superscript DP) shows that the coefficients scale according to:

$$\frac{A^{DP}}{A^{VM}} = \sqrt{\frac{B^{DP}}{B^{VM}}} = \frac{1-\varphi}{1-\varphi-\alpha^2\mathcal{K}} \geq 0 \tag{3.47}$$

As expected, for $\alpha = 0$, we retrieve the Von-Mises case.

Finally, Table 3.1 also specifies the A, B, C coefficients for a modified cohesive Cam-Clay

Coefficient	Von-Mises Solid (c^s)	Drucker-Prager Solid ($h^s = c^s/\alpha, \alpha$)	Cam Clay (m, ρ, p_{cr})
A	$c^s\sqrt{(1-\varphi)\,\mathcal{K}}$	$c^s\sqrt{(1-\varphi)\,\mathcal{K}}\dfrac{1-\varphi}{1-\varphi-\alpha^2\mathcal{K}}$	p_{cr}
B	$c^s\sqrt{(1-\varphi)\,\mathcal{M}}$	$c^s\sqrt{(1-\varphi)\,\mathcal{M}}\sqrt{\dfrac{1-\varphi}{1-\varphi-\alpha^2\mathcal{K}}}$	$\dfrac{m\,p_{cr}}{\sqrt{3}}$
C	0	$\Sigma_m^c = -c^s\alpha\mathcal{K}\dfrac{1-\varphi}{1-\varphi-\alpha^2\mathcal{K}}$	$\rho - p_{cr}$

Table 3.1: Elliptical strength parameters for a porous material composed of a Von-Mises solid and a Drucker-Prager solid.

model, a common plasticity model in geotechnical engineering (developed by the (UK-) Cambridge School, namely Roscoe, Schofield, Wroth, Parry and later Burland). The yield function can be written in the form [77]:

$$2F\left(\mathbf{\Sigma}\right) = \left(\Sigma_m - \rho + p_{cr}\right)^2 + \frac{3\Sigma_d^2}{m^2} - p_{cr}^2 \leq 0 \tag{3.48}$$

where m, ρ, p_{cr} are three model parameters that are determined from triaxial testing. Rewriting (3.48) in the form of (3.41) provides a means to link those empirical fitting parameters to the strength properties of the solid phase, the porosity and its morphology (coefficients $\mathcal{K}, \mathcal{M}$):

$$\begin{aligned}
p_{cr} &= A^{DP} = c^s\sqrt{(1-\varphi)\,\mathcal{K}}\frac{1-\varphi}{1-\varphi-\alpha^2\mathcal{K}} && \text{(3.49a)}\\
m &= \sqrt{3}\frac{B^{DP}}{A^{DP}} = \sqrt{3\frac{\mathcal{M}}{\mathcal{K}}\frac{1-\varphi-\alpha^2\mathcal{K}}{1-\varphi}} && \text{(3.49b)}\\
\rho &= C + A = c^s\left(\sqrt{(1-\varphi)\,\mathcal{K}} - \alpha\mathcal{K}\right)\frac{1-\varphi}{1-\varphi-\alpha^2\mathcal{K}} && \text{(3.49c)}
\end{aligned}$$

Vice versa, the link with the Cam-Clay model shows that the homogenized strength model of a porous material composed of a cohesive-frictional solid and pore space is a 'Cam-Clay type' strength model.

3.2.6 Effect of Pore Morphology (Mori-Tanaka and Polycrystal Morphology)

We are left with specifying the effect of the pore morphology on the homogenized strength criteria (3.38) and (3.39), respectively on the macroscopic dissipation functions (3.35) and (3.46). This comes to specify the functions $\mathcal{K} = \mathcal{K}\left(\varphi;\eta_0\right)$ and $\mathcal{M} = \mathcal{M}\left(\varphi;\eta_0\right)$ defined by

(3.33). We remind ourselves that those functions are determined from the linear upscaling of the isotropic stiffness properties of a porous material composed of a linear isotropic incompressible solid phase ($k^s \rightarrow \infty$):

$$k^{\text{hom}} = \mathcal{K}(\varphi;\eta_0)\,\mu^s;\ \mu^{\text{hom}} = \mathcal{M}(\varphi;\eta_0)\,\mu^s \tag{3.50}$$

Two types of pore morphology can be distinguished, which we have already encountered in Section 2.3.3 in the context of multi-scale elastic indentation analysis.

Mori-Tanaka Scheme

The Mori-Tanaka Scheme represents a porous material with a dominating matrix-pore inclusion morphology. The matrix remains continuous for the entire solid concentration range $\eta = 1-\varphi \in [0,1]$. The linear upscaling model yields [30]:

$$\mathcal{K}_{mt}(\varphi;\eta_0=0) = \frac{4(1-\varphi)}{3\varphi} \tag{3.51a}$$

$$\mathcal{M}_{mt}(\varphi;\eta_0=0) = \frac{1-\varphi}{1+2\varphi/3} \tag{3.51b}$$

Use of (3.51a) in (3.47) shows that the elliptical criterion is defined only if the following condition is met:

$$\boxed{\frac{4}{3}\alpha^2 = \varphi_{mt}^{\lim} < \varphi \leq 1} \tag{3.52}$$

In other words, only for a Von-Mises solid phase ($\alpha = 0$) is it possible to analyze the solid-only limit case. In this case, we recognize from Table 3.1 and relations (3.51) that:

$$\lim_{\varphi=0} A_{mt}(\alpha=0) \rightarrow +\infty;\ \lim_{\varphi=0} B_{mt}(\alpha=0) = c^s;\ C_{mt}(\alpha=0) = 0 \tag{3.53}$$

Use of (3.53) in (3.41) yields:

$$\lim_{\substack{\varphi=0\\ \alpha^s=0}} F(\Sigma_m,\Sigma_d) = \left(\frac{\Sigma_d}{c^s}\right)^2 - 1 = 0 \tag{3.54}$$

which is the Von-Mises strength criterion (3.17).

It is also useful to check the strength behavior at the limit porosity $\varphi = \varphi_{mt}^{\lim} = \frac{4}{3}\alpha^2 \Leftrightarrow \alpha = \sqrt{3\varphi_{mt}^{\lim}/2}$. While $\lim_{\varphi=\varphi_{mt}^{\lim}} A_{mt} = \lim_{\varphi=\varphi_{mt}^{\lim}} B_{mt} = \lim_{\varphi=\varphi_{mt}^{\lim}} C_{mt} \rightarrow +\infty$, let us note that

$$\lim_{\varphi=\varphi_{mt}^{\lim}} \left(\frac{C_{mt}}{A_{mt}}\right) = \lim_{\varphi=\varphi_{mt}^{\lim}} \left(-\alpha\sqrt{\frac{\mathcal{K}_{mt}}{(1-\varphi)}}\right) = -1 \tag{3.55}$$

Therefore, for finite values of Σ_m and Σ_d, the homogenized strength criterion remains satisfied:

$$\lim_{\varphi=\varphi_{mt}^{\lim}} F\left(\Sigma_m, \Sigma_d\right) = \lim_{\varphi=\varphi_{mt}^{\lim}} \left(\frac{C_{mt}}{A_{mt}}\right)^2 - 1 < 0 \tag{3.56}$$

Polycrystal Morphology

Solid particles whose behavior is driven by the contact between particles are captured by the polycrystal (or self-consistent) model. The model is characterized by a percolation threshold of $\eta_0 = 1/2$, below which the solid particles loose continuity. The linear self-consistent scheme provides the following expressions for $\mathcal{K}$ and $\mathcal{M}$ [30]:

$$\mathcal{K}_{sc}\left(\varphi; \eta_0 = 1/2\right) = \frac{4\left(1-2\varphi\right)\left(1-\varphi\right)}{\varphi\left(3-\varphi\right)} \tag{3.57a}$$

$$\mathcal{M}_{sc}\left(\varphi; \eta_0 = 1/2\right) = 3\frac{\left(1-2\varphi\right)}{\left(3-\varphi\right)} \tag{3.57b}$$

We verify without difficulty that $\mathcal{K}_{sc}\left(\varphi = \eta_0 = 1/2\right) = \mathcal{M}_{sc}\left(\varphi = \eta_0 = 1/2\right) = 0$, in which case the elliptical criterion degenerates to a point at the origin of the $\left(\Sigma_m, \Sigma_d\right)$ plane, corresponding to a zero-strength capacity. Furthermore, (3.57a) and (3.47) allow us to identify the porosity domain of relevance of the self-consistent model:

$$\boxed{\frac{3}{2} + 4\alpha^2 - \frac{1}{2}\sqrt{\left(9 + 32\alpha^2 + 64\alpha^4\right)} = \varphi_{sc}^{\lim} < \varphi \leq 1/2} \tag{3.58}$$

We verify that the solid-only limit case can only be analyzed for a Von-Mises solid phase ($\alpha = 0$), for which the homogenized strength criterion degenerates to the Von-Mises strength criterion

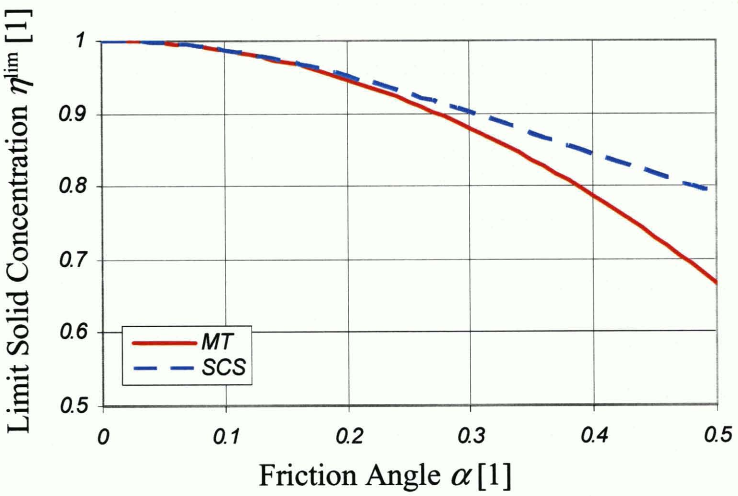

Figure 3-5: Domain of application of the homogenized strength criteria for porous media.

(3.54). On the other hand, for $\varphi = \varphi_{sc}^{\lim} \Leftrightarrow \alpha = \frac{1}{2}\sqrt{\varphi_{sc}^{\lim}\left(3-\varphi_{sc}^{\lim}\right)/\left(1-2\varphi_{sc}^{\lim}\right)}$,

$$\lim_{\varphi=\varphi_{sc}^{\lim}} \left(\frac{C_{mt}}{A_{mt}}\right) = \lim_{\varphi=\varphi_{st}^{\lim}} \left(-\alpha\sqrt{\frac{\mathcal{K}_{sc}}{(1-\varphi)}}\right) = -1 \tag{3.59}$$

Therefore, for finite values of Σ_m and Σ_d, the yield criterion is satisfied in this limit case,

$$\lim_{\varphi=\varphi_{sc}^{\lim}} F\left(\Sigma_m, \Sigma_d\right) = \lim_{\varphi=\varphi_{sc}^{\lim}} \left(\frac{C_{mt}}{A_{mt}}\right)^2 - 1 = 0 \tag{3.60}$$

We keep those limit results in mind for the forthcoming applications of our model in indentation analysis.

In summary, Figure 3-5 displays the domain of application of the homogenized strength criteria for porous media, in form of a plot of the limit solid concentration $\eta^{\lim} = 1 - \varphi^{\lim}$ as a function of the solid's friction angle, for the considered two pore morphologies, the Mori-Tanaka model and the Self-Consistent model.

3.2.7 Summary of Governing Equations

We now have two representations of the macroscopic strength criteria of porous materials:

Coefficient	Mori-Tanaka ($\eta_0 = 0$)	Self-Consistent ($\eta_0 = 1/2$)
$\mathcal{A} = A/c^s$	$2\dfrac{(1-\varphi)\sqrt{3\varphi}}{3\varphi - 4\alpha^2}$	$\dfrac{2(1-\varphi)\sqrt{\varphi(1-2\varphi)(3-\varphi)}}{3\varphi - \varphi^2 - 4\alpha^2(1-2\varphi)}$
$\mathcal{B} = B/c^s$	$\dfrac{3\sqrt{\varphi}(1-\varphi)}{\sqrt{(3+2\varphi)(3\varphi - 4\alpha^2)}}$	$\sqrt{\dfrac{3\varphi(1-2\varphi)(1-\varphi)}{(3\varphi - \varphi^2 - 4\alpha^2(1-2\varphi))}}$
$\mathcal{C} = C/c^s$	$-\dfrac{4(1-\varphi)\alpha}{3\varphi - 4\alpha^2}$	$-\dfrac{4(1-\varphi)(1-2\varphi)\alpha}{3\varphi - \varphi^2 - 4\alpha^2(1-2\varphi)}$
Limit	$\varphi_{mt}^{\lim} = \frac{4}{3}\alpha^2 < \varphi \leq 1$	$\varphi_{sc}^{\lim} = \frac{3}{2} + 4\alpha^2 - \frac{1}{2}\sqrt{(9 + 32\alpha^2 + 64\alpha^4)} < \varphi \leq 1/2$

Table 3.2: Summary of elliptical strength parameters for a porous material composed of a cohesive-frictional solid phase organized in a matrix-pore inclusion morphology (Mori-Tanaka) and a polycrystal morphology (Self-Consistent).

- The direct definition (3.41) of the yield criterion $F(\Sigma_m, \Sigma_d)$ of a porous material, which turned out to be a Cam-Clay type strength criterion:

  $$F(\Sigma_m, \Sigma_d) = \left(\frac{\Sigma_m - C}{A}\right)^2 + \left(\frac{\Sigma_d}{B}\right)^2 - 1 = 0 \tag{3.61}$$

  The coefficients (A, B, C) contain all the information about the solid's properties (c^s, α) and the isotropic microstructure (φ, η_0). Table 3.2 summarizes the coefficients for the two morphologies considered in this study, the Mori-Tanaka matrix-pore morphology and the Self-Consistent morphology (Section 3.2.6).

- The dual definition of the strength domain expressed by the macroscopic dissipation function (3.46):

  $$\Pi^{est}(\mathbf{D}) = c^s \left(\sqrt{\mathcal{A}^2 (\operatorname{tr}\mathbf{D})^2 + 2\mathcal{B}^2 \mathbf{\Delta} : \mathbf{\Delta}} + \mathcal{C}\operatorname{tr}\mathbf{D}\right) \geq 0 \tag{3.62}$$

  where $\mathcal{A}, \mathcal{B}, \mathcal{C}$ are the coefficients A, B, C normalized by the solid's cohesion c^s (see Table 3.2).

With those strength elements in hand, we can return to the initial focus of our study, which is indentation analysis. In particular, use of (3.61) and (3.62) in respectively (3.9) and (3.10) allows us to redefine our problem in the dimensionless form (2.34):

$$\boxed{\frac{H^-}{c^s} \leq \frac{H}{c^s} = \mathcal{F}\left(\alpha, \varphi, \eta_0, \theta\right) \leq \frac{H^+}{c^s}} \tag{3.63}$$

where H^-/c^s is a lower bound of the sought hardness-to-solid cohesion ratio that is obtained with any stress field $\mathbf{\Sigma}'$ that is statically admissible with the boundary conditions (3.11) and plastically admissible with the homogenized strength criterion approximated by (3.61). On the other hand, H^+/c^s is an upper bound of the sought hardness-to-solid cohesion ratio and is obtained with kinematically admissible velocity fields that satisfy the velocity boundary conditions (3.12). It follows:

$$\boxed{\frac{H}{c^s} = \mathcal{F}\left(\alpha, \varphi, \eta_0, \theta\right) = \frac{1}{A_c} \inf_{\underline{U}' KA} \int_{\Omega} \left(\sqrt{\mathcal{A}^2 \left(\operatorname{tr} \mathbf{D}\right)^2 + 2\mathcal{B}^2 \mathbf{\Delta} : \mathbf{\Delta}} + \mathcal{C} \operatorname{tr} \mathbf{D} \right) d\Omega} \tag{3.64}$$

3.3 Analytical Lower Bound: Flat Punch Indentation

By way of illustration, we develop here below an analytical lower bound solution for the flat punch problem, $\theta = \pi/2$, based on statically admissible stress fields satisfying the strength criterion (3.61).

3.3.1 Problem Formulation

The simplest statically admissible stress field is a piecewise constant stress field of the form (see Fig. 3-6):

$$z > 0, r \leq a; \; \mathbf{\Sigma}'^{(1)} = q\left[\underline{e}_r \otimes \underline{e}_r + \underline{e}_\theta \otimes \underline{e}_\theta\right] - H \underline{e}_z \otimes \underline{e}_z \tag{3.65a}$$

$$z > 0, r > a; \; \mathbf{\Sigma}'^{(2)} = q\left[\underline{e}_r \otimes \underline{e}_r + \underline{e}_\theta \otimes \underline{e}_\theta\right] \tag{3.65b}$$

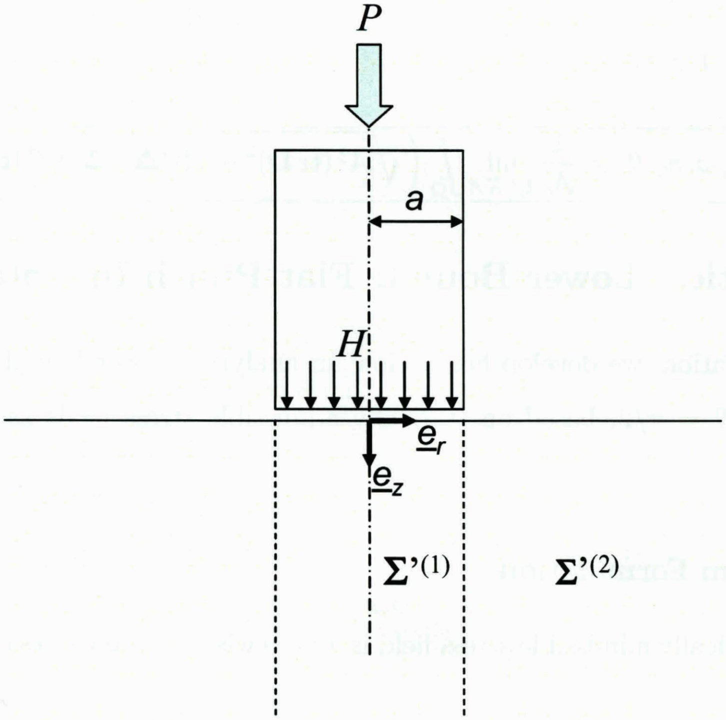

Figure 3-6: Flat punch problem with piecewise constant stress fields.

where $H = P/A_c$ is the hardness. For this stress field the stress invariants read:

$$z > 0, r \leq a;\ \Sigma'_m = \frac{1}{3}(2q - H);\ \Sigma'_d = \sqrt{\frac{1}{3}}\,|q + H| \tag{3.66a}$$

$$z > 0, r > a;\ \Sigma'_m = \frac{2}{3}q;\ \Sigma'_d = \sqrt{\frac{1}{3}}\,|q| \tag{3.66b}$$

Use in the elliptical strength criterion (3.61) yields the following two inequalities:

$$z > 0, r \leq a;\ F\left(\Sigma'_m, \Sigma'_d\right) = \left(\frac{2q - H - 3C}{3A}\right)^2 + \frac{(q + H)^2}{3B^2} - 1 \leq 0 \tag{3.67a}$$

$$z > 0, r > a;\ F\left(\Sigma'_m, \Sigma'_d\right) = \left(\frac{2q - 3C}{3A}\right)^2 + \left(\frac{q^2}{3B^2}\right) - 1 \leq 0 \tag{3.67b}$$

Assuming that both domains are at yield, we obtain three possible lower bound solutions:

$$H^- = 0 \tag{3.68a}$$

$$H^- = 6B\frac{\left(2B^2 - 3A^2\right)\sqrt{\left(3A^4 + \left(4B^2 - 3C^2\right)A^2\right)} - 9A^2CB}{9A^4 + 15B^2A^2 + 4B^4} \tag{3.68b}$$

$$H^- = 6B\frac{\left(3A^2 - 2B^2\right)\sqrt{\left(3A^4 + \left(4B^2 - 3C^2\right)A^2\right)} - 9A^2CB}{9A^4 + 15B^2A^2 + 4B^4} \tag{3.68c}$$

Since we employ a lower bound approach, we need to find the maximum value of the hardness in function of the three parameters (A, B, C), which as we will see below is:

$$\max H^- = 6B\frac{\left(3A^2 - 2B^2\right)\sqrt{\left(3A^4 + \left(4B^2 - 3C^2\right)A^2\right)} - 9A^2CB}{9A^4 + 15B^2A^2 + 4B^4} \tag{3.69}$$

3.3.2 Von-Mises Solid

We start with a Von-Mises solid, for which $C^{VM} = 0$:

$$H^- = 6B\frac{\left(3A^2 - 2B^2\right)\sqrt{\left(3A^4 + 4B^2A^2\right)}}{9A^4 + 15B^2A^2 + 4B^4} \tag{3.70}$$

Use of A^{VM} and B^{VM} (from Table 3.1), that is:

$$A^{VM} = c^s\sqrt{(1 - \varphi)\mathcal{K}};\ B^{VM} = c^s\sqrt{(1 - \varphi)\mathcal{M}};\ C^{VM} = 0 \tag{3.71}$$

yields:

$$\frac{H^-}{c^s} = \frac{6\sqrt{\mathcal{K}\mathcal{M}\,(4\mathcal{M}+3\mathcal{K})}\sqrt{(1-\varphi)}\,(3\mathcal{K}-2\mathcal{M})}{4\mathcal{M}^2+15\mathcal{K}\mathcal{M}+9\mathcal{K}^2} \tag{3.72}$$

For a matrix-pore inclusion morphology, for which $\mathcal{K} = \mathcal{K}_{mt}$ and $\mathcal{M} = \mathcal{M}_{mt}$ are given by the Mori-Tanaka estimate (3.51), we obtain:

$$\frac{H^-_{mt}}{c^s} = \mathcal{F}^-_{mt}\left(\varphi, \eta_0 = 0\right) = 12\frac{(1-\varphi)\sqrt{(5\varphi+3)}\,(6+\varphi)}{55\varphi^2+93\varphi+36} \tag{3.73}$$

In turn, a polycrystal morphology, for which $\mathcal{K} = \mathcal{K}_{sc}$ and $\mathcal{M} = \mathcal{M}_{sc}$ are given by the Self-Consistent estimate (3.57), yields:

$$\frac{H^-_{sc}}{c^s} = \mathcal{F}^-_{sc}\left(\varphi, \eta_0 = 1/2\right) = 12\frac{(1-\varphi)\,(2-3\varphi)\sqrt{(1-2\varphi)}}{\sqrt{(3-\varphi)}\,(4-3\varphi)} \tag{3.74}$$

In both cases, (3.73) and (3.74), we recover for $\varphi = 0$ the Von-Mises lower bound solution of the flat punch problem:

$$\lim_{\varphi=0}\frac{H^-_{mt}}{c^s} = \lim_{\varphi=0}\frac{H^-_{sc}}{c^s} = 2\sqrt{3} \tag{3.75}$$

This solution is clearly a lower bound: in comparison to the 'rule-of-thumb' (2.19), $H/Y \simeq 2.8$, the lower bound solution (3.75) predicts $H^-/Y = H^-/\left(\sqrt{3}c^s\right) = 2$. On the other hand, the lower bound solutions allow us to illustrate the effect of the pore morphology on the hardness-to-solid cohesion relation, as displayed in figure 3-7 in form of a plot of H^-/c^s vs. the solid concentration $\eta = 1-\varphi$. The figure is the transposition of figure 2-7 to strength indentation analysis. In particular, it shows that the Mori-Tanaka scheme (MT) provides a continuous relation over the entire range of possible solid concentrations, $0 \leq \eta \leq 1$, while the polycrystal lower bound (SCS) prediction only covers the range between the solid percolation threshold $\eta_0 = 1/2$ and $\eta = 1$. Moreover, a study of the particular behavior of the polycrystal solution (3.74) around the percolation threshold readily reveals that the solution has an infinite slope:

$$\frac{d}{d\varphi}|_{\varphi_0=1/2}\left(\frac{H^-_{sc}}{c^s}\right) \rightarrow \infty \tag{3.76}$$

We keep this in mind for further developments.

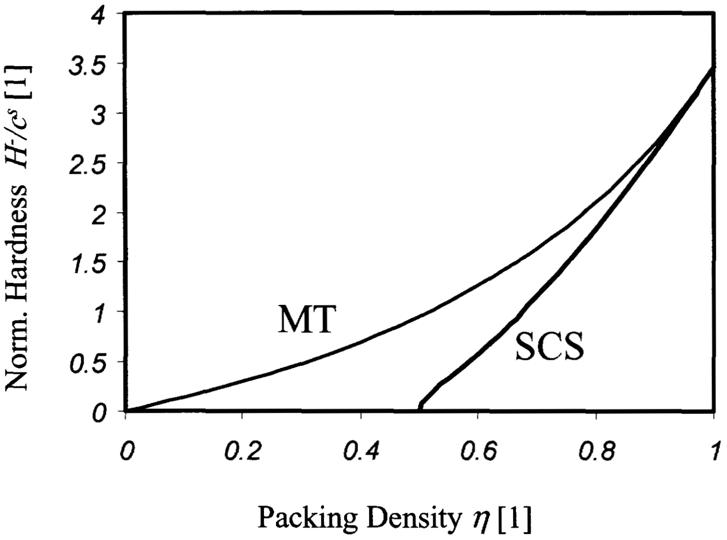

Figure 3-7: Effect of the pore morphology on the Lower Bound hardness-to-solid cohesion relation: 'MT' stands for 'Mori-Tanaka scheme', 'SCS' stands for 'Self-Consistent scheme'.

3.3.3 Drucker-Prager Solid

We consider next the Drucker-Prager solid, for which:

$$A^{DP} = c^s (1-\varphi) \frac{\sqrt{(1-\varphi)\mathcal{K}}}{1-\varphi-\alpha^2\mathcal{K}};\ B^{DP} = c^s (1-\varphi) \sqrt{\frac{\mathcal{M}}{1-\varphi-\alpha^2\mathcal{K}}};\ C^{DP} = -\frac{c^s (1-\varphi)\alpha\mathcal{K}}{1-\varphi-\alpha^2\mathcal{K}} \tag{3.77}$$

For a matrix-pore morphology ($\mathcal{K} = \mathcal{K}_{mt}$,$\mathcal{M} = \mathcal{M}_{mt}$), substitution of (3.77) in (3.69) yields:

$$\frac{H^-_{mt}}{c^s} = 12\frac{(1-\varphi)\left(4\sqrt{(5\varphi+3)}\alpha^2 + (18+12\varphi)\,\alpha + \sqrt{(5\varphi+3)}\,(6+\varphi)\right)}{16\alpha^4 - 4\,(15+16\varphi)\,\alpha^2 + 55\varphi^2 + 93\varphi + 36} \tag{3.78}$$

Similarly, for a polycrystal morphology ($\mathcal{K} = \mathcal{K}_{sc}$,$\mathcal{M} = \mathcal{M}_{sc}$), substitution of (3.77) in (3.69) yields:

$$\begin{aligned}\frac{H^-_{sc}}{c^s} &= 12\,(1-\varphi)\cdot \qquad (3.79)\\ &\frac{\sqrt{(3-\varphi)\,(1-2\varphi)}\left(4\,(1-2\varphi)\,\alpha^2 - 11\varphi + 6 + 3\varphi^2\right) + (1-2\varphi)\left(6\varphi^2 - 24\varphi + 18\right)\alpha}{\left(64\varphi^2 + 16 - 64\varphi\right)\alpha^4 + \left(24\varphi^3 - 124\varphi^2 - 60 + 176\varphi\right)\alpha^2 - 51\varphi - 3\varphi^3 + 22\varphi^2 + 36}\end{aligned}$$

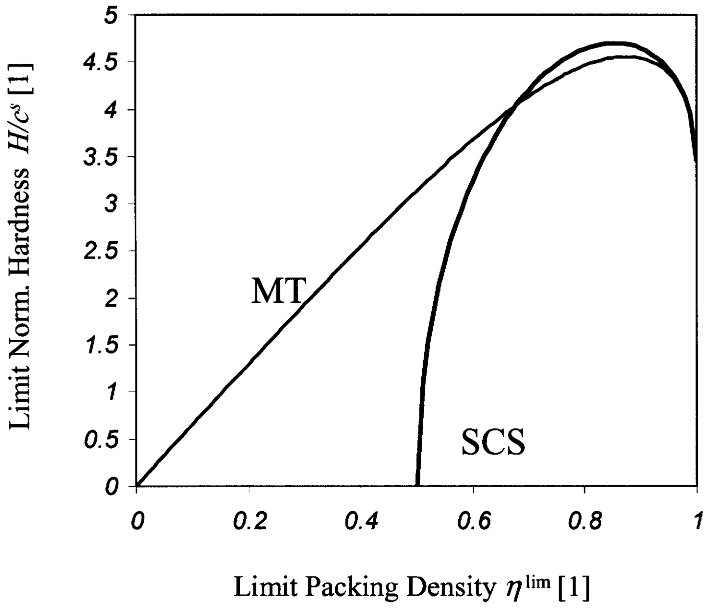

Figure 3-8: Asymptotic Behavior of the lower bound hardness-to-cohesion ratio at the limit packing density η^{lim}. The figure shows that the effect of the pore morphology (MT = Mori-Tanaka, SCS = Self-Consistent) is negligible for high packing densities, for which the composite hardness response is dominated by friction.

Letting $\alpha = 0$, we verify that (3.78) and (3.79) reduce to (3.73) and (3.74), respectively. Furthermore, letting $\varphi = \varphi_{mt}^{\text{lim}}$ from (3.57) into (3.78) yields the following asymptotic behavior of the Mori-Tanaka hardness-to-cohesion ratio at the highest possible solid concentration, $\eta_{mt}^{\text{lim}} = 1 - \frac{4}{3}\alpha^2$:

$$\lim_{\varphi=\varphi_{mt}^{\text{lim}}=1-\eta_{mt}^{\text{lim}}} \frac{H_{mt}^{-}}{c^s} = 3\eta \frac{3\sqrt{3}\sqrt{(1-\eta)} + 2\sqrt{(8-5\eta)}}{5-2\eta} \tag{3.80}$$

Similarly, letting $\varphi = \varphi_{sc}^{\text{lim}}$ from (3.58) in (3.79) yields the asymptotic hardness-to-cohesion ratio at the highest possible packing density $\eta_{sc}^{\text{lim}} = 1 - \left(\frac{3}{2} + 4\alpha^2 - \frac{1}{2}\sqrt{(9 + 32\alpha^2 + 64\alpha^4)}\right)$:

$$\lim_{\varphi=\varphi_{sc}^{\text{lim}}=1-\eta_{sc}^{\text{lim}}} \frac{H_{sc}^{-}}{c^s} = 3\frac{2\sqrt{(-2+3\eta+2\eta^2)} + 3\sqrt{(-2-\eta^2+5\eta-2\eta^3)}}{\eta+2} \tag{3.81}$$

Figure 3-8, which compares the asymptotic behavior of the two lower bounds (3.80) and (3.81), shows that the effect of the pore morphology is rather negligible for high limit packing densities > 65%, corresponding to friction angles of the solid of $0 < \alpha < 0.5$ for a Mori-Tanaka solid phase and $0 < \alpha < 0.8$ for a polycrystal solid. As expected, the two morphologies provide the same asymptotic value for $\eta^{\lim} = 1$, which corresponds to $\alpha = 0$, and for which (3.80) and (3.81) converge to the Von-Mises solid value (3.75). A second limit packing density, for which (3.80) and (3.81) coincide is $\eta^{\lim} = 0.676$, which corresponds to a friction coefficient of $\alpha = \sqrt{3\left(1 - \eta_{mt}^{\lim}\right)/2} = 0.5$ for a Mori-Tanaka pore morphology, and $\alpha = \sqrt{\left(\left(2\eta_{sc}^{\lim} - 1\right)\left(2 - \left(\eta_{sc}^{\lim}\right)^2 - \eta_{sc}^{\lim}\right)\right) / \left(4\eta_{sc}^{\lim} - 2\right)} = 0.785$ for a polycrystal morphology:

$$\lim_{\varphi=\varphi_{mt}^{\lim}} \frac{H_{mt}^{-}}{c^s} = \lim_{\varphi=\varphi_{sc}^{\lim}} \frac{H_{sc}^{-}}{c^s} = 4.034\,1 > 2\sqrt{3} \tag{3.82}$$

On first sight, it may be surprising that the H^{-}/c^s for high packing densities are actually higher than the pure Von-Mises solid value (3.75). This paradox is readily explained by the fact that H/C of a cohesive-frictional solid increases with the friction angle (see Section 2.2.2 and Fig. 2-4). Therefore, the results in Figure 3-8 show that the friction angle dominates the asymptotic behavior for high packing density. In return, as the material becomes increasingly porous, the effect of the solid's friction vanishes to the benefit of the specific pore morphology, which dominates the limit behavior at lower limit solid concentrations (corresponding to 'high' (i.e. unrealistic) friction coefficients).

Moreover, the limit behavior provides a convenient way to compare the effect of morphology on the hardness-to-cohesion ratio for cohesive-frictional porous materials. Instead of comparing the response for the same friction coefficient, it is more appropriate to compare the response for the same limit packing density, by replacing in (3.78) and (3.79) α by $\eta_{mt}^{\lim}$ and $\eta_{sc}^{\lim}$, respectively. This yields for the Mori-Tanaka morphology:

$$\frac{H_{mt}^{-}}{c^s} = 12\eta \frac{(15 - 6\eta)\sqrt{3\left(1 - \eta_{mt}^{\lim}\right)} + \sqrt{(8 - 5\eta)}\left(10 - \eta - 3\eta_{mt}^{\lim}\right)}{9\left(\eta_{mt}^{\lim}\right)^2 + 75\eta_{mt}^{\lim} - 48\eta_{mt}^{\lim}\eta - 155\eta + 100 + 55\eta^2} \tag{3.83}$$

(The expression for the polycrystal morphology is quite lengthy and is therefore omitted). Figure 3-9 displays the hardness-to-cohesion ratio for $\eta_{mt}^{\lim} = \eta_{sc}^{\lim} = 0.676$ in the interval $\eta \in \left[\eta_0, \eta^{\lim}\right]$ (where η_0 stands for the percolation threshold: $\eta_0 = 0$ for Mori-Tanaka morphology,

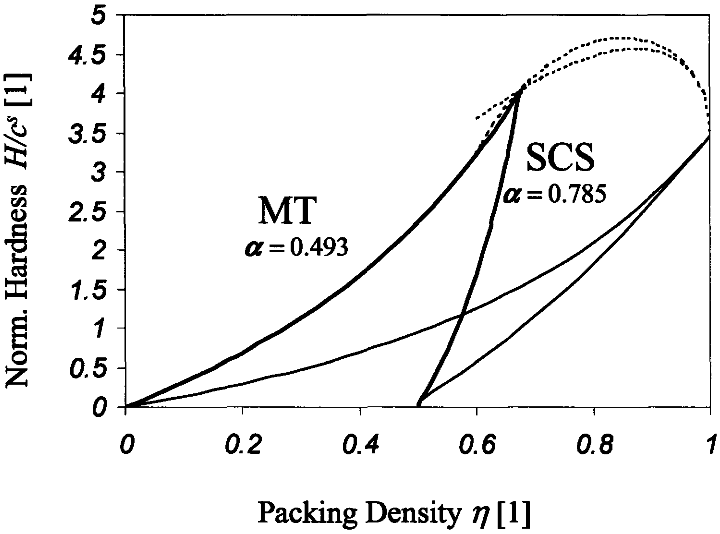

Figure 3-9: Lower bound hardness-to-cohesion ratio for two cohesive materials of different morphology (MT = Mori-Tanaka, SCS = Self-Consistent) and different friction coefficients α, but same limit packing density $\eta_{mt}^{\lim} = \eta_{sc}^{\lim} = 0.676$. For comparison, the figure also displays the $\alpha = 0$ case, for which $\eta_{mt}^{\lim} = \eta_{sc}^{\lim} = 1$.

$\eta_0 = 1/2$ for polycrystal morphology).

3.4 Chapter Summary

In this Chapter we developed a multi-scale indentation strength approach for cohesive-frictional *porous* materials. The approach is based on recent progress in the field of nonlinear strength homogenization of porous materials. The separation of scale condition between the macroscopic scale of the indentation analysis and the microscopic scale of the components of the porous *rev* allows us to derive estimates of the homogenized yield function of a porous material while considering both the strength properties of the cohesive-frictional solid and the particular morphology of the porous microstructure, namely a matrix-pore inclusion morphology (Mori-Tanaka scheme) and a polycrystal morphology. The results obtained with these models in a lower bound estimate of a flat indenter shows the potential of this novel approach to determine the hardness-to-solid cohesion relation from the limit theorems of yield design:

$$\frac{H^-}{c^s} \leq \frac{H}{c^s} = \mathcal{F}\left(\alpha, \varphi, \eta_0, \theta\right) \leq \frac{H^+}{c^s} \tag{3.84}$$

In particular, the lower bound results reveal that the presence of friction in highly compacted solids leads to an increase of H/c^s compared to the solid-only situation. These results need now to be confirmed with an upper bound approach based on kinematically admissible velocity fields. While the theory is now in place, it is quite difficult to develop analytically the upper bound for the indentation test in closed-form. For this reason, the next Chapter presents an original numerical implementation of the multi-scale upper bound approach. The comparison of this upper bound with the lower bound developed here is discussed in Chapter 5.

Chapter 4

Computational Implementation of the Upper Bound

> '*Problems of axi-symmetrical plastic flow cannot, in general, be solved by the method of characteristics (slip lines) as in plane strain*' (Johnson, 1985, page 168).

The very difficulty of solving the plastic flow problem in axi-symmetrical conditions, as noted by Johnson in his classical book on contact mechanics [46], motivates the development of a computational strategy to implement the Upper Bound of yield design for the analysis of the hardness-to-cohesion ratio of cohesive-frictional porous materials. Given the limited possibilities for analytical solutions (such as slip-line solutions), the beneficial use of a continuum discretization into finite elements together with linear programming techniques was early on recognized for the implementation of both the lower bound theorem for plane-stress conditions [54], [57], [58] and the upper bound theorem for plane-strain conditions [2], [33], [76], [8]. The most advanced implementation is due to Sloan and co-worker combining (plane stress/plane strain) 2-D or 3-D linear finite element formulations with linear and non-linear programming [65], [66], [67], [52], [53], [48]. We employ a similar strategy for the axi-symmetrical conditions of the indentation test. The axi-symmetrical discretization by finite elements is identical to the one developed by Ganneau and Ulm [36] for conical indentation analysis in a Mohr-Coulomb material (see Section 2.2.2). The originality of our approach is the numerical implementation of the discretized dissipation function of the elliptical (Cam-Clay type) strength criterion in form of a second-order 'conic' optimization problem, for which advanced numerical solvers became recently available.

4.1 Governing Equations

The upper bound problem we want to solve is the defined by (3.64) and (3.12). Restated as a minimization problem, it reads:

$$\boxed{\begin{array}{c} \dfrac{H}{c^s} = \mathcal{F}\left(\alpha, \varphi, \eta_0, \theta\right) = \dfrac{1}{A_c} \min_{\underline{U}'\, KA} \displaystyle\int_{\Omega} \left(\sqrt{\mathcal{A}^2 D_v'^2 + 4\mathcal{B}^2 D_d'^2} + \mathcal{C} D_m' \right) d\Omega \leq \dfrac{H^+}{c^s} \\ \\ \text{subject to (s.t.):} \\ \\ \forall \left(r, z\right) \in A_M;\ \underline{U}' \cdot \underline{n} = -\sin\theta \\ \left(r, z\right) \to \infty;\ \underline{U}' = 0 \end{array}} \tag{4.1}$$

The coefficients $\mathcal{A}$, $\mathcal{B}$ and $\mathcal{C}$ are the pore morphology parameters summarized in Table 3.2. We recall that $A_c = A_M \sin\theta$ is the projected contact area of the conical indenter (half-apex angle θ) with the 'deformed' infinite half-space Ω, when the indenter is at an indentation depth h (see Fig. 2-3). It is assumed to be known. Furthermore, $\underline{U}' = \underline{U}'\left(\underline{x}\right)$ is the plastic velocity field normalized by the indentation rate $\overset{\circ}{h} = 1$ taken as reference. $\underline{U}'$ belongs to a space of kinematically admissible (KA) velocity fields which satisfy the zero-velocity boundary condition at infinity of the studied domain, as well as the frictionless contact conditions at the indenter-material interface. Those conditions are constraints in the optimization problem (4.1). Finally, the invariants of the strain rate field $\mathbf{D}'\left(\underline{x}\right) = \frac{1}{2}\left(\operatorname{grad}\underline{U}' + {}^t\operatorname{grad}\underline{U}'\right)$ derive from the velocity field:

$$\begin{aligned} D_v' &= \operatorname{tr}\mathbf{D}' = \operatorname{div}\underline{U}' \\ D_d'^2 &= \tfrac{1}{2}\boldsymbol{\Delta}' : \boldsymbol{\Delta}' = \tfrac{1}{2}\mathbf{D}' : \mathbb{K} : \mathbf{D}' \end{aligned} \tag{4.2}$$

where $\mathbb{K} = \mathbb{I} - \frac{1}{3}\mathbf{1} \otimes \mathbf{1}$ is the forth-order deviator tensor projection of the unit tensor $I_{ijkl} = \frac{1}{2}\left(\delta_{ik}\delta_{jl} + \delta_{il}\delta_{jl}\right)$ which obeys to $\mathbb{K} : \mathbb{K} = \mathbb{K}$. The implementation of this upper bound problem requires on the one side the discretization of the material domain Ω, and on the other hand an efficient formulation to solving the optimization problem. This is the focus of this Chapter.

4.2 Space Discretization by Finite Elements

4.2.1 Assumptions

Using a finite element discretization comes to replacing the infinite half-space Ω by a bounded domain Ω'. A further simplification consists of modeling the 'deformed' surface as a flat surface, when the indenter is at a given indentation depth h. This amounts to neglecting in the evaluation of the overall dissipation capacity (4.1) of the material bulk the contribution of localized regions around the indenter undergoing pile-up or sink-in (see Fig. 4-1). However, compared to the material bulk volume that contributes to the overall dissipation capacity, the additional contribution of the pile-up or sink-in material volume $\delta\Omega$ is expected to be of second-order in the evaluation (4.1) of the maximum dissipation the porous material system can afford. In other words, the dissipation capacity of the porous material system is determined for a fixed 'undeformed' geometry, and the projected contact area is readily determined from the cone geometry (see Section 2.1.2) as $A_c = \pi \left(h \tan\theta\right)^2$. Of course, for any practical application in indentation analysis, the piling-up or sinking-in phenomena cannot be neglected in the evaluation of the hardness value from its definition (1.1). Finally, making use of the axi-symmetry of the geometry of the indentation depth, all developments below are developed in 2-D cylinder coordinates (r, z).

4.2.2 Finite Element Discretization

The velocity field $\underline{U}'$ in Ω' is discretized in the form:

$$U_i' = \sum_k N_k\left(r, z\right) u_i^k \tag{4.3}$$

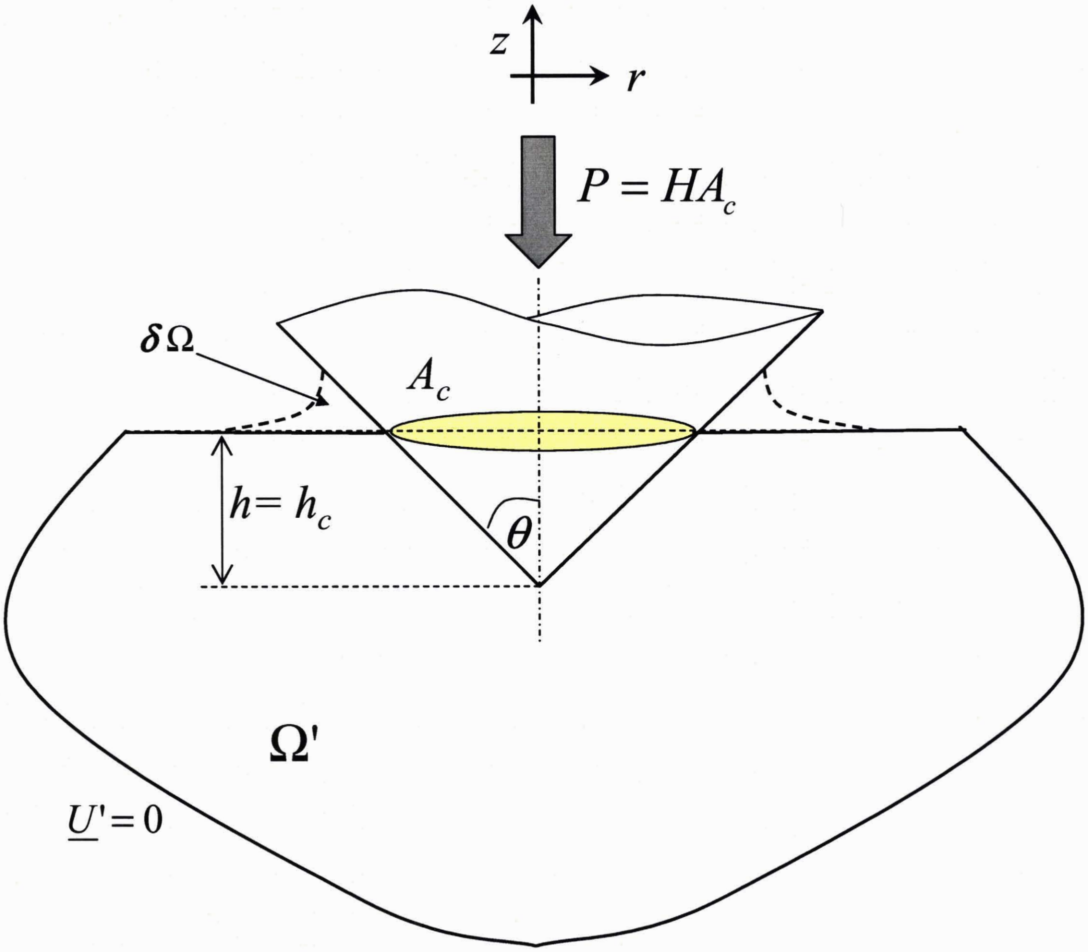

Figure 4-1: Modeling assumption in the application of yield design for indentation analysis. The analysis is carried out on a fixed 'undeformed' geometry, which neglects the dissipation contribution of the pile-up (or sink-in) volume $\delta\Omega$.

where u_i^k are the nodal velocities and N_k are linear shape functions. We restrict ourselves to linear three-node triangle elements, for which (4.3) is written in the form:

$$\begin{aligned} u_r &= \sum_{k=1}^{3} N_k u_r^k \\ u_z &= \sum_{k=1}^{3} N_k u_z^k \end{aligned} \tag{4.4}$$

where $\left(u_r^k, u_z^k\right)$ are nodal velocities in the r- and z-directions, respectively, and N_k are the following linear shape functions expressed in terms of the nodal coordinates (r_i, z_i):

$$\begin{aligned} N_1 &= \frac{(r_2 z_3 - r_3 z_2) + z_{23} r + r_{32} z}{2A_{el}} \\ N_2 &= \frac{(r_3 z_1 - r_1 z_3) + z_{31} r + r_{13} z}{2A_{el}} \\ N_3 &= \frac{(r_1 z_2 - r_2 z_1) + z_{12} r + r_{21} z}{2A_{el}} \end{aligned} \tag{4.5}$$

where $r_{32} = r_3 - r_2 \qquad z_{23} = z_2 - z_3$

$r_{13} = r_1 - r_3 \qquad z_{31} = z_3 - z_1$

$r_{21} = r_2 - r_1 \qquad z_{12} = z_1 - z_2$, and $2A = |(r_1 - r_3)(z_2 - z_3) - (r_3 - r_2)(z_3 - z_1)|$ is twice the triangle area. The 'volume' of the axi-symmetric triangle is given by:

$$\begin{aligned} V &= 2\pi r_c A = 2\pi A \tfrac{r_1 + r_2 + r_3}{3} \\ &= |(r_1 - r_3)(z_2 - z_3) - (r_3 - r_2)(z_3 - z_1)|\, \pi \tfrac{r_1 + r_2 + r_3}{3} \end{aligned} \tag{4.6}$$

4.2.3 Constraints From Velocity Boundary and Frictionless Contact Conditions

The application of a finite element discretization lends itself readily for the implementation of the boundary and contact conditions in (4.1). Instead of prescribing zero-velocity boundary conditions at infinity, they are prescribed on all nodes (r_i, z_i) situated at the (finite) edges $\partial\Omega'$

of the discretized domain Ω' (see Fig. 4-2):

$$\partial\Omega_{V^d} = \begin{cases} \forall r_i = r_M & u_r^i = u_z^i = 0 \\ \forall z_i = 0 & u_r^i = u_z^i = 0 \\ \forall r_i = 0 & u_r^i = 0 \end{cases} \tag{4.7}$$

(the last condition is the velocity condition along the symmetry axis in the 2-D cylinder coordinate system).

Similarly, the frictionless contact condition along the indenter – material interface I, can be written in the form:

$$\forall i \in I \qquad -\cos(\theta)u_r^i + \sin(\theta)u_z^i = -\overset{\circ}{h}\sin(\theta) \tag{4.8}$$

This contact condition implies that the whole optimization problem is proportional to $\overset{\circ}{h}$ and that the optimal solution $P\overset{\circ}{h}$ is proportional to $\overset{\circ}{h}$. In other words, $\overset{\circ}{h}$ is a dummy variable, which we set equal to $\overset{\circ}{h} = 1$. Both boundary and contact conditions are linear constraints in the optimization problem, which can be written in the compact form:

$$[A_1]\,(u) - (b_1) = 0 \tag{4.9}$$

where $[A_1]$ is the constraint matrix, $[u]$ are the velocity unknowns on $\partial\Omega_{V^d}$ and I, and vector $[b_1]$ assembles the constraints (0 on $\partial\Omega_{V^d}$, $-\sin\theta$ on I).

4.2.4 Discretization of Dissipation Function

Using the classical notation of displacement-based finite element formulation (see e.g. [4]) which is here applied to the velocity formulation, the components of the strain rate tensor are given by:

$$(D') = [B]^T\,(u) \tag{4.10}$$

where $(D') = (D'_{rr}, D'_{\theta\theta}, D'_{zz}, D'_{rz})^T$ are the components of the strain rate tensor written in vector form:

$$(D')^T = \left(\frac{\partial u_r}{\partial r}, \frac{u_r}{r}, \frac{\partial u_z}{\partial z}, \frac{1}{2}\left(\frac{\partial u_r}{\partial z} + \frac{\partial u_z}{\partial r}\right)\right) \tag{4.11}$$

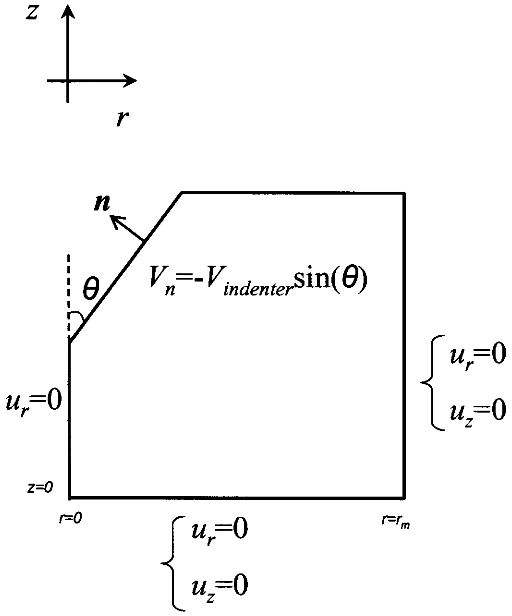

Figure 4-2: Boundary conditions for the optimization problem leading to an upper bound of the exact limit load.

$[B]$ is the strain rate-velocity matrix (equivalent to the strain-displacement matrix in the FEM). For the chosen linear interpolation (4.5), $[B]$ is constant per element. This simplifies the calculations. For instance, the volume strain rate can be expressed as:

$$D'_v = \operatorname{tr}\mathbf{D}' = \frac{\partial u_r}{\partial r} + \frac{u_r}{r} + \frac{\partial u_z}{\partial z} = [B_v]^T (u) \tag{4.12}$$

where $[B_v]$ is the vector:[1]

$$[B_v] = \begin{bmatrix} \frac{2\pi A}{3V} + \frac{\partial N_1(r,z)}{\partial r} \\ \frac{\partial N_1(r,z)}{\partial z} \\ \frac{2\pi A}{3V} + \frac{\partial N_2(r,z)}{\partial r} \\ \frac{\partial N_2(r,z)}{\partial z} \\ \frac{2\pi A}{3V} + \frac{\partial N_3(r,z)}{\partial r} \\ \frac{\partial N_3(r,z)}{\partial z} \end{bmatrix} \tag{4.13}$$

and (u) the nodal velocity vector:

$$(u)^T = \begin{pmatrix} u_r^1 & u_z^1 & u_r^2 & u_z^2 & u_r^3 & u_r^3 \end{pmatrix} \tag{4.14}$$

Similar, the shear strain rate invariant can be obtained from:

$$D_d'^2 = \frac{1}{2}\mathbf{\Delta}' : \mathbf{\Delta}' = \frac{1}{2}(u)^T [B_d] [B_d]^T (u)^T \tag{4.15}$$

where $[B_d]$ is a 6×4 matrix of constant coefficients which links the components of the strain deviator tensor to the nodal velocity vector, $\left(\Delta_j'\right) = [B_d]^T (u)^T$. If we substitute (4.12) and (4.15) in the dissipation function (3.62) of the porous material, we obtain a means to evaluate the contribution of each triangle element to the overall dissipation capacity:

$$\int_V \Pi^{est}(\mathbf{D}')\, dV = c^s \left(\sqrt{(u)^T [\mathrm{BB}] (u)^T} + \mathcal{C} [B]^T (u) \right) V \tag{4.16}$$

where [BB] is the 6×4 matrix:

$$[\mathrm{BB}] = \mathcal{A}^2 [B_v] [B_v]^T + 4\mathcal{B}^2 [B_d] [B_d]^T \tag{4.17}$$

---

[1] For constant strain per three-node triangle element (volume V, section A) we note that:

$$D_{\theta\theta}' = \frac{1}{V}\int_V \left(\frac{u_r}{r}\right) r dr d\theta dz = \frac{2\pi A}{3V}\left(u_r^1 + u_r^2 + u_r^3\right)$$

4.3 Formulation of the Optimization Problem

4.3.1 Problematique

With the spacial discretization in hand, we can reformulate the problem (4.1) as follows:

$$\boxed{\begin{array}{c} \dfrac{H}{c^s} = \min\limits_{(u)} \dfrac{1}{A_c} \sum\limits_{el} \left(\sqrt{(u)^T \, [\mathrm{BB}] \, (u)^T} + \mathcal{C} \, [B]^T \, (u) \right) V \\ \\ \text{s.t.} \\ \\ [A_1] \, (u) - (b_1) = 0 \end{array}} \tag{4.18}$$

This minimization problem is far from trivial, as it involves as objective function a quadratic term that cannot be handled with the classical tools of linear optimization. The following brief review inspired by [59] and [62] of three major optimization classes, namely the Linear Optimization, the Semi-Definite Optimization and the Second-Order Conic Optimization, will provide the necessary background for solving this problem. Some additional background is given in Appendix B.

4.3.2 Optimization Classes

The first step to solving an optimization problem amounts to identifying the optimization class to which the problem belongs. Knowledge of the optimization class allows one to choose the corresponding class of solvers, if such a solver exists. Choosing a solver that is adapted to one's problem has two main advantages. First, there is no need to adapt one's problem to the solver by means of approximations. Then, the solver will be efficient and the problem can be solved in an optimal time.

Linear Optimization (LO)

The simplest optimization problem is the linear problem. The standard Linear Optimization problem can be written as:

$$\begin{array}{ll} \text{(LO)} & \min c^T x \\ \text{s.t.} & x \geq 0 \\ & Ax = b \end{array} \tag{4.19}$$

where $A \in \mathbb{R}^{m \times n}$, $b \in \mathbb{R}^m$, $c \in \mathbb{R}^n$.

Semi-Definite Optimization (SDO)

Linear Optimization is a simplification of a more general class of problems, the Semi-Definite Optimization problem, which has the following standard form:

$$\begin{array}{ll} \text{(SDO)} & \min Tr(CX) \\ \text{s.t.} & Tr(A_i X) = b_i \ , \ i = 1, ..., m \\ & X \succeq 0 \end{array} \tag{4.20}$$

where A_i are symmetric $n \times n$ matrices, and $b \in \mathbb{R}^m$. Furthermore, $X \succeq 0$ means that X is a symmetric positive semi-definite matrix. The matrices are assumed to be linearly independent.

Second-Order Conic Optimization (SOCO)

Second Order Cone Optimization, which is a particular case of Semi-Definite Optimization, is the problem of minimizing a linear objective function subject to the intersection of an affine set and the direct product of several second-order cones. The standard SOCO problem takes the following mathematical form:

$$\begin{array}{ll} \text{(SOCO)} & \min c^T x \\ \text{s.t.} & Ax = b \\ & x \in K \end{array} \tag{4.21}$$

where K is the product of several second-order cones, that is, $K = K^1 \times K^2 \times ... \times K^N$ with

$$K^j = \left\{ x \in \mathbb{R}^{n_j} : \sum_{i=2}^{n_j} \left(x_i^j\right)^2 \leq \left(x_1^j\right)^2 \text{ and } x_1^j \geq 0 \right\} \tag{4.22}$$

From a pure mathematical point of view, the constraint function defining the second-order cone K^j is nothing more than some specific quadratic functions.

For the solution of those optimization problems, two main methods are available: the Simplex Method (SM) and the Interior Point Method (IPM). The Simplex Method has been the main method to solve Linear Problems, while the Interior Point Method allows solving more complex problems such as nonlinear convex programming, semi-definite optimization (SDO) and second-order conic optimization (SOCO). In particular, IPMs appear to be the first and also most efficient approach for SDO. SDO and IPM are today a very active area of research in mathematical programming.

4.3.3 Reformulation as Convex Conic Problem

After this brief presentation about optimization, we can now return to developing a strategy for solving (4.18). While the term $\min_{(u)} \mathcal{C} D'_m = \min \mathcal{C} [B]^T (u)$ is readily recognized as a Linear Problem, the quadratic term $\sqrt{\mathcal{A}^2 D_v'^2 + 4\mathcal{B}^2 D_d'^2} = \min_{(u)} \sqrt{(u)^T [\text{BB}] (u)^T}$ defies the classification in one of the three optimization classes. On the other hand, let us rewrite the problem (4.1) in a slightly modified form:

$$\boxed{\begin{array}{l} \dfrac{H}{c^s} = \min\limits_{(u,z)} \dfrac{1}{A_c} \sum\limits_{el} \left(z + \mathcal{C} D'_m\right) V \\ \\ \text{s.t.} \quad \begin{cases} [A_1]\,(u) - (b_1) = 0 \\ z \geq \sqrt{\mathcal{A}^2 D_v'^2 + 4\mathcal{B}^2 D_d'^2} \end{cases} \end{array}} \tag{4.23}$$

This problem is equivalent to the original problem and is recognized to be of the form (4.21), i.e. a Second-Order Conic Problem.

4.4 Implementation in MOSEK

In general, before solving an optimization problem, data is gathered and prepared. Then, the data is communicated to the optimization software. Finally, once the solution has been obtained by the solver, it is analyzed. A popular software tool for doing all those tasks is MATLAB. However, MATLAB has the disadvantage that it is slow at solving optimization problems. In particular, solving large-scale sparse problems might be time consuming if not impossible using MATLAB and in any case, MATLAB can not handle the optimization of a Second-Order Conic problem. On the other hand, MOSEK which is the name of a set of optimizer, can deal with a lot of various optimization problems [85]. In particular, one of MOSEK's optimizers in specialized in SOCO problems and can deal with large-scale and sparse problems [84]. Therefore, MOSEK optimizers seem to be a very good choice to solve our optimization problem (4.23).

The MOSEK optimizers can be used from different sources. For example, it can be used from a C routine. An optimization toolbox has also been created which makes it possible to use the MOSEK optimizers from within the MATLAB environment, so that the MOSEK optimizers are used as ordinary MATLAB functions. This combination MOSEK / MATLAB is very convenient: the MATLAB environment is very user-friendly and intuitive, and the optimization problem is solved much faster with MOSEK than with MATLAB. This efficiency comes from the fact that the MOSEK optimizer is written in C and works as an independent black box that uses the inputs given by MATLAB and delivers the outputs to MATLAB.

For these reasons, the MATLAB environment will be used to write, with the MOSEK formalism, the discrete formulation of the optimization problem.

4.4.1 MOSEK Formalism

In order to use MOSEK, the conic optimization problem must be presented in the following form:

$$\left\{ \begin{array}{l} \min c^T x + c^f \\ \text{s.t.} \left\{ \begin{array}{c} l^c \leq Ax \leq u^c \\ l^x \leq x \leq u^x \\ x \in C \end{array} \right. \end{array} \right. \tag{4.24}$$

where C is a set of quadratic cones and rotated quadratic cones. The mathematical definition of C is as follows:

Let $x^t \in R^{n^t}, t = 1, ..., k$ be vectors comprised of parts of the decision variables x such that each decision variable is a member of exactly one vector x^t. C is defined as: $C := \{x \in \mathbb{R}^n, x^t \in C_t, t = 1, 2, ..., k\}$, where: C_t is a quadratic cone

$$C_t = \left\{ x \in R^{n^t} : x_1 \geq \sqrt{\sum_{j=2}^{n^t} x_j^2} \right\}, \tag{4.25}$$

or a rotated quadratic cone

$$C_t = \left\{ x \in \mathbb{R}^{n^t} : 2x_1x_2 \geq \sum_{j=3}^{n^t} x_j^2, x_1, x_2 \geq 0 \right\}. \tag{4.26}$$

Through the MATLAB interface, the definition of a cone is done in two steps. First, the type of the cone (quadratic cone or rotated quadratic cone) is specified. Then the indices of the variables playing a role in the cone are given. For example, if the cone is defined as:

$$K = \left\{ x \in \mathbb{R}^n : (x_1)^2 \geq \sum_{i=2}^{n} (x_i)^2 \text{ and } x_1 \geq 0 \right\} \tag{4.27}$$

then the indices order is $[1, 2, ..., n]$.

4.4.2 Discrete Formulation with Additional Cones

Let us define the cone we need to consider for each triangle i. In addition to the nodal velocities, we have z as an additional unknown; hence:

$$K^i = \left\{ \left(z^i, \left(\begin{array}{cccccc} u_r^1 & u_z^1 & u_r^2 & u_z^2 & u_r^3 & u_r^3 \end{array} \right)^i \right) \in \mathbb{R}^7 : \mathcal{A}^2 \left(D_v^i\right)^2 + \mathcal{B}^2 \left(2D_d^i\right)^2 \leq z^2 \text{ and } z \geq 0 \right\} \tag{4.28}$$

This cone is not defined directly by the unknowns but is defined with non-linear functions of the unknowns $\left(z, \left(\begin{array}{cccccc} u_r^1 & u_z^1 & u_r^2 & u_z^2 & u_r^3 & u_r^3 \end{array} \right)\right)$. In order to adapt our problem to the MOSEK formalism, we will introduce additional cones, which replace the original cone $\mathcal{A}^2 \left(D_v^i\right)^2 +$

$4\mathcal{B}^2\left(D_d^i\right)^2 \leq z^2$. This may seem at first counter intuitive, since adding new unknowns may appear to complicate the problem and to slow the computational solution. However, since our optimization formulation is a Second-Order Cone problem, and since MOSEK is specialized in solving that kind of problem, the addition of appropriate new unknowns defining cones will turn out to be a perfect match for our implementation in MOSEK.

The Nonlinear Functions D_v and D_d

For each element (section A), we develop the expressions (4.12) and (4.15) of D_v and D_d as follows:

$$\begin{aligned} D_v &= u_r^1\frac{z_2 - z_3}{2A} + u_r^2\frac{z_3 - z_1}{2A} + u_r^3\frac{-z_2 + z_1}{2A} + \frac{u_r^1 + u_r^2 + u_r^3}{r_1 + r_2 + r_3} \\ &\quad + u_z^1\frac{r_3 - r_2}{2A} + u_z^2\frac{r_1 - r_3}{2A} + u_z^3\frac{r_2 - r_1}{2A} \end{aligned} \tag{4.29}$$

$$\begin{aligned} D_d^2 &= \left(\tfrac{1}{3}u_r^1\tfrac{z_2-z_3}{2A} + \tfrac{1}{3}u_r^2\tfrac{z_3-z_1}{2A} + \tfrac{1}{3}u_r^3\tfrac{-z_2+z_1}{2A} - \tfrac{1}{6}u_z^3\tfrac{r_2-r_1}{2A} - \tfrac{1}{6}u_z^2\tfrac{r_1-r_3}{2A} - \tfrac{1}{6}u_z^1\tfrac{r_3-r_2}{2A} - \tfrac{1}{6}\tfrac{u_r^1+u_r^2+u_r^3}{r_1+r_2+r_3}\right)^2 \\ &+ \left(\tfrac{1}{2}u_r^1\tfrac{r_3-r_2}{2A} + \tfrac{1}{2}u_r^2\tfrac{r_1-r_3}{2A} + \tfrac{1}{2}u_r^3\tfrac{r_2-r_1}{2A} + \tfrac{1}{2}u_z^1\tfrac{z_2-z_3}{2A} + \tfrac{1}{2}u_z^1\tfrac{z_3-z_1}{2A} + \tfrac{1}{2}u_z^3\tfrac{-z_2+z_1}{2A}\right)^2 \\ &+ \left(\tfrac{1}{3}\tfrac{u_r^1+u_r^2+u_r^3}{r_1+r_2+r_3} - \tfrac{1}{6}u_z^3\tfrac{r_2-r_1}{2A} - \tfrac{1}{6}u_z^2\tfrac{r_1-r_3}{2A} - \tfrac{1}{6}u_z^1\tfrac{r_3-r_2}{2A} - \tfrac{1}{6}u_r^3\tfrac{-z_2+z_1}{2A} - \tfrac{1}{6}u_r^2\tfrac{z_3-z_1}{2A} - \tfrac{1}{6}u_r^1\tfrac{z_2-z_3}{2A}\right)^2 \\ &+ \left(\tfrac{1}{3}u_z^1\tfrac{r_3-r_2}{2A} + \tfrac{1}{3}u_z^2\tfrac{r_1-r_3}{2A} + \tfrac{1}{3}u_z^3\tfrac{r_2-r_1}{2A} - \tfrac{1}{6}\tfrac{u_r^1+u_r^2+u_r^3}{r_1+r_2+r_3} - \tfrac{1}{6}u_r^3\tfrac{-z_2+z_1}{2A} - \tfrac{1}{6}u_r^2\tfrac{z_3-z_1}{2A} - \tfrac{1}{6}u_r^1\tfrac{z_2-z_3}{2A}\right)^2 \end{aligned} \tag{4.30}$$

An interesting observation is that D_d^2 is the sum of four functions, which are squared functions of linear functions in the velocity unknowns. Therefore, in order to define the original cone $\mathcal{A}^2\left(D_v^i\right)^2 + \mathcal{B}^2\left(2D_d^i\right)^2 \leq z^2$, we are led to add for each triangle new unknowns in order to describe new cones. The additional unknowns we introduce are $(d_1, d_2, d_3, d_4, d_5)$:

$$d_1 = \mathcal{A}D_m \tag{4.31}$$

$$\begin{cases} d_2 = 2\mathcal{B}\left(\frac{1}{3}u_r^1\frac{z_2-z_3}{2A} + \frac{1}{3}u_r^2\frac{z_3-z_1}{2A} + \frac{1}{3}u_r^3\frac{-z_2+z_1}{2A} - \frac{1}{6}u_z^3\frac{r_2-r_1}{2A} - \frac{1}{6}u_z^2\frac{r_1-r_3}{2A} - \frac{1}{6}u_z^1\frac{r_3-r_2}{2A} - \frac{1}{6}\frac{u_r^1+u_r^2+u_r^3}{r_1+r_2+r_3}\right) \\ d_3 = 2\mathcal{B}\left(\frac{1}{2}u_r^1\frac{r_3-r_2}{2A} + \frac{1}{2}u_r^2\frac{r_1-r_3}{2A} + \frac{1}{2}u_r^3\frac{r_2-r_1}{2A} + \frac{1}{2}u_z^1\frac{z_2-z_3}{2A} + \frac{1}{2}u_z^1\frac{z_3-z_1}{2A} + \frac{1}{2}u_z^3\frac{-z_2+z_1}{2A}\right) \\ d_4 = 2\mathcal{B}\left(\frac{1}{3}\frac{u_r^1+u_r^2+u_r^3}{r_1+r_2+r_3} - \frac{1}{6}u_z^3\frac{r_2-r_1}{2A} - \frac{1}{6}u_z^2\frac{r_1-r_3}{2A} - \frac{1}{6}u_z^1\frac{r_3-r_2}{2A} - \frac{1}{6}u_r^3\frac{-z_2+z_1}{2A} - \frac{1}{6}u_r^2\frac{z_3-z_1}{2A} - \frac{1}{6}u_r^1\frac{z_2-z_3}{2A}\right) \\ d_5 = 2\mathcal{B}\left(\frac{1}{3}u_z^1\frac{r_3-r_2}{2A} + \frac{1}{3}u_z^2\frac{r_1-r_3}{2A} + \frac{1}{3}u_z^3\frac{r_2-r_1}{2A} - \frac{1}{6}\frac{u_r^1+u_r^2+u_r^3}{r_1+r_2+r_3} - \frac{1}{6}u_r^3\frac{-z_2+z_1}{2A} - \frac{1}{6}u_r^2\frac{z_3-z_1}{2A} - \frac{1}{6}u_r^1\frac{z_2-z_3}{2A}\right) \end{cases} \tag{4.32}$$

We can now define the cones.

Cone to Define D_d

The first cone we define expresses the link between $4\mathcal{B}^2\left(D_d^i\right)^2$ and the additional unknowns (d_2, d_3, d_4, d_5). A 6th additional unknown d_6 is then created as $d_6^2 = \left(2\mathcal{B}D_d^i\right)^2$. These unknowns belong to the quadratic cone C^t:

$$C_t^1 = \left\{(d_2, d_3, d_4, d_5, d_6) \in R^5 : d_6 \geq \sqrt{d_2^2 + d_3^2 + d_4^2 + d_5^2}\right\} \tag{4.33}$$

The Original Cone

A second cone is defined to express the original cone, i.e. the square-root of the original objective function. This quadratic cone is defined as:

$$C_t^2 = \left\{(d_1, d_6, d_7) \in R^3 : d_7 \geq \sqrt{d_1^2 + d_6^2}\right\} \tag{4.34}$$

With the formalism of MOSEK, the same unknown cannot belong to several cones at the same time. We thus introduce an additional unknown $d_7 = d_6$ and then redefine the cone:

$$C_t^{2bis} = \left\{(d_1, d_7, d_8) \in R^3 : d_8 \geq \sqrt{d_1^2 + d_7^2}\right\} \tag{4.35}$$

This last cone C_t^{2bis} corresponds to $z^2 \geq \mathcal{A}^2\left(D_v^i\right)^2 + 4\mathcal{B}^2\left(D_d^i\right)^2$. The linear relation $d_7 = d_6$ will be taken into account as an additional linear constraint in the optimization problem.

Modification of the Objective Function

In a last step, we redefine the volumetric term in the objective function, $\mathcal{C}D'_m = \mathcal{C}/\mathcal{A}\, d_1$. The final objective function is then defined by a 9th unknown d_9 which is the following linear combination:

$$d_9 = d_8 + \frac{\mathcal{C}}{\mathcal{A}} d_1 \tag{4.36}$$

This linear relation correspond to the objective function $z + \mathcal{C}D'_m$ which represents the dissipation capacity now as a linear equality. This equality is implemented as a linear constraint in the optimization problem.

4.4.3 Summary

The solver MOSEK eventually deals with the following problem:

$$\boxed{\begin{cases} \frac{H}{c^s} = \frac{1}{A_c} \min\limits_{x=(U,d)} \sum_{el} d_9 V \\ \text{s.t.} \begin{cases} Rx = S \\ l^x \leq x \leq u^x \\ x \in \bigcup\limits_t \left(C_t^1 \cup C_t^{2bis} \right) \end{cases} \end{cases}} \tag{4.37}$$

where x is the vector that has as unknowns the nodal velocities and the nine additional unknowns that define the cones, i.e. for each element:

$$x^T = \left(\begin{pmatrix} u_r^1 & u_z^1 & u_r^2 & u_z^2 & u_r^3 & u_r^3 \end{pmatrix} \begin{pmatrix} d_1 & d_2 & \dots & d_8 & d_9 \end{pmatrix} \right) \in \mathbb{R}^{15} \tag{4.38}$$

The linear constraint $Rx = S$ assembles the boundary conditions and contact conditions (4.9) as well as the equalities $d_7 = d_6$ and (4.36).

4.5 Computational Environment

We present briefly here below the computational environment in which we solve the problem.

4.5.1 Organization of the Program

The solver MOSEK is called from the MATLAB interface. The program developed with MATLAB is organized into four parts:

1. The first part reads the inputs from a file written by the finite element software CESAR-LCPC; CESAR-LCPC is used to create the mesh for our sample and write a .data file of this mesh; the .data file contains the coordinates of the nodes and proposes a numbering of the nodes; the nodes where there is a boundary condition are also emphasized.
2. The second part writes the objective function, the linear constraints and the conic constraints with the formalism of MOSEK.
3. The third part calls the solver MOSEK
4. The fourth and last part organizes the outputs given by MOSEK and displays graphically the results.

4.5.2 Presentation of the Results by MOSEK

During MOSEK optimization, several information are shown on the screen (Fig. 4-3 and Fig. 4-4):

- MOSEK displays the method it uses to solve the minimization problem. As expected, it uses the 'Interior Point Method'.
- MOSEK uses both a primal and dual problem formulation, which converge toward the same limit. The problem status is given as 'primal-dual feasible' (see Appendix B).
- The solution status is 'optimal' or 'near-optimal' according to the speed of the convergence of the iteration process.
- At the end of MOSEK routine, the computational time is given.
- Last, our MATLAB routine displays the final value of the hardness-to-cohesion ratio.

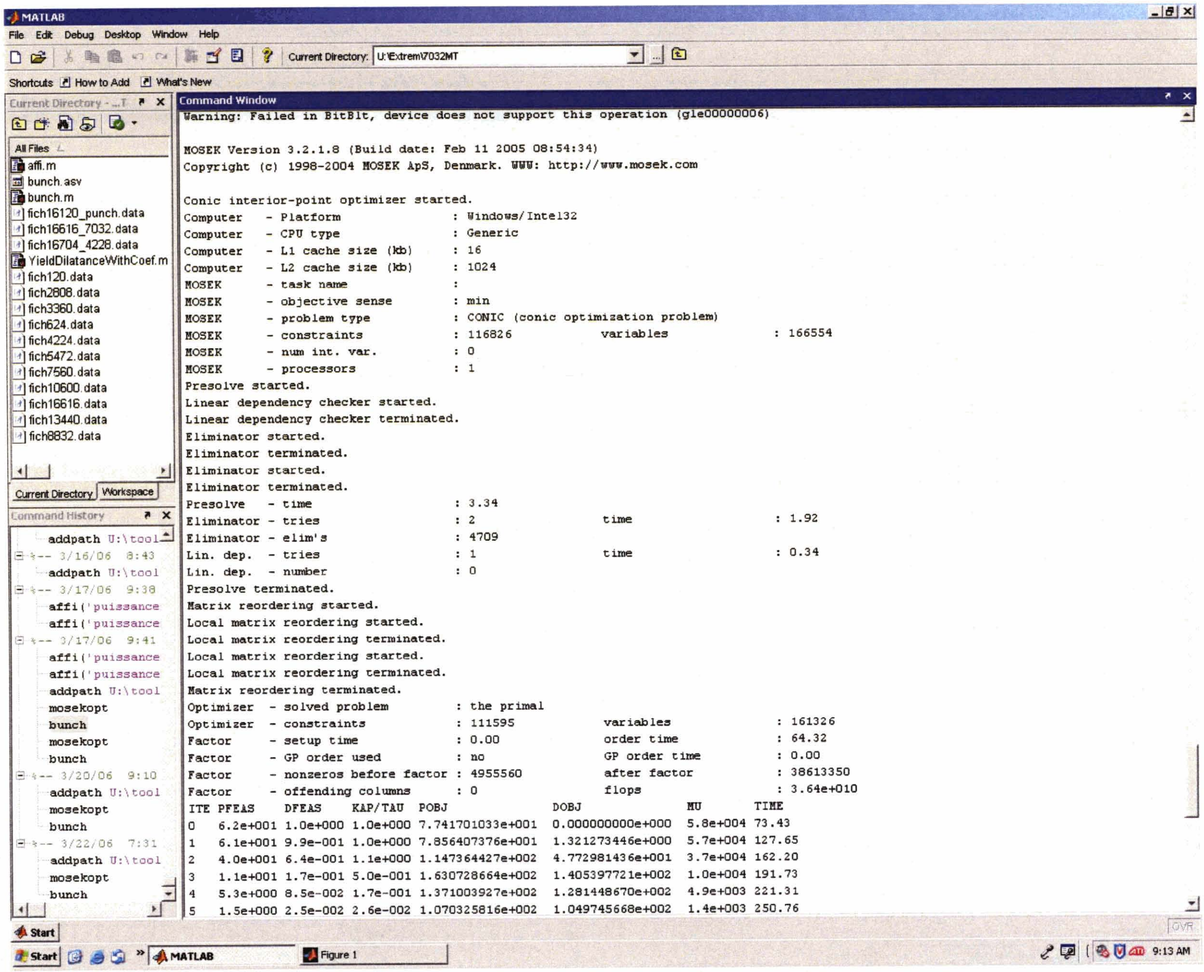

```
addpath U:\tool
%-- 3/16/06  8:43
addpath U:\tool
%-- 3/17/06  9:38
affi('puissance
affi('puissance
%-- 3/17/06  9:41
affi('puissance
affi('puissance
addpath U:\tool
mosekopt
bunch
mosekopt
bunch
%-- 3/20/06  9:10
addpath U:\tool
mosekopt
bunch
%-- 3/22/06  7:31
addpath U:\tool
mosekopt
bunch
```

```
Warning: Failed in BitBlt, device does not support this operation (gle00000006)

MOSEK Version 3.2.1.8 (Build date: Feb 11 2005 08:54:34)
Copyright (c) 1998-2004 MOSEK ApS, Denmark. WWW: http://www.mosek.com

Conic interior-point optimizer started.
Computer    - Platform              : Windows/Intel32
Computer    - CPU type              : Generic
Computer    - L1 cache size (kb)    : 16
Computer    - L2 cache size (kb)    : 1024
MOSEK       - task name             :
MOSEK       - objective sense       : min
MOSEK       - problem type          : CONIC (conic optimization problem)
MOSEK       - constraints           : 116826          variables             : 166554
MOSEK       - num int. var.         : 0
MOSEK       - processors            : 1
Presolve started.
Linear dependency checker started.
Linear dependency checker terminated.
Eliminator started.
Eliminator terminated.
Eliminator started.
Eliminator terminated.
Presolve    - time                  : 3.34
Eliminator - tries                  : 2               time                  : 1.92
Eliminator - elim's                 : 4709
Lin. dep.   - tries                 : 1               time                  : 0.34
Lin. dep.   - number                : 0
Presolve terminated.
Matrix reordering started.
Local matrix reordering started.
Local matrix reordering terminated.
Local matrix reordering started.
Local matrix reordering terminated.
Matrix reordering terminated.
Optimizer  - solved problem         : the primal
Optimizer  - constraints            : 111595          variables             : 161326
Factor     - setup time             : 0.00            order time            : 64.32
Factor     - GP order used          : no              GP order time         : 0.00
Factor     - nonzeros before factor : 4955560         after factor          : 38613350
Factor     - offending columns      : 0               flops                 : 3.64e+010
ITE PFEAS   DFEAS   KAP/TAU POBJ             DOBJ             MU      TIME
0   6.2e+001 1.0e+000 1.0e+000 7.741701033e+001 0.000000000e+000 5.8e+004 73.43
1   6.1e+001 9.9e-001 1.0e+000 7.856407376e+001 1.321273446e+000 5.7e+004 127.65
2   4.0e+001 6.4e-001 1.1e+000 1.147364427e+002 4.772981436e+001 3.7e+004 162.20
3   1.1e+001 1.7e-001 5.0e-001 1.630728664e+002 1.405397721e+002 1.0e+004 191.73
4   5.3e+000 8.5e-002 1.7e-001 1.371003927e+002 1.281448670e+002 4.9e+003 221.31
5   1.5e+000 2.5e-002 2.6e-002 1.070325816e+002 1.049745668e+002 1.4e+003 250.76
```

Figure 4-3: MOSEK screen (1)

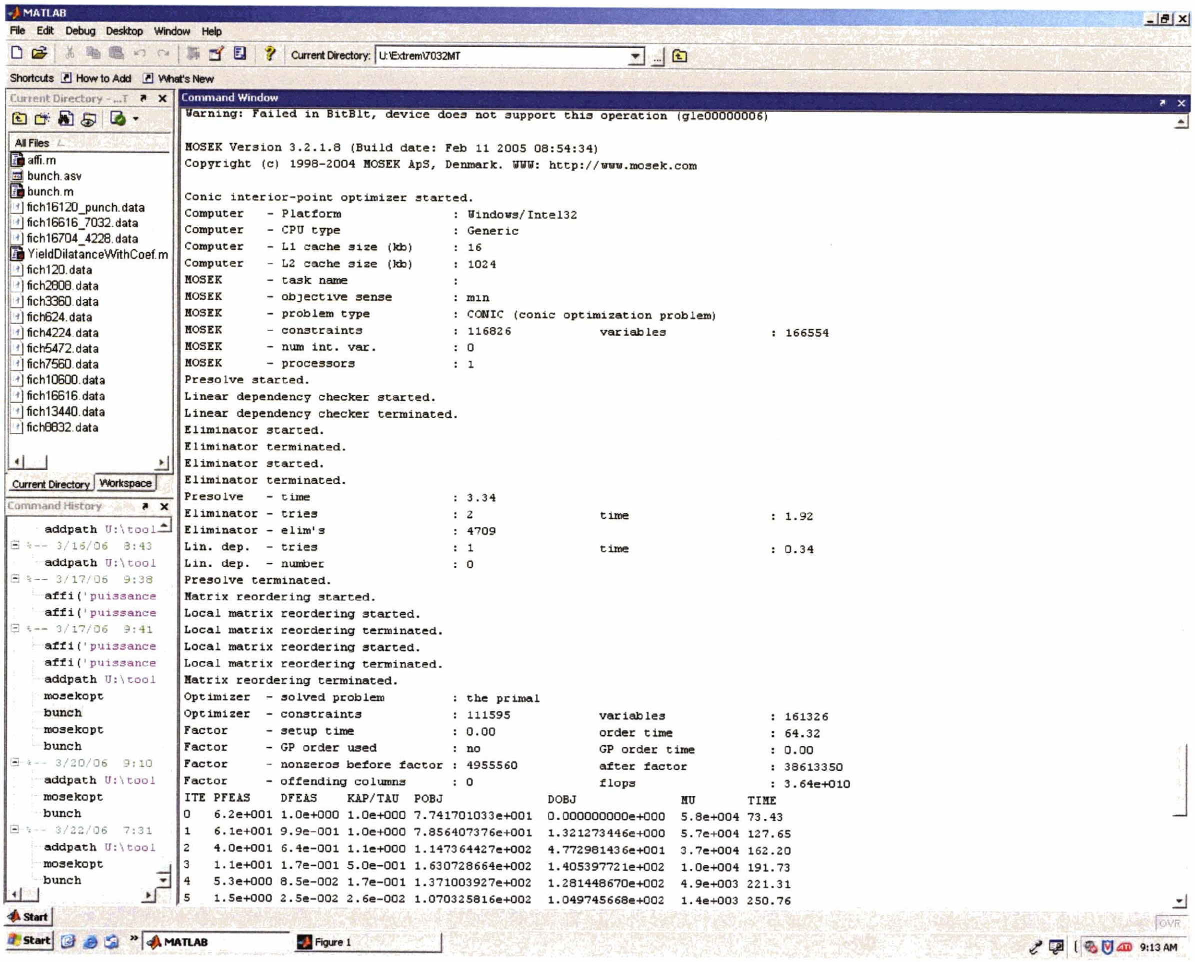

```
    addpath U:\tool
%-- 3/16/06  8:43
    addpath U:\tool
%-- 3/17/06  9:38
    affi('puissance
    affi('puissance
%-- 3/17/06  9:41
    affi('puissance
    affi('puissance
    addpath U:\tool
    mosekopt
    bunch
    mosekopt
    bunch
%-- 3/20/06  9:10
    addpath U:\tool
    mosekopt
    bunch
%-- 3/22/06  7:31
    addpath U:\tool
    mosekopt
    bunch
```

```
Warning: Failed in BitBlt, device does not support this operation (gle00000006)

MOSEK Version 3.2.1.8 (Build date: Feb 11 2005 08:54:34)
Copyright (c) 1998-2004 MOSEK ApS, Denmark. WWW: http://www.mosek.com

Conic interior-point optimizer started.
Computer    - Platform                : Windows/Intel32
Computer    - CPU type                : Generic
Computer    - L1 cache size (kb)      : 16
Computer    - L2 cache size (kb)      : 1024
MOSEK       - task name               :
MOSEK       - objective sense         : min
MOSEK       - problem type            : CONIC (conic optimization problem)
MOSEK       - constraints             : 116826          variables             : 166554
MOSEK       - num int. var.           : 0
MOSEK       - processors              : 1
Presolve started.
Linear dependency checker started.
Linear dependency checker terminated.
Eliminator started.
Eliminator terminated.
Eliminator started.
Eliminator terminated.
Presolve    - time                    : 3.34
Eliminator  - tries                   : 2               time                  : 1.92
Eliminator  - elim's                  : 4709
Lin. dep.   - tries                   : 1               time                  : 0.34
Lin. dep.   - number                  : 0
Presolve terminated.
Matrix reordering started.
Local matrix reordering started.
Local matrix reordering terminated.
Local matrix reordering started.
Local matrix reordering terminated.
Matrix reordering terminated.
Optimizer   - solved problem          : the primal
Optimizer   - constraints             : 111595          variables             : 161326
Factor      - setup time              : 0.00            order time            : 64.32
Factor      - GP order used           : no              GP order time         : 0.00
Factor      - nonzeros before factor  : 4955560         after factor          : 38613350
Factor      - offending columns       : 0               flops                 : 3.64e+010
ITE PFEAS    DFEAS    KAP/TAU  POBJ                DOBJ                MU      TIME
0   6.2e+001 1.0e+000 1.0e+000 7.741701033e+001    0.000000000e+000    5.8e+004 73.43
1   6.1e+001 9.9e-001 1.0e+000 7.856407376e+001    1.321273446e+000    5.7e+004 127.65
2   4.0e+001 6.4e-001 1.1e+000 1.147364427e+002    4.772981436e+001    3.7e+004 162.20
3   1.1e+001 1.7e-001 5.0e-001 1.630728664e+002    1.405397721e+002    1.0e+004 191.73
4   5.3e+000 8.5e-002 1.7e-001 1.371003927e+002    1.281448670e+002    4.9e+003 221.31
5   1.5e+000 2.5e-002 2.6e-002 1.070325816e+002    1.049745668e+002    1.4e+003 250.76
```

Figure 4-4: MOSEK screen (2)

4.6 Chapter Summary

We now have a working model in place to perform the multi-scale indentation analysis of the hardness-to-cohesion ratio of cohesive-frictional porous materials. In this Chapter, we developed an original computational implementation of the upper bound theorem. Our approach is based on the identification of our problem as a Second-Order Conic optimization problem. To our knowledge, this is the first time that the upper bound approach, when used with an elliptical strength criterion, is recognized as a SOCO. This identification opens the way for solving the problem by most advanced solver techniques, such as MOSEK. The originality of our approach lies in the combination of finite element discretization and advanced optimization techniques, which is readily implemented in standard tools of computational mechanics, such as MATLAB. The validation of this approach is shown in the next two Chapters, before we apply it to shale indentation analysis in Chapter 7.

Part III

Upper Bound Solutions

Chapter 5

Verification and Validation

This third part of the thesis presents the upper bound solutions obtained with the optimization algorithm developed in Chapter 4. This Chapter is dedicated to a rigorous verification and validation of the upper bound solution procedure. Given the discretized nature of the problem with finite elements we start with a sensitivity analysis of the results with regard to meshing effects. In particular, we study the effect of the boundary of the modeled domain on the hardness-to-cohesion ratio. We then present a validation of the upper bound solution for flat indentation for which we developed a lower bound solution in Chapter 3. Both verification and validation provide a sound basis for a parameter study of the multi-scale strength model in Chapter 6.

5.1 Discretization Verification

In contrast to theoretical indentation analysis which is based on the infinite half-space model of a continuum, the implementation of the upper bound of our model involves a finite sample domain Ω'(see Fig. 4-1). This introduces two additional finite length scales into the axi-symmetric analysis: sample height z_M and sample radius r_M (see Fig. 4-2). A third additional length scale is introduced by the finite characteristic size ℓ of the elements employed in the finite element (FE) mesh of Ω'. We recall that the use of linear interpolation functions leads to a constant strain rate per element, and thus to a constant value of the dissipation function per element (see Section 4.2.4). Eliminating those discretization effects is of critical importance in several regards. In particular, the additional three length scales (h, r_M, ℓ) may jeopardize the classical self-similarity properties of the indentation test as stated in Section 2.1.2. As a consequence, the hardness would depend not only on the strength properties of the indented material, but as well on mesh-size effects and size of the modeled domain. Hence, instead of (2.34):

$$\frac{H}{c^s} = \mathcal{F}\left(\alpha, \varphi, \eta_0, \theta, \frac{z_M}{h}, \frac{r_M}{a}, \frac{z_M}{\ell}\right) \tag{5.1}$$

where:

- The ratios z_M/h and r_M/a represent respectively the sample height-to-indentation depth ratio and the radial sample extension-to-contact radius ($a = h \tan\theta$ in conical indentation). Both reflect a possible effect of the zero-velocity boundary conditions on the indentation response. In the continuum half-space model, $z_M/h \to \infty$ and $r_M/a \to \infty$. Eliminating those effects for finite values of z_M/h and r_M/a amounts to eliminating artificial boundary condition effects.

- The ratio r_M/ℓ, which is the radial extension of the sample over the characteristic size of a mesh element, reflects the mesh sensitivity of the implementation. In fact, for $r_M = z_M$, $r_M/\ell \sim \sqrt{N}$ where N is the number of elements. In the continuum model $r_M/\ell \to \infty$. Eliminating this discretization effect for finite values of r_M/ℓ is critical for the choice of the appropriate element size.

The ultimate aim of studying those invariants is to determine an optimized mesh whose response in indentation analysis approaches the best the half-space model. By 'optimized' we mean a mesh which eliminates the discretization length scale effects, while remaining computationally efficient for a massive employment in a parameter study of our model.

5.1.1 Regular vs. Irregular Mesh

To start our investigation, we have a look on mesh effects induced by regular vs. irregular FE meshes. The elements we use are triangular elements. Meshes are generated with the pre-

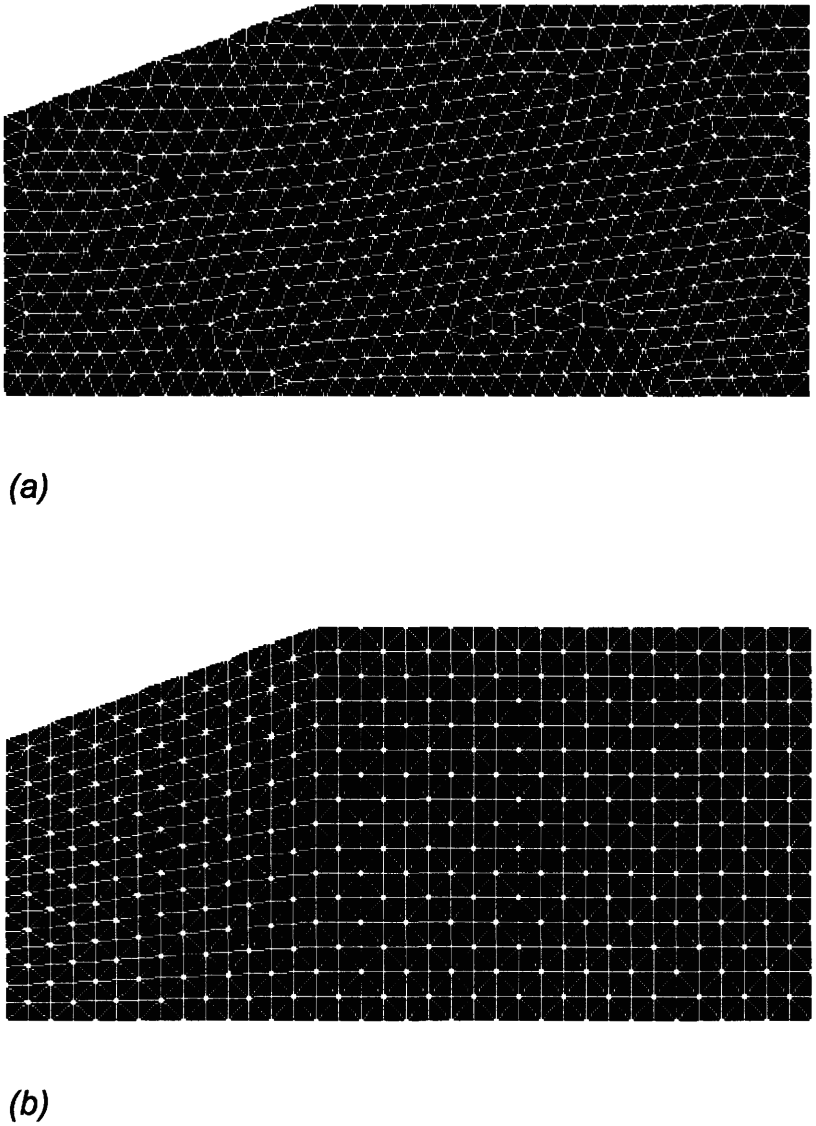

Figure 5-1: 2 mesh configurations: (a) direct triangulation, (b) sub-triangulation: a rectangle is divided into 8 regular triangles.

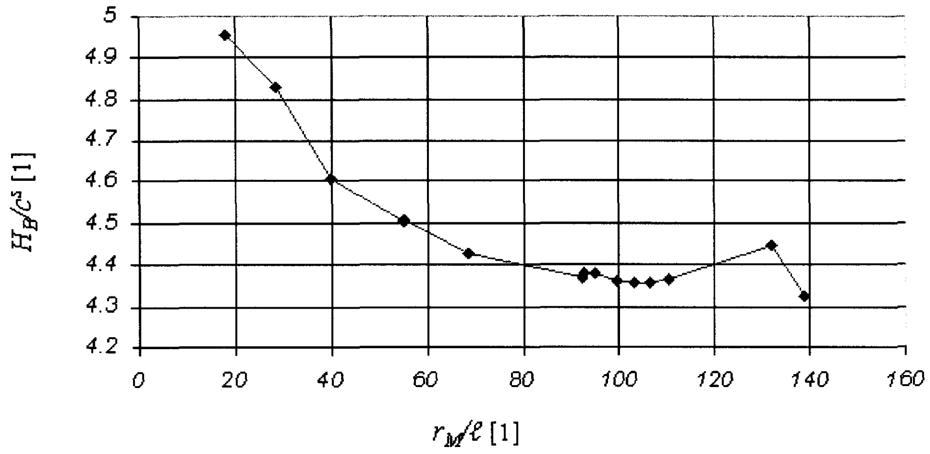

Figure 5-2: Mesh effects due to irregular mesh generated by direct triangulation: Hardness-to-cohesion ratio vs. mesh-size number r_M/ℓ. (Simulation results for $\theta = 70.32°$, $\alpha = 0, \varphi = 0.033, \eta_0 = 0$).

processor of CESAR-LCPC, which offers among other options two mesh operations (see Figure 5-1):

1. Direct triangulation: The domain Ω' is discretized by triangular elements of a characteristic length ℓ, without imposing any fixed points that restrict the location of individual nodes (Fig. 5-1(a)). This mesh generation procedure depends on the triangulation method used in the software, for instance Delaunay triangulation[1], and yields an irregular mesh. The particular triangulation method may induce another length scale in the analysis, characterizing the regularity of the mesh. For instance, a Delaunay triangulation enforces that no three points are on the same line and no four are on the same circle, for a two dimensional set of points. As the number of points increases, the effect becomes negligible; but along this way, there are effects of the non-smoothness of the mesh on the hardness-to-cohesion ratio. This is shown in Figure 5-2, in form of a plot of H/c^s vs.

---

[1] In mathematics, and computational geometry, the Delaunay triangulation or Delone triangularization for a set P of points in the plane is the triangulation DT(P) of P such that no point in P is inside the circumcircle of any triangle in DT(P). Delaunay triangulations maximize the minimum angle of all the angles of the triangles in the triangulation; they tend to avoid "sliver" triangles. (from http://en.wikipedia.org/wiki/Delaunay_triangulation)

r_M/ℓ. The irregular mesh influences the discretized velocity field, which in turn prevents a smooth evolution of the velocity when the mesh is refined.

2. Sub-Triangulation: The domain Ω' is first discretized by quadrilateral (square) elements.[2] The quadrilateral elements are then subdivided into eight triangular elements. The first step generates a regular distribution of nodes in Ω': nodes are now nicely organized in a regular woven-type pattern (Fig. 5-1(b)). As a consequence, the velocity field is a lot less influenced by the distribution of the nodes. A careful examination of the velocity fields shows a slight disturbance around the vertical line demarcating the limit between the free surface region and the region below the indenter. We can hardly avoid this disturbance in the velocity field, since this vertical line separates anyway two zones with very different boundary conditions. On the other hand, this disturbance seems not to affect the overall hardness-to-cohesion response. Indeed, the nice and smooth curves that are presented throughout this chapter are based on the regular mesh obtained by sub-triangulation.

5.1.2 Eliminating Boundary Effects

The aim of this Section is to determine the minimum extension of the meshed domain for which the effects of the zero-boundary conditions prescribed along $\partial\Omega'$ become negligible. In this case, the discrete solutions should be close to the infinite half-space model underlying indentation analysis. Given the large variety of possible model parameters that may influence the results, we need to define a reference 'worst-case scenario'. This 'worst' representative case corresponds to the one which produces the widest distribution of the velocity field in Ω'. From a visual inspection of a large array of velocity field results, we choose the case where $\theta = 70.32°$ (Berkovich indentation), $\alpha = 0$, $\phi = 0.000001$, which is very close to the pure Von-Mises case.

---

[2] In the pre-processor of CESAR-LCPC, the quadrilateral elements are 8-noded solid elements, which are divided in eight 6-noded triangles. In our computational implementation we reduce the 6-noded elements to 3-noded elements by means of a specially designed interface program.

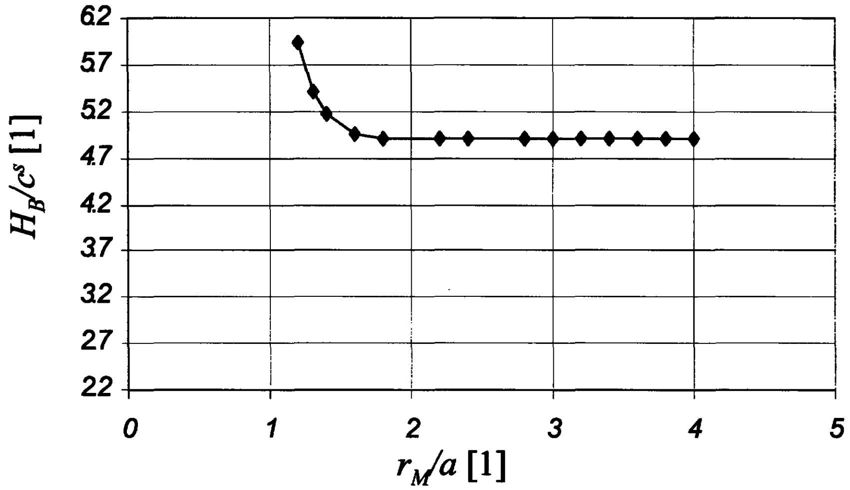

Figure 5-3: Study of boundary effects: Hardness-to-cohesion ratio vs. radial extension r_M/a, at constant values of z_M/h and r_M/ℓ. (Simulation results for $\theta = 70.32°$, $\alpha = 0, \varphi = 0.000001, \eta_0 = 0$).

Radial Sample Extension r_M/a

Figure 5-3 displays the hardness-to-cohesion ratio as a function of the radial extension parameter r_M/a (r_M is the radial mesh length, a is the projected contact radius). For this study, the height z_M/h of the sample and the mesh size number r_M/ℓ are kept constant. The results call for the following comments:

- For $r_M/a < 1.2$, the problem is not primal-dual[3]. This means that there are too many constraints on the sample and there is no primal-dual feasible solution. In this case, the velocity fields appear to be unrealistic (see Fig. 5-4), leading to unrealistic high H/c^s values (for instance, $H/c^s\,(r_M/a = 1.1) = 407.4$!).
- For $1.2 < r_M/a < 1.8$, the influence of the mesh extension is important, and thus the effects of the lateral zero-velocity boundary conditions on the indentation response. This can be explained from a visual inspection of the velocity fields in Figure 5-5: As r_M/a

---

[3] The reader will find a definition and importance of a primal-dual problem in Appendix B dealing with some elements of optimization theory.

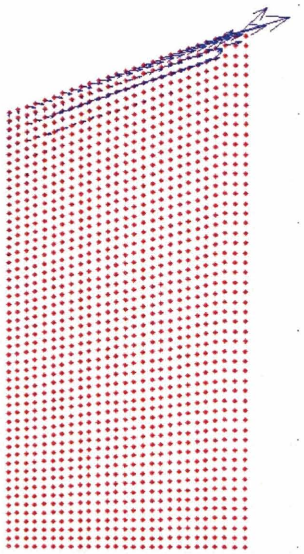

Figure 5-4: Velocity field for $r_M/a = 1.1$. The solution is not primal-dual feasible. (Simulation result for $\theta = 70.32°$, $\alpha = 0, \varphi = 0.000001, \eta_0 = 0$).

increases from 1.2 (Fig.5-5 (a)) to 1.8 (Fig.5-5 (b)), the velocity fields emerge freely to the surface, instead of being generated by the enforced zero-velocity boundary condition at r_M.

Figure 5-3 shows that the H/c^s stabilizes for $r_M/a > 1.8$. However, a closer look on the velocity field reveals that the velocity field for $r_M/a = 1.8$ is still influenced by the lateral boundary conditions, in particular in comparison with a larger extension $r_M/a = 4$ (Fig.5-5 (c)) for which the boundary effect becomes negligible. This does not change the overall H/c^s ratio, since the velocity field is compressed horizontally and lengthened vertically and since the perturbed vectors are very small compared to the average vector. As a consequence both effects compensate each other, and the internal dissipation still equates to $H/c^s = 4.88 - 4.90$.

Our final choice is $r_M/a = 2.6$ (Fig.5-5 (d)), for which the effects of lateral boundary conditions can be considered as negligible on the velocity field and the H/c^s ratio.

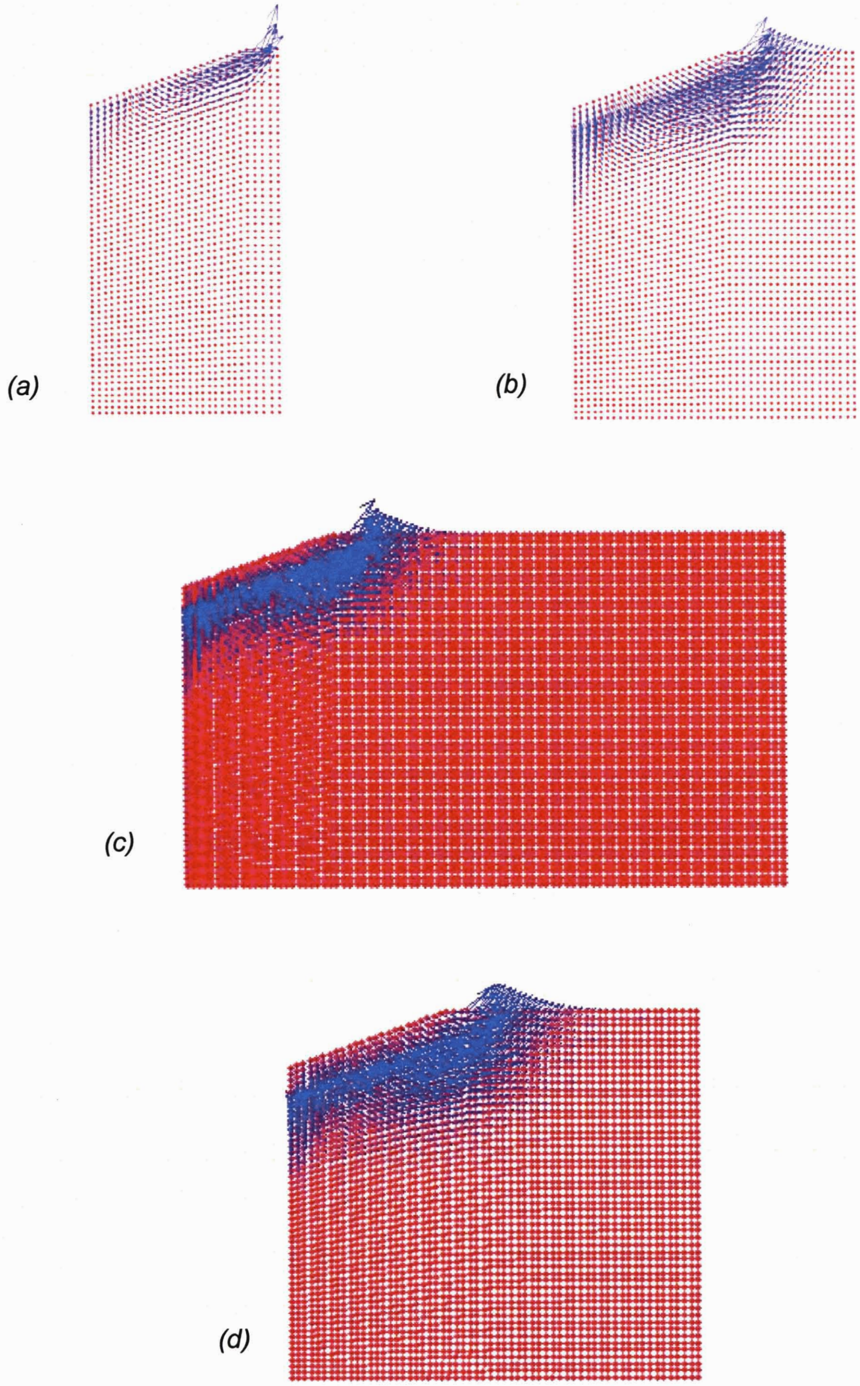

Figure 5-5: Velocity fields for (a) $r_M/a = 1.2$, (b) $r_M/a = 1.8$, (c) $r_M/a = 4.0$ and (a) $r_M/a = 2.6$. (Simulation results for $\theta = 70.32^\circ$, $\alpha = 0, \varphi = 0.000001, \eta_0 = 0$).

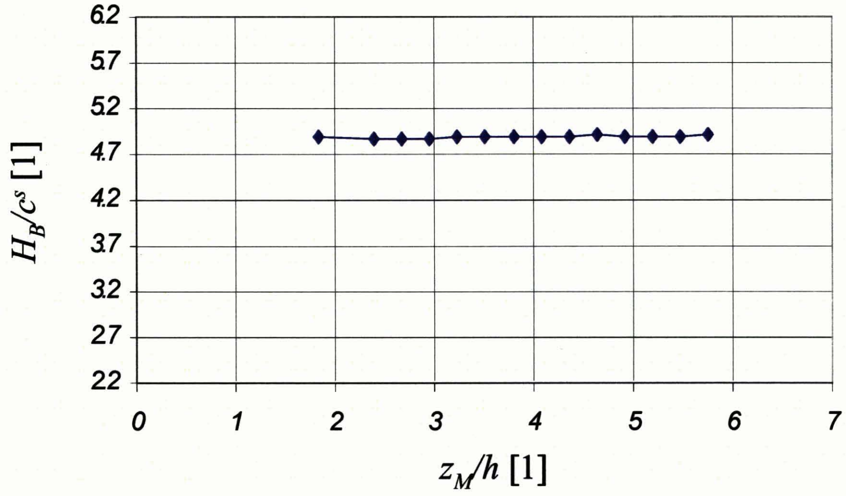

Figure 5-6: Study of boundary effects: Hardness-to-cohesion ratio vs. vertical mesh extension z_M/h, at constant values of r_M/a and r_M/ℓ. (Simulation results for $\theta = 70.32°$, $\alpha = 0, \varphi = 0.000001, \eta_0 = 0$).

Sample Height z_M/h

A similar study is carried out to determine the sample height z_M/h, while keeping r_M/a and r_M/ℓ constant. The results are displayed in Figure 5-6:

- For $z_M/h < 1.8$, there are too many constraints on the sample and no primal-dual solution is found.

- For $z_M/h > 1.8$ all primal-dual solutions converge to the same value, $H/c^s = 4.88 - 4.90$. On the other hand, the velocity fields displayed in Figure 5-7 tell a different story: For $z_M/h = 1.8$ (Fig.5-7 (a)) the velocity field appears to be strongly disturbed close to the lower boundary, while this effect is negligible for $z_M/h = 5.75$ (Fig.5-7 (b)). The reason for which both samples yield the same H/c^s ratio may be explained as before: the velocity field is lengthened horizontally and compressed vertically and since the disturbed vectors are very small compared to the average vector, both effects compensate and the internal power still equates to $H/c^s = 4.88 - 4.90$.

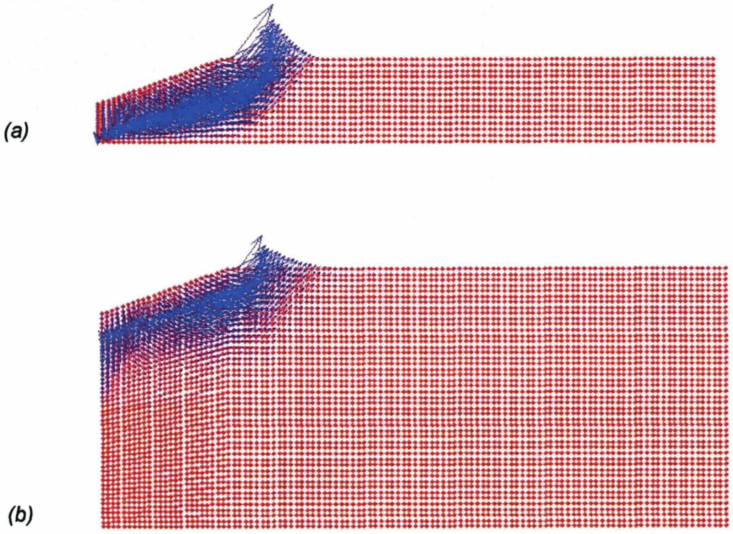

Figure 5-7: Velocity fields for (a) $z_M/h = 1.8$, (b) $z_M/h = 5.75$. (Simulation results for $\theta = 70.32°$, $\alpha = 0, \varphi = 0.000001, \eta_0 = 0$).

Based on this study, we choose a value of $z_M/h = 3.5$, which ensures that the vertical boundary effects do not affect the (upper bound) indentation hardness response.

5.1.3 Upper Bound Convergence Study

The last effect we study is the mesh-size effect captured by the mesh size number r_M/ℓ in the dimensionless relation (5.1). In these simulations, $r_M/a = 2.6$ and $z_M/h = 3.5$, which eliminates possible boundary effects. Therefore, studying the effect of the mesh size number r_M/ℓ provides a means to verify the convergence behavior of our upper bound computational implementation. Figure 5-8 shows a consistent convergence of the upper bound solution: as the mesh size number increases the hardness-to-cohesion ratio converges towards a constant value, and this for finite values of the mesh size number. We choose $r_M/\ell = 130$ which corresponds to a total number of triangle elements of $N = 16,000$. This high number of elements comes at a price, as figure 5-9 shows: the computational time increases rapidly with the number of elements. Recalling that r_M/ℓ is roughly $\sqrt{N}$, figure 5-9 allows us to conclude that the computational time increases almost linearly with r_M/ℓ.

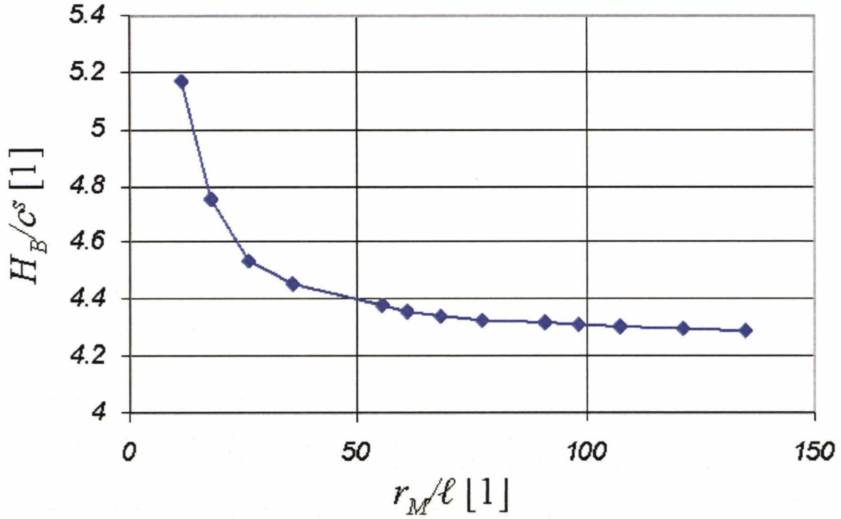

Figure 5-8: Convergence study of mesh size effects: Hardness-to-cohesion ratio vs. mesh-size number r_M/ℓ, at constant values of $r_M/a = 2.6$ and $z_M/\ell = 3.5$. (Simulation results for $\theta = 70.32°$, $\alpha = 0, \varphi = 0.033, \eta_0 = 0$).

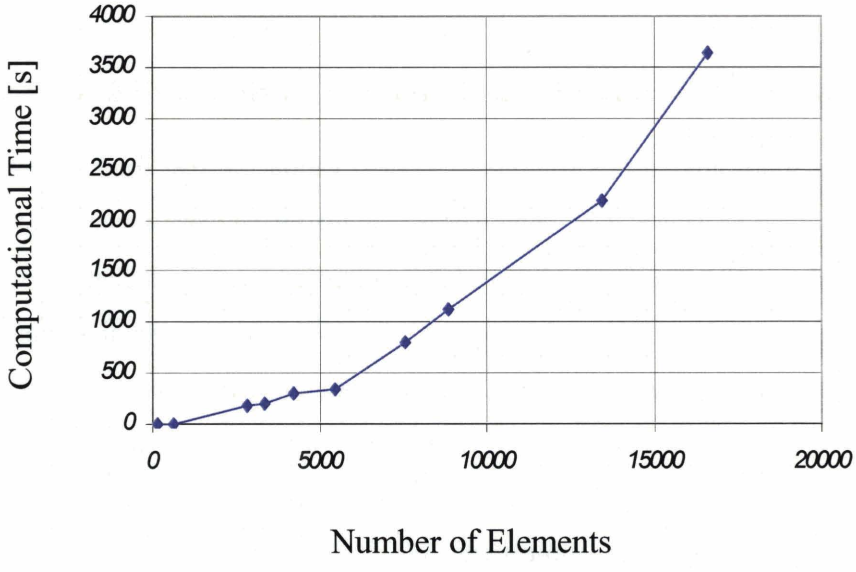

Figure 5-9: Computational time vs. number of elements. (Simulation results for $\theta = 70.32°$, $\alpha = 0, \varphi = 0.033, \eta_0 = 0$).

5.2 Validation

We now have a working computational model in hand, which validates the computational implementation of the upper bound solution. This allows us to return to the true focus of our study, which is (2.34):

$$\frac{H}{c^s} = \mathcal{F}(\alpha, \varphi, \eta_0, \theta) \tag{5.2}$$

This section is devoted to a quantitative validation of the upper bound solution. The upper bound finite element simulation is validated with the following data:

- The Von-Mises pure solid case, for which Cheng and Cheng [17] reported $H/Y \simeq 2.8$ from comprehensive finite element elastoplastic analysis on a conical indentation with a semi-apex angle of $\theta = 68°$. We will study this limit case by letting $\alpha = 0$ and $\varphi = 0$ in our model, while varying the semi-apex angle θ.
- The lower bound solution for flat indentation developed in Sections 3.3.2 and 3.3.3.

As we will see, these two limit cases provide a means to quantitatively assess the predictive capabilities of our upper bound solution.

5.2.1 Validation Set #1: Limit Case of a (Pure) Von-Mises Solid

The Von-Mises solid-only-case is the most classical validation test for hardness-strength properties relations (see Section 2.2.2). The earliest quantitative work for such materials is due to Tabor [72]. Tabor's slip-line field solution for indentation in a rigid-plastic solids by a frictionless rigid wedge provides $H/Y = 3$, where $Y = \sqrt{3}c^s$ is the uniaxial strength and c^s is the Von-Mises cohesion. Cheng and Cheng [17] by means of comprehensive finite element elastoplastic contact simulations showed that $H/Y \simeq 2.8$ for materials for which $Y/E \rightarrow 0$, when Y is taken as the uniaxial yield stress at 10% of strain. This value is considered today as a rule-of-thumb in the indentation literature. We should note, however, that Cheng and Cheng obtained this result by simulating the comical indentation having a semi-apex angle $\theta = 68°$. To our knowledge, this apex angle is not representative of any of the typical indenter shapes used today (see Section 2.1.2, Table 2.1): the equivalent cone angle of a Berkovich or Vickers indenter is $\theta = 70.32^\circ$ and $\theta = 42.28^\circ$ for the Cube Corner.

We want to validate our approach for this limit case of a Von-Mises solid. This is obtained by letting $\alpha = 0$ and $\varphi = 0$ in our model:

$$\frac{H}{Y} = \frac{1}{\sqrt{3}}\mathcal{F}\left(\alpha = 0, \varphi = 0, \eta_0, \theta\right) \tag{5.3}$$

For purpose of comparison with Cheng and Cheng's value, we assume that the uniaxial strength Y is representative of the yield stress at 10%. On the other hand, we do not fix the cone-angle, but determine H^+/Y for three indenter shapes: cube corner, 68°-Cone, Berkovich (or Vickers) and flat indenter. The values we obtain with the upper bound approach are presented in Table 5.1, and are plotted in Figure 5-10 as a function of the half-cone angle. We readily note that our simulation result for the 68°-Cone are in excellent agreement with Cheng and Cheng's result obtained by complete elasto-plastic finite element simulations. Furthermore, the results also show that there is a slight (yet visible) dependence of the hardness-to-strength ratio on the cone angle: the highest hardness is obtained for the flat punch and the lowest hardness for the cube corner[4]. Finally, Table 5.1 lists the values for both the Mori-Tanaka scheme and the Self-Consistent Scheme. As expected, for a pure solid phase, both schemes provide the same response.

Finally, the value we obtain with the upper bound solution for the flat punch, $H^+/Y = 3.1$ is well above the lower bound prediction $H^-/Y = 2$ developed in Section 3.3.2 (Eq. (3.75)).

---

[4] For reference: The Berkovich-to-Cube Corner hardness ratio for the Von-Mises case is:

$$\frac{H_B}{H_{CC}} = 1.118$$

The dual indentation technique of Ganneau et al. [37] developed for cohesive-frictional solids (of the Mohr-Coulomb type) would predict for this ratio (see Eq. (2.21) and Fig. 2-5) a friction angle of roughly $\phi = 10^\circ$. The accuracy of this method, therefore, appears to be limited to higher friction angles, as the same ratio may simply correspond to the effect of the cone angle on the hardness of a pure cohesive solid of the Von-Mises type.

	θ	H^+/Y (MT)	H^+/Y (SCS)
Cube Corner	42.28°	2.5292	2.5274
68°-Cone	68°	2.7956	2.7941
Berkovich	70.32°	2.8275	2.8263
Flat punch	90°	3.1003	3.0957

Table 5.1: Hardness-to-Yield Strength values obtained with the upper bound solution for a Von Mises solid material for different indenters. (MT = Mori-Tanaka, SCS = Polycrystal)

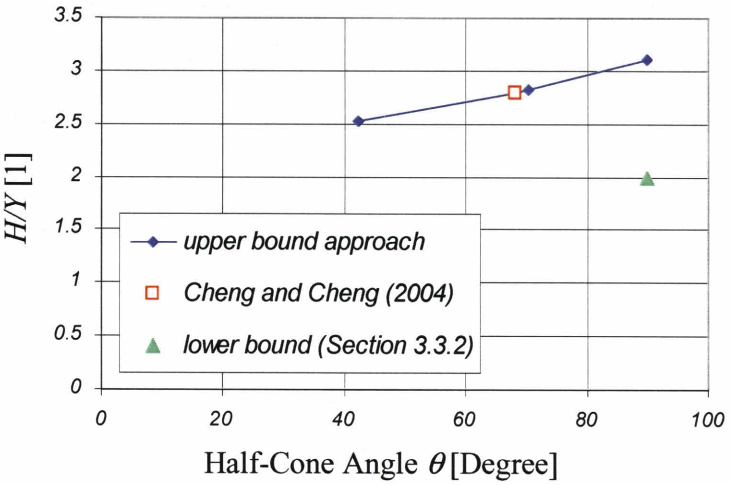

Figure 5-10: Effect of the half-cone angle θ on the hardness-to-strength ratio H/Y of a Von-Mises solid. The figure also displays the results of Cheng and Cheng obtained from comprehensive elastoplastic contact finite element simulations.

5.2.2 Validation Set #2: Comparison with Flat Punch Lower Bound Solution

Given the strong duality of the two approaches (see Appendix A.1), the true lipness test for any yield design approach is the comparison of the lower and the upper bound solution. We have already noted that close to the pure solid state ($\varphi \rightarrow 0$), our upper bound solution comes very close to the actual solution of the problem, while our lower bound approach based on a simple piece-wise constant stress field performs rather poorly. The focus of this second validation set is a comparison of the lower and upper bound over the entire range of possible porosities, and for different pore morphologies. This will be done for flat punch indentation for which we developed a lower bound in Sections 3.3.2 and 3.3.3.

Porous Von-Mises Material

We start with the comparison for a porous Von-Mises solid, for which we compare the lower bound solutions developed in Section 3.3.2 with the upper bound solutions obtained with the computational model. In terms of the dimensionless relation (5.2), the focus is on:

$$\frac{H^-}{c^s} \leq \frac{H}{c^s} = \mathcal{F}(\alpha = 0, \varphi, \eta_0, \theta = 90^\circ) \leq \frac{H^+}{c^s} \tag{5.4}$$

Figure 5-11 displays the upper and the lower bound solutions of the hardness-to-cohesion ratio as a function of the solid packing density $\eta = 1 - \varphi$ for the two pore morphologies: the matrix-pore inclusion morphology (MT = Mori-Tanaka) and the polycrystal morphology (SCS = Self-Consistent Scheme). The figure reveals some interesting results: first, the upper bound solution at all times is a true upper bound to the lower bound. Second, not surprisingly, we find that the upper bound solution is well above the lower bound solution close to $\eta = 1$, where the latter – as we have stated before – performs poorly. This trend seems to hold for packing densities roughly above 75%. But below this value, i.e. as the porosity increases, both the upper bound and the lower bound give comparable values, and almost coincide for a large range of values. For obvious reasons, they exactly converge to the same zero-value at the percolation threshold ($\eta_0 = 0$ for Mori-Tanaka, $\eta_0 = 1/2$ for Polycrystal). In other words, for $\eta_0 \leq \eta < 3/4$,

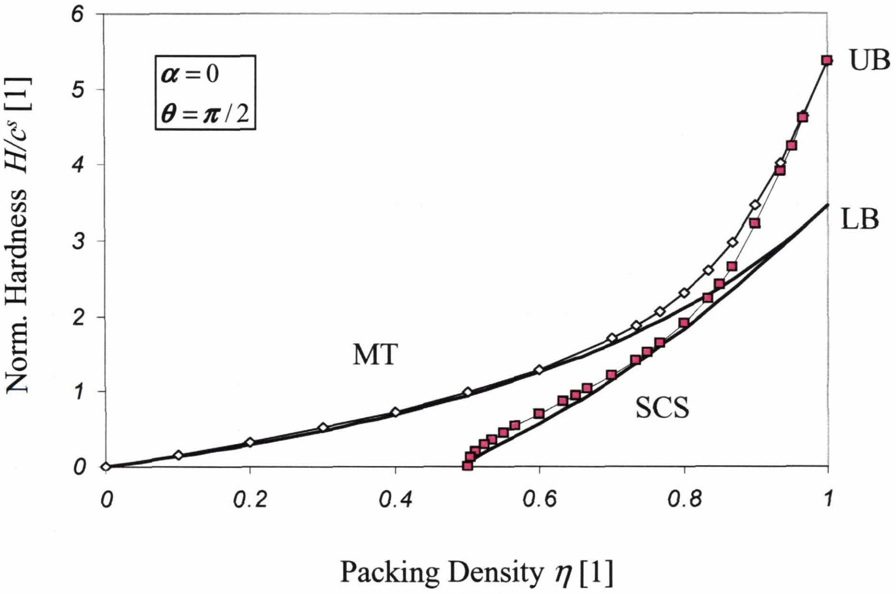

Figure 5-11: Comparison of lower bound (LB) and upper bound (UB) solutions for the flat punch for a porous Von-Mises Material (MT=Mori-Tanaka, SCS=Self-Consistent Scheme).

we almost achieve with our approach the strong duality between the lower and the upper bound approach for a porous Von-Mises material.

Porous Drucker-Prager Material

Figure 5-12 compares the lower and upper bound flat punch solution for a porous material composed of a Drucker-Prager solid and pore space; that is:

$$\frac{H^-}{c^s} \leq \frac{H}{c^s} = \mathcal{F}\left(\alpha, \varphi, \eta_0, \theta = 90^\circ\right) \leq \frac{H^+}{c^s} \tag{5.5}$$

The observation made for the Von-Mises case also apply here. In particular, we find an excellent agreement of the lower and upper bound solution for packing densities $\eta_0 \leq \eta < 3/4\eta^{\text{lim}}$, where $\eta^{\text{lim}} = \eta^{\text{lim}}\left(\alpha, \eta_0\right)$ is the limit packing density defined for the Mori-Tanaka morphology by (3.57) and for the Self-Consistent morphology by (3.58). For $3/4\eta^{\text{lim}} < \eta \leq \eta^{\text{lim}}$, lower and upper bound diverge in a very similar way as in the Von-Mises case.

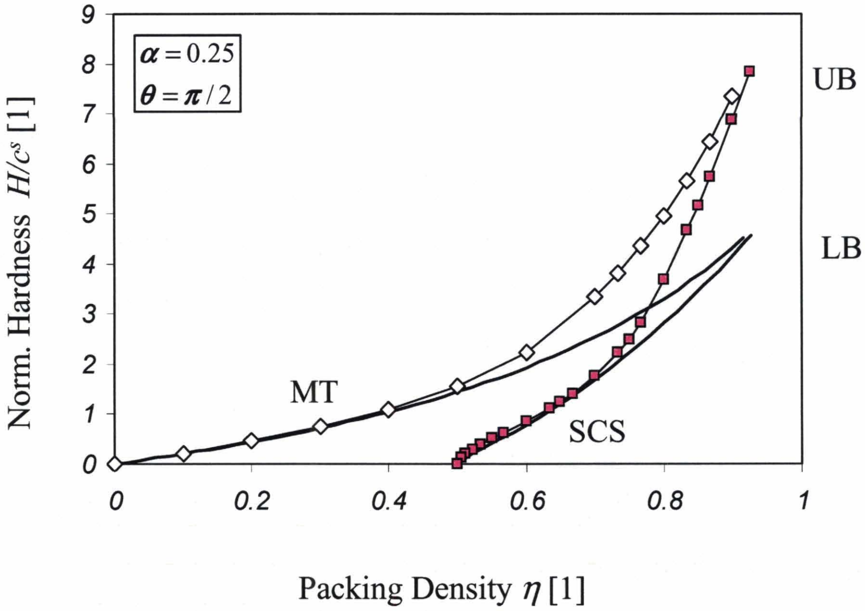

Figure 5-12: Comparison of lower bound (LB) and upper bound (UB) solutions for the flat punch for a porous Drucker-Prager Material (MT=Mori-Tanaka, SCS=Self-Consistent Scheme).

This limit behavior is exemplified in Figure 5-13 which displays the lower and upper bound of $\lim H/c^s$ for $\eta \rightarrow \eta^{\mathrm{lim}}(\alpha, \eta_0)$ for both the Mori-Tanaka and Self-Consistent Morphology.[5] The figure shows that the trend predicted by the lower bound approach (i.e. Fig. 3-8) is reproduced by the upper bound solutions, but at a somewhat higher level, as expected from an upper bound solution. The conclusions made in Section 3.3.3 apply here as well:

- The pore morphology (MT or SCS) is rather negligible for high limit packing densities $> 65\%$, corresponding to friction angles of the solid of $0 < \alpha < 0.5$ for a Mori-Tanaka solid phase and $0 < \alpha < 0.8$ for a polycrystal solid.
- The frictional behavior dominates the asymptotic behavior of porous materials for high packing densities, for which $\lim H/c^s$ is greater than $\lim H/c^s$ for a Von-Mises solid material, $\eta^{\mathrm{lim}} = 1$.
- As the material becomes increasingly porous, the effect of the solid's friction vanishes to the benefit of the specific pore morphology, which dominates the limit behavior at lower limit packing densities.

5.3 Summary of Validation

The excellent agreement with Cheng and Cheng's analysis (based on the weak form of equilibrium, i.e. finite element solution) for a pure Von-Mises solid provides strong evidence that the upper bound approach for low to zero porosities provides an excellent prediction of the actual hardness-to-strength values. Furthermore, the excellent agreement of the upper and lower flat punch solutions for packing densities $\eta_0 \leq \eta < 3/4\eta^{\mathrm{lim}}$ provides strong evidence that the solution we here propose is the actual yield design solution, in the sense of the 'strong duality' of yield design theory. This is not surprising in the light of the developments presented in Chapter 4: the consistent formulation and implementation of the upper bound has sufficient degrees of

---

[5] The attentive reader will find that the limit value of the numerical solution for $\alpha = 0$ in Figure 5-12 does not correspond to the H/c^s value for the flat punch reported in Table 5.1. In fact, the displayed upper bound values are the limit values for the Berkovich indenter $\theta = 70.32°$, which are compared with the lower bound flat punch limit values. Since $H_B/c^s < H_{90°}/c^s$, this minor detail does not change the course of our arguments.

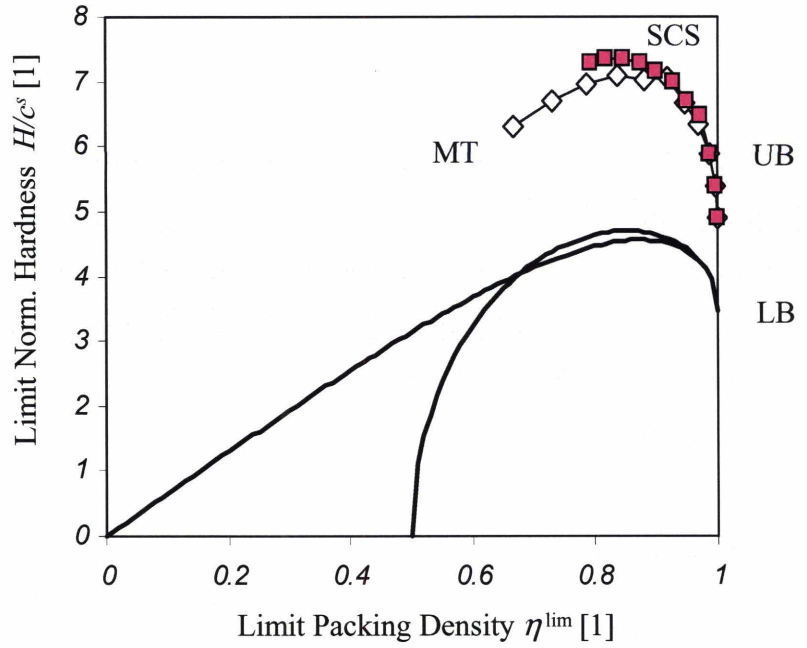

Figure 5-13: Asymptotic behavior of lower and upper bound hardness-to-cohesion ratio at the limit packing density η^{lim}. (The lower bound corresponds to the flat punch, while the upper bound solution is for Berkovich indenter).

freedoms to accurately capture the actual dissipation capacity of the material system below the indenter, for which reason the solution converges to the actual solution of the optimization problem. Hence, in all what follows we will refer exclusively to the upper bound solutions.

What is most surprising, however, is that the relatively simple lower bound based on a piecewise constant stress-field performs exceptionally well for packing densities $\eta_0 \leq \eta < 3/4\eta^{\text{lim}}$. The reason for this agreement can only be related to the elliptical strength criterion, which appears to be well adapted to capture the strength behavior below an indenter even with crude stress field approximations.

Indeed, if we evaluate the stress field corresponding to the upper bound from (3.37) we readily see that the stresses are far from piecewise constant as assumed in the lower bound approach. The stresses $\overline{\Sigma}_m = \frac{1}{3} tr\mathbf{\Sigma}/c^s$ and $\sqrt{2}\overline{\Sigma}_d = \sqrt{\mathbf{\Sigma}_d : \mathbf{\Sigma}_d}/c^s$ are displayed in Figure 5-14.

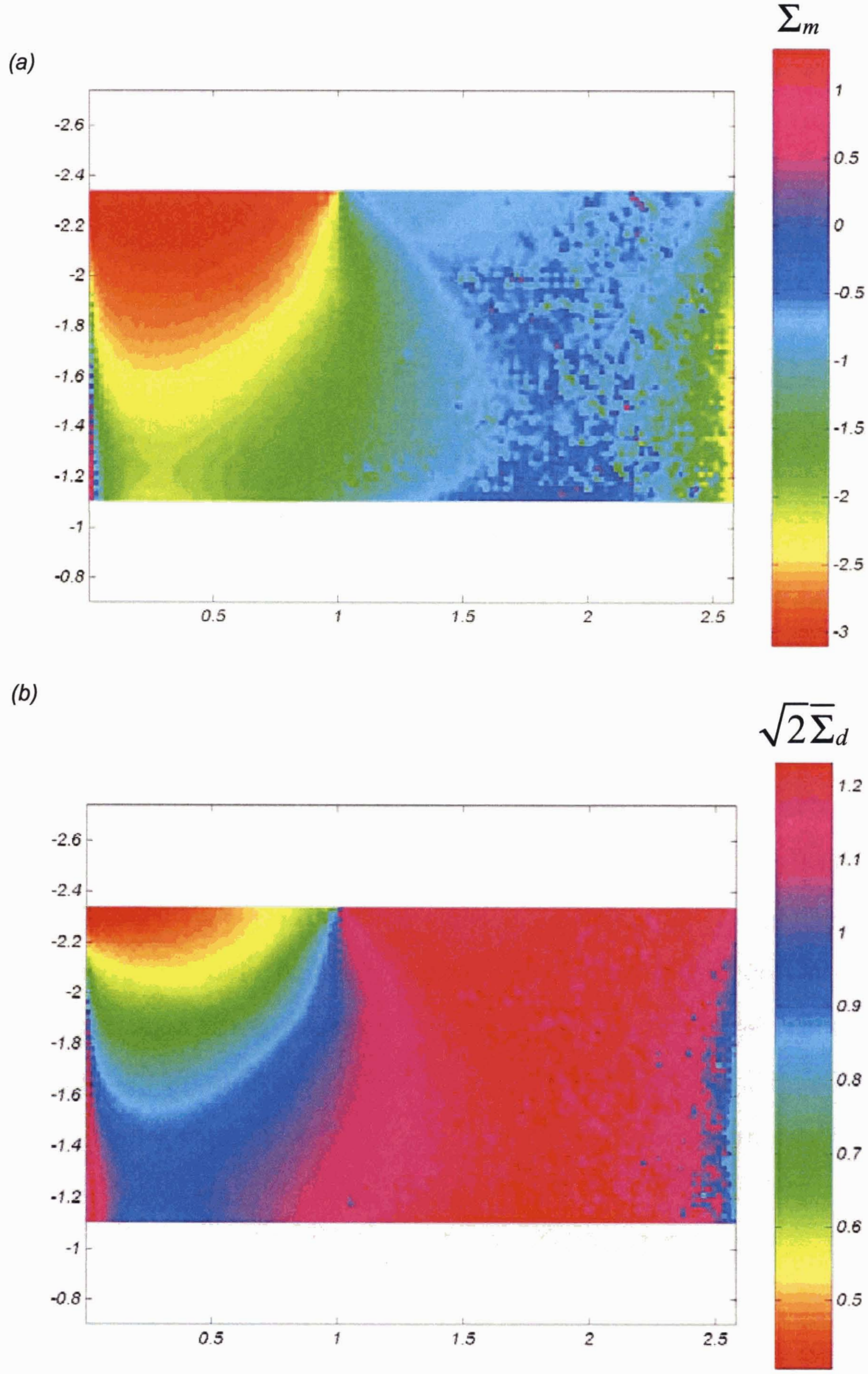

Figure 5-14: Sress Fields (a) $\overline{\Sigma}_m = \frac{1}{3} tr\mathbf{\Sigma}/c^s$ and (b) $\sqrt{2}\overline{\Sigma}_d = \sqrt{\mathbf{\Sigma}_d : \mathbf{\Sigma}_d}/c^s$ corresponding to the upper bound solution for $\alpha = 0$, $\varphi = 0.1$ and $\eta_0 = 0$.

Chapter 6

Parameter Study

The excellent performance of the upper bound solution for the Von-Mises solid limit case and of the upper and lower bound flat punch solutions for cohesive-frictional porous materials are very strong arguments in favor of the use of the upper bound solution for indentation analysis. On this background, this Chapter examines how the hardness-to-cohesion ratio H/c^s depends on the different parameters, in particular the semi-apex angle θ. The question is motivated by *multiple indenter approaches* which became recently popular in the indentation literature. Multiple indenter approaches aim at overcoming the non-uniqueness of the reverse analysis of a single indentation test by means of multiple indentation tests with different geometry. The approach we develop below for porous cohesive-frictional materials is of a similar vain, but instead of making use of the dependence of the hardness on the cone angle (which we find to be weak), we identify hardness–packing density scaling relations for flat punch, Berkovich, and Cube Corner indentation.

6.1 Motivation: Multiple Indenter Approach

It was recently recognized that the extraction of material properties from the reverse analysis of a single indentation test suffers from non-uniqueness (see e.g. [17]). Several multiple indenter approaches have been proposed to overcome this limitation for elasto-plastic cohesive materials with or without power-law strain hardening using conical or pyramidal indenters [34] [12] [15]

[27] [71] [37] (see also Section 2.2.2). The key idea of the multiple indenter approach is to exploit the self-similarity of the indentation test w.r.t. the indenter geometry; i.e. for conical indentation from the dependence of the dimensionless relations (2.17) on the tip apex angle θ. Using our upper bound approach for conical indentation, we follow a similar strategy here to find out whether it is possible to extract the cohesion c^s and the friction coefficient α from the hardness-to-cohesion relation of cohesive-frictional porous materials:

$$\frac{H}{c^s} = \mathcal{F}\left(\alpha, \varphi, \eta_0, \theta\right) \tag{6.1}$$

It is readily understood that the number of indentation results obtained with different apex angles should equal the number of unknown constants in the constitutive model [34], i.e. two hardness measurements for cohesive-frictional porous materials, if the porosity $\varphi = 1 - \eta$ and the pore morphology η_0 are known. This is a necessary, but not sufficient condition. Indeed, the uniqueness of such a dual indentation procedure needs to be ensured. This motivates the detailed study of relation (6.1) for different semi-apex angles, namely (see Section 2.1.2, Tab. 2.1): flat punch ($\theta = 90°$), Berkovich ($\theta = 70.32°$) and Cube Corner ($\theta = 42.28°$).

6.2 Comparative Results

We carried out a great number of simulations by varying the four parameters in (6.1). This Section provides an overview of the results in a compact form.

6.2.1 Visualization of Velocity Fields

A first screening of the velocity fields obtained with the upper bound approach provides some insight into the particular indentation behavior of cohesive-frictional *porous* materials. Figure 6-1 compares the indentation velocity fields of two materials having the same friction coefficient and the same morphology (here matrix-pore inclusion), but different porosities. There is a clear difference in the limit behavior: the plastic zone contributing to the overall dissipation is greater for smaller porosities than for larger porosities, and appears to be dominantly dilating (except for a narrow zone below the indenter). By contrast, in the case of greater porosities, the material bulk that contributes to the dissipation capacity is concentrated into a narrow band parallel to the indenter-material interface, where the material undergoes primarily a plastically contracting behavior. This difference in activated bulk volume contributing to the dissipation explains why higher porosity materials have a lower overall hardness-to-cohesion ratio.

The velocity fields are also influenced by the pore morphology. By way of illustration, figure 6-2 compares the indentation velocity fields of two materials having the same friction coefficient and the same porosities but different pore morphologies: a matrix-pore inclusion morphology (MT, Fig. 6-2(a, c, e)) vs. a polycrystal morphology (SC, Fig. 6-2(b, d, f)). There is a clear difference in the limit behavior: the Mori-Tanaka morphology generates a diffuse velocity field around the indenter, while the Self-Consistent morphology entails a more localized response. In other words, for the same solid friction coefficient and same porosity, the MT-model activates more volume to contribute to the overall dissipation capacity than the SC-model. As a consequence, the hardness-to-cohesion ratio is greater for MT than for SC.

Finally, in all cases, there appears to be an effect of the cone angle on the extent of the plastic velocities field: as the cone becomes flatter, more material is activated. The hardness-to-cohesion ratio is greater for the Berkovich ($\theta = 70.32°$) than for the Cube Corner ($\theta = 42.28°$), and it is the highest for the flat punch ($\theta = 90°$).

6.2.2 Contour Plots $\mathcal{F}(\alpha, \varphi)$

A convenient way to display discrete data points is in form of a contour plot which transforms the discrete data system into a continuous distribution of linearly interpolated data points. We apply this technique to the H/c^s values for each apex angle θ and homogenization scheme η_0. Figures 6-3 and 6-4 display the contour plots for the Mori-Tanaka scheme ($\eta_0 = 0$) and the Self-Consistent Scheme ($\eta_0 = 1/2$), respectively.

The curved solid line on the left of the figures correspond to the limit case, $\lim_{\varphi \to \varphi^{\text{lim}}} H/c^s$, where φ^{lim} stands for the limit porosity defined by (3.57) and (3.58) (see Section 3.2.5 and discussion below). Furthermore, a comparison of the contour-plots 6-3 and 6-4 for different cone angles shows that the hardness-to-cohesion ratio increases with the cone angle. We have already noted this effect in the pure Von-Mises Solid case $\left(\varphi^{\text{lim}} = 0\right)$ (see Fig. 5-10). To analyze

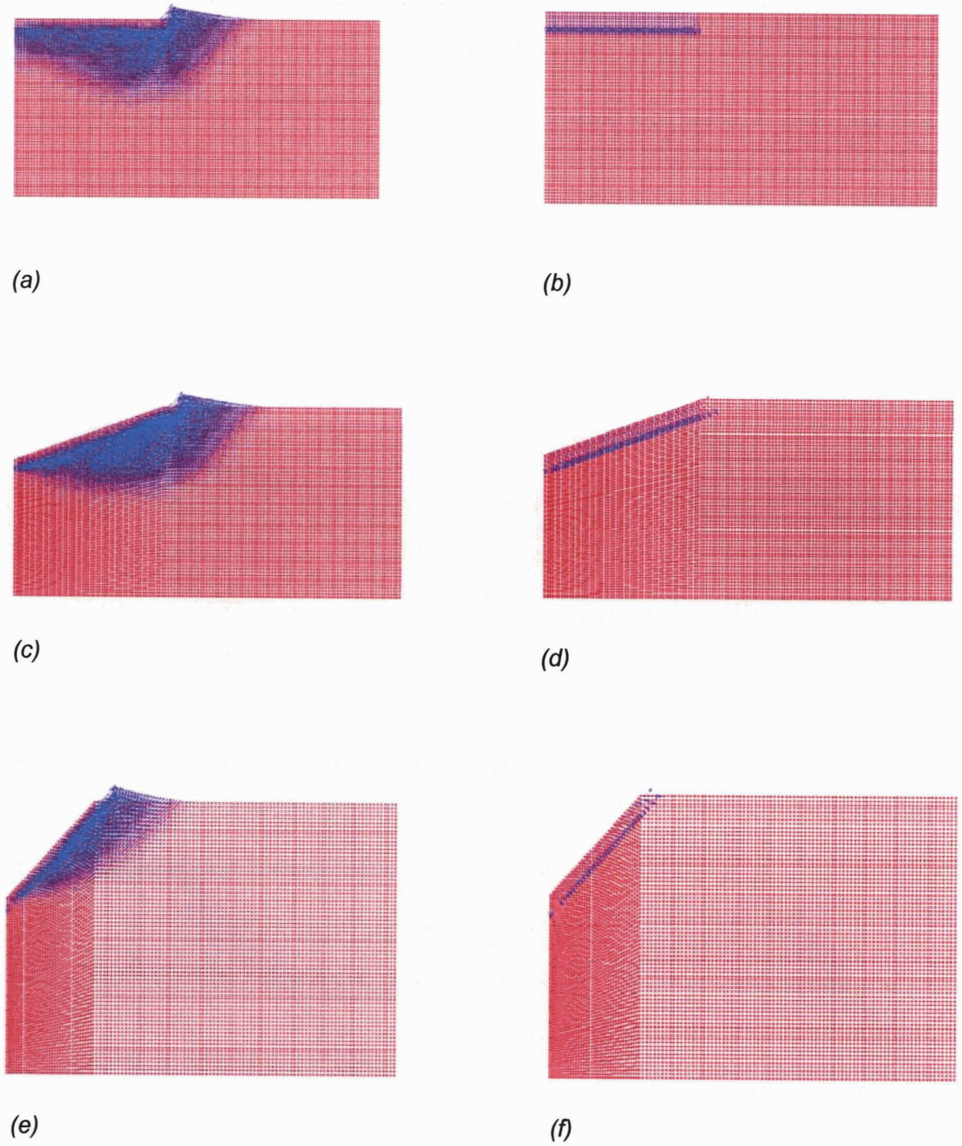

(a) (b) (c) (d) (e) (f)

Figure 6-1: Effect of the porosity on the indentation velocity fields of cohesive-frictional porous materials: *Flat Punch and* $\alpha = 0$ for (a) $\varphi = 0.1$ and (b) $\varphi = 0.3$. *Berkovich and* $\alpha = 0.05$ for (c) $\varphi = 0.033$ and (d) $\varphi = 0.3$. *Cube Corner and* $\alpha = 0.25$ for (e) $\varphi = 0.133$ and (f) $\varphi = 0.7$. (Results with Mori-Tanaka scheme $\eta_0 = 0$).

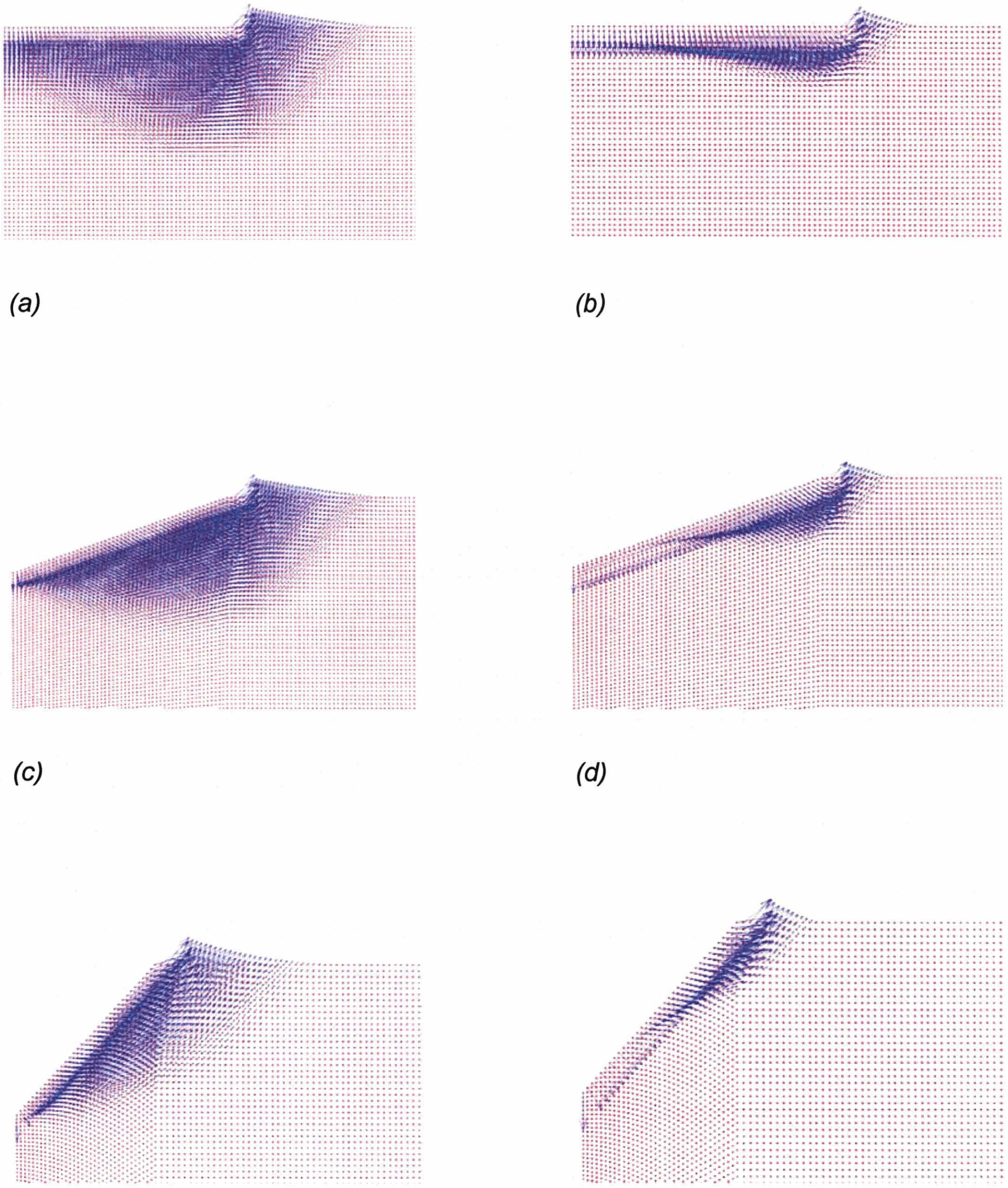

(a) (b)

(c) (d)

(e) (f)

Figure 6-2: Effect of the pore morphology on the indentation velocity fields for cohesive-frictional porous materials: *Mori-Tanaka Scheme* ($\eta_0 = 0$) for (a) flat punch ($\alpha = 0.15$, $\varphi = 0.1$), (c) Berkovich ($\alpha = 0.05$, $\varphi = 0.033$) and (e) Cube Corner ($\alpha = 0.25$, $\varphi = 0.133$). *Self-Consistent Scheme* ($\eta_0 = 1/2$) for for (b) flat punch ($\alpha = 0.25$, $\varphi = 0.2$), (d) Berkovich ($\alpha = 0$, $\varphi = 0.1$) and (f) Cube Corner ($\alpha = 0.2$, $\varphi = 0.2$).

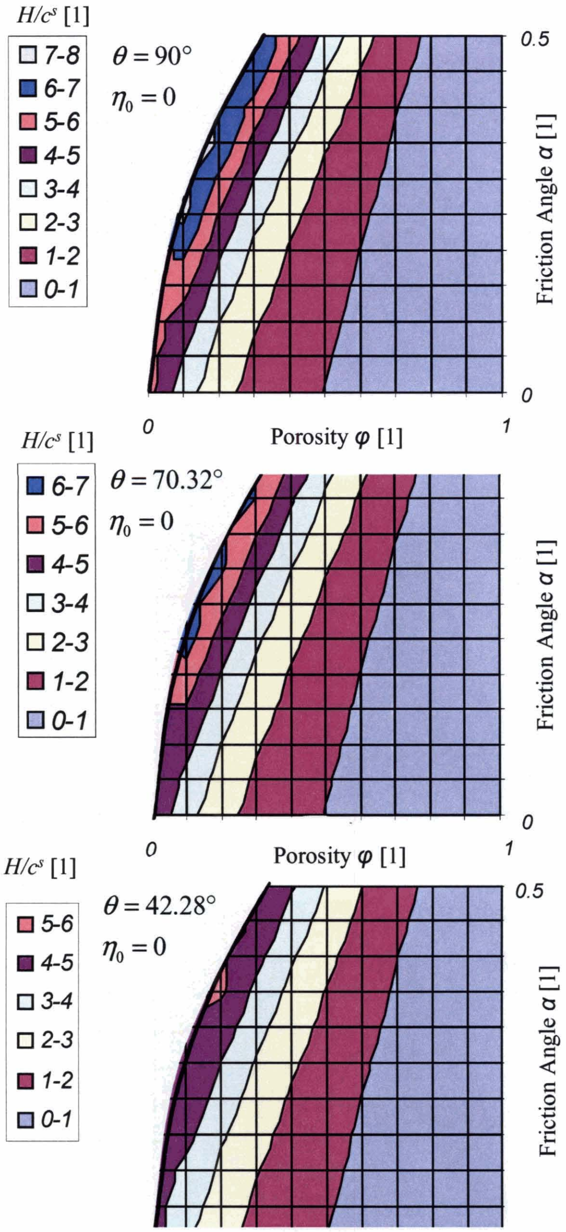

Figure 6-3: Friction–porosity contour plots of the hardness-to-cohesion ratio $H/c^s = \mathcal{F}(\alpha, \varphi)$ for three semi-apex angles θ corresponding to (from top to down) the Flat punch, the Berkovich and the Cube Corner indentation. The results are for the matrix-pore inclusion morphology (Mori-Tanaka, $\eta_0 = 0$).

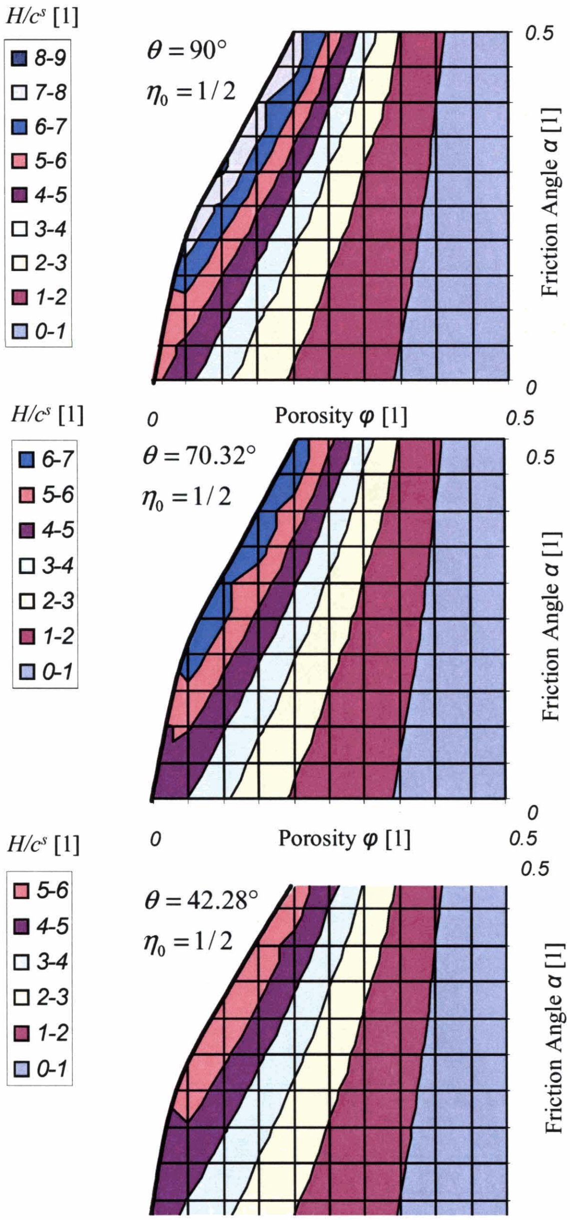

Figure 6-4: Friction–porosity contour plots of the hardness-to-cohesion ratio $H/c^s = \mathcal{F}(\alpha, \varphi)$ for three semi-apex angles θ corresponding to (from top to down) the Flat punch, the Berkovich and the Cube Corner indentation. The results are for the polycrystal morphology (Self-Consistent, $\eta_0 = 1/2$).

this behavior, we introduce the following hardness ratios:

$$\mathcal{H}_{CC}^{FP} = \frac{H\left(\theta = 90^{\circ}\right)}{H\left(\theta = 42.28^{\circ}\right)};\ \mathcal{H}_{CC}^{B} = \frac{H\left(\theta = 70.32^{\circ}\right)}{H\left(\theta = 42.28^{\circ}\right)} \tag{6.2}$$

The super- and subscripts FP, B, CC stand for 'Flat Punch', 'Berkovich and Cube Corner, respectively. Figures 6-5 and 6-6 display for each homogenization scheme the contour plots of the hardness ratios. The figures reveal that the highest hardness contrast is achieved at the limit case $\varphi \longrightarrow \varphi^{\text{lim}}$, and that the contrast reduces as the material becomes more and more porous.

6.2.3 The Limit Case of Cohesive-Frictional Porous Materials

We have a closer look on the limit case $\lim_{\eta \rightarrow \eta^{\text{lim}}} H/c^s$, where $\eta^{\text{lim}} = 1 - \varphi^{\text{lim}}$ is the limit packing density (or solid concentration), for which the elliptical strength criterion is defined. We recall (3.57) and (3.58) in the form:

$$\eta_0 = 0 \leq \eta < \eta_{mt}^{\text{lim}} = 1 - \frac{4}{3}\alpha^2 \tag{6.3}$$

$$\eta_0 = 1/2 \leq \eta < \eta_{sc}^{\text{lim}} = \frac{1}{2}\left(\sqrt{(9 + 32\alpha^2 + 64\alpha^4)} - 1\right) - 4\alpha^2 \tag{6.4}$$

Figure 6-7 displays, for Berkovich ($\theta = 70.32^{\circ}$) and Cube Corner ($\theta = 42.28^{\circ}$), the limit values $\lim_{\eta \rightarrow \eta^{\text{lim}}} H/c^s$ as a function of the limit packing density η^{lim}, corresponding to friction coefficients of $\alpha \in [0, 0.5]$. The general trend observed for the lower bound flat punch solution (see Figs. 3-8 and 5-12) is found to hold for all cone angles: an increase of $\lim_{\eta \rightarrow \eta^{\text{lim}}} H/c^s$ close to the pure solid state, followed by a decrease as the material becomes increasingly porous. We have explained this behavior by the effect of friction on highly filled systems in Section 5.2.2.

To fully apreciate this limit case, we plot in figure 6-8 the Berkovich-to-Cube Corner hardness ratio $\mathcal{H}_{CC}^{B}$ as a function of the limit packing density for the two homogenization schemes. Let us note that $\mathcal{H}_{CC}^{B}$ in this limit case is a priori a function of α and η_0; i.e. $\mathcal{H}_{CC}^{B} = \mathcal{H}_{CC}^{B}\left(\alpha, \eta_0\right)$. An important observation from figure 6-8 is that the ratio of the hardness limit values can be

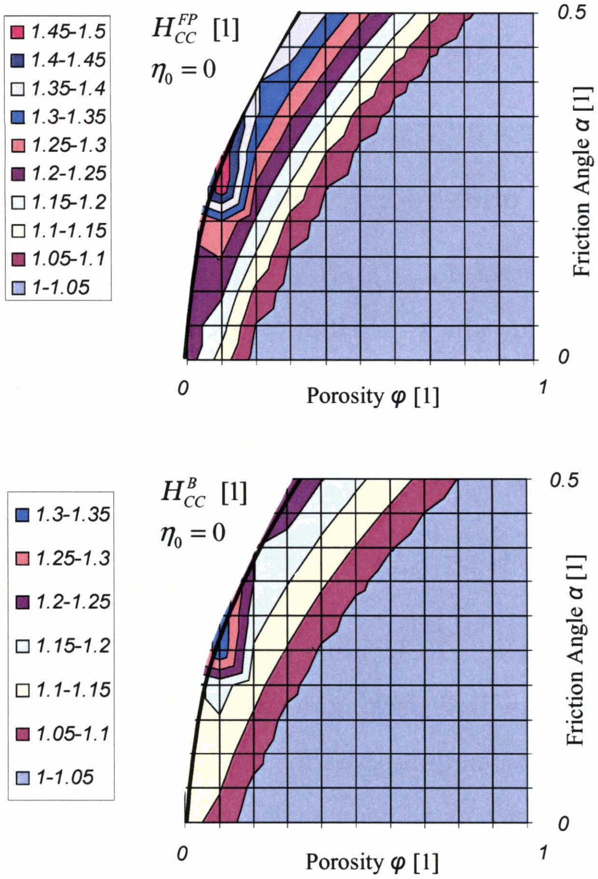

Figure 6-5: Hardness Ratios for Mori-Tanaka Scheme (matrix-pore inclusion morphology, $\eta_0 = 0$): $\mathcal{H}_{CC}^{FP}$: Flat punch–over–Cube Corner Hardness (top), $\mathcal{H}_{CC}^{B}$: Berkovich–over–Cube Corner Hardness (bottom).

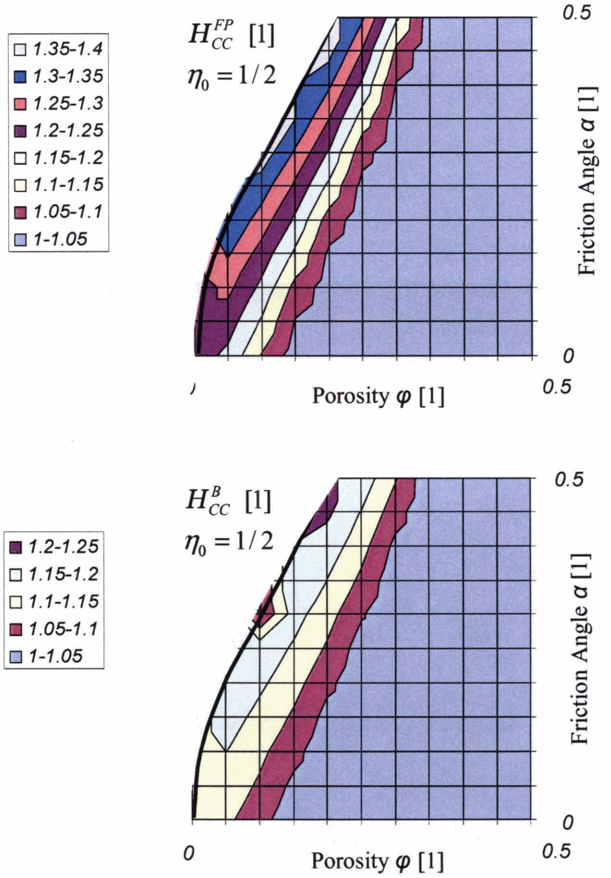

Figure 6-6: Hardness Ratios for Self-Consistent Scheme (polycrystal morphology, $\eta_0 = 1/2$): $\mathcal{H}_{CC}^{FP}$: Flat punch–over–Cube Corner Hardness (top), $\mathcal{H}_{CC}^{B}$: Berkovich–over–Cube Corner Hardness (bottom).

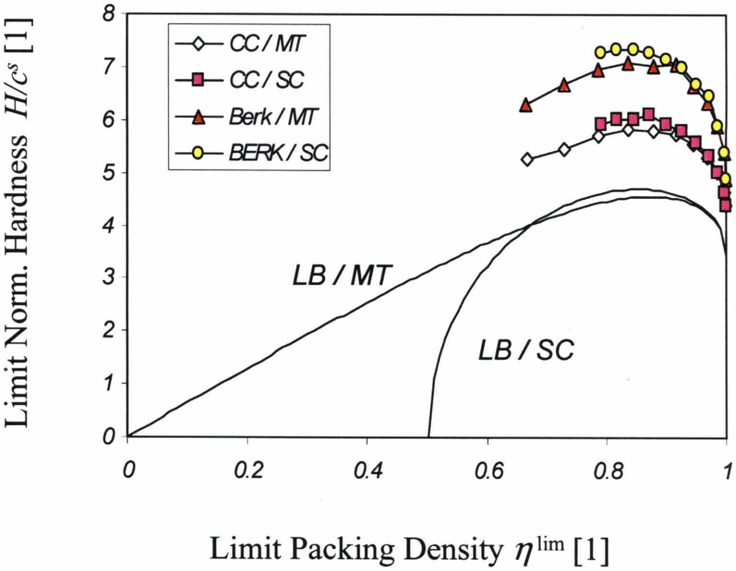

Figure 6-7: Effect of the cone angle on $\lim_{\varphi\rightarrow\varphi^{\text{lim}}} H/c^s$ as a function of the limit packing density $\eta^{\text{lim}} = 1 - \varphi^{\text{lim}}$. (B = Berkovich ($\theta = 70.32°$), CC = Cube Corner ($\theta = 42.28°$), MT = Mori-Tanaka ($\eta_0 = 0$) and SC = Self-Consistent scheme ($\eta_0 = 1/2$).

represented as a function of a single variable, the limit packing density $\eta^{\text{lim}} = \eta^{\text{lim}}(\alpha)$:

$$\mathcal{H}_{CC}^{B} = \frac{\lim_{\eta \to \eta^{\text{lim}}} H/c^{s}\left(\theta = 70.32^{\circ}\right)}{\lim_{\eta \to \eta^{\text{lim}}} H/c^{s}\left(\theta = 42.28^{\circ}\right)} = \mathcal{H}_{CC}^{B}\left(\eta^{\text{lim}}\right) \tag{6.5}$$

This is an important result in several regards:

1. Our results can be seen as an extension to cohesive-frictional *porous* materials of previous investigations of hardness-strength relations for cohesive-frictional *solids* [37]. Instead of hardness ratio $\mathcal{H}_{CC}^{B}$ – friction angle relations (see Fig. 2-5), we suggest that the appropriate parameter for cohesive-frictional porous materials is the limit packing density $\eta^{\text{lim}} = \eta^{\text{lim}}(\alpha, \eta_0)$, which combines both the solid's friction coefficient and the microstructural morphology, namely the percolation threshold η_0.
2. For cohesive-frictional solids, the hardness ratio (6.5) has been suggested as input for the reverse analysis of the friction angle by means of the so-called Dual-Indentation technique (see Section 2.2.2). It is readily understood from the results in figure 6-8 that the uniqueness of the reverse analysis cannot be ensured for a cohesive-frictional porous material (at its limit state), as $\mathcal{H}_{CC}^{B}\left(\eta^{\text{lim}}\right)$ is not a mononone decreasing function. In addition, the low hardness contrast between different cone angles that dominates the behavior for $\eta_0 \leq \eta < \eta^{\text{lim}}$ (see Figs. 6-5 and 6-6) makes it difficult to imagine an efficient dual-indentation technique to work for cohesive-frictional *porous* materials.

6.2.4 Hardness–Packing Density Scaling Relations

On first sight, the impossibility to use a multiple indenter approach to extract the strength properties of cohesive-frictional porous materials may come as a disappointment. However, upon scrutiny the same results allow us to merge two invariants for the limit case, namely the friction coefficient α and the pore morphology represented by the percolation threshold η_0 into one, the limit packing density $\eta^{\text{lim}} = \eta^{\text{lim}}(\alpha, \eta_0)$. This is of great value as we will see here below.

Figure 6-9 shows normalized hardness-packing density scaling relations for different friction angles α, cone angles θ and pore morphologies. We readily find that it is not possible, except

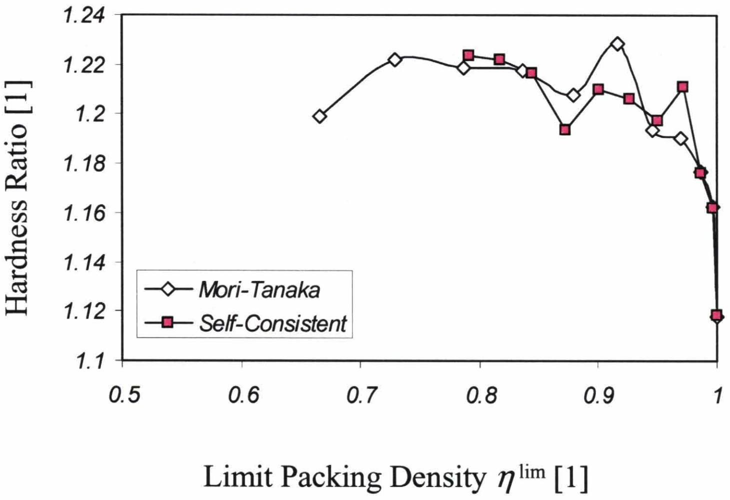

Figure 6-8: Berkovich-to-Cube Corner hardness ratio $\mathcal{H}_{CC}^{B}$ as a function of the limit packing density $\eta^{\lim} = 1 - \varphi^{\lim}(\alpha)$.

for the zero-friction case, to scale the hardness response of two porous materials as a function of α and η, since the curves do not approach the same asymptotic value. Figure 6-10 shows scaling relations of the form (6.7) for small values of α, for which the limit packing densities (6.3) and (6.4) coincide:

$$\eta_{sc}^{\lim} = 1 - \frac{4}{3}\alpha^2 + O\left(\alpha^4\right) \approx \eta_{mt}^{\lim} \tag{6.6}$$

In this case, the hardness–packing density scaling relations converge towards the same asymptotic value. Extending this observation to higher friction angles, we suggest the following hardness-packing density scaling relation, in which α is replaced by the limit packing density $\eta^{\lim}$:

$$\boxed{\frac{H}{c^s} = \mathcal{F}\left(\eta = 1 - \varphi, \eta_0, \eta^{\lim}, \theta\right)} \tag{6.7}$$

A further normalization of both the hardness by its asymptotic value $\lim_{\eta \to \eta^{\lim}} H/c^s$ and of the packing density η by its limit value $\eta^{\lim}$ provides a means to collapse for each scheme all curves into one single curve, a master-curve. In order to obtain a normalization for each scheme where all the curves have the same initial and final points, the normalization of the η-axis is

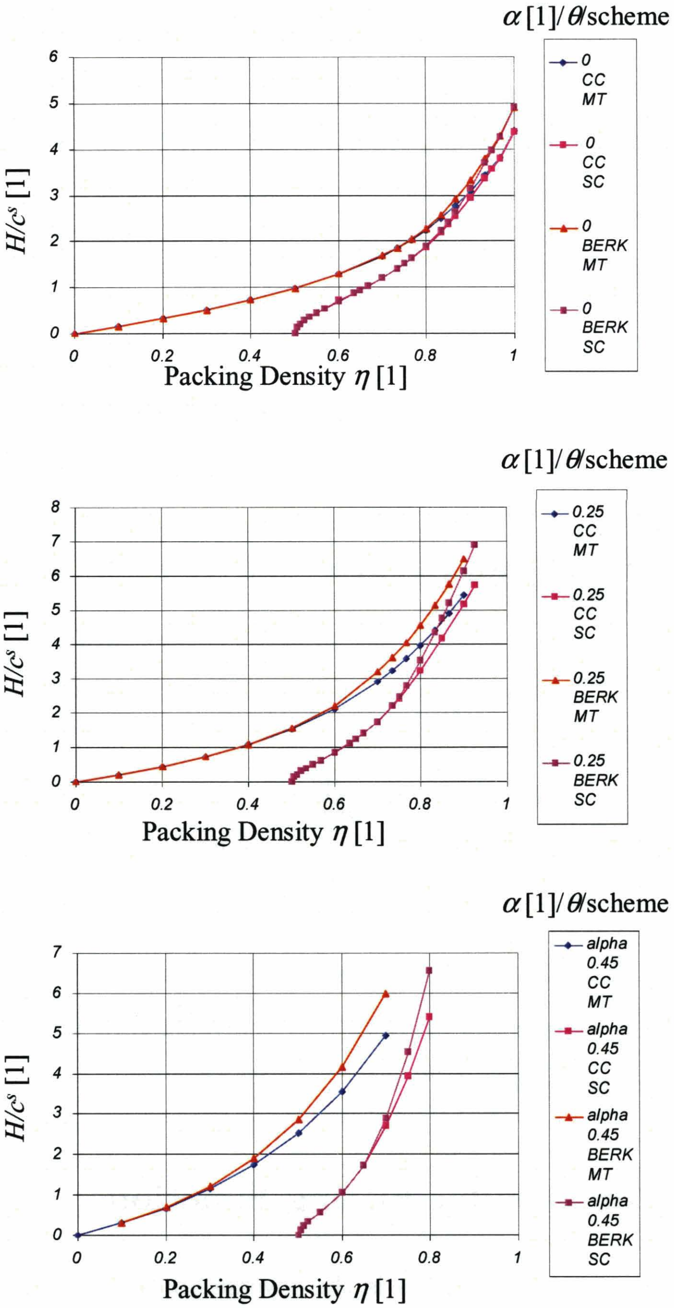

Figure 6-9: Normalized hardness-packing density scaling relations of the form (6.1) for (a) $\alpha = 0$, (b) $\alpha = 0.25$ and (c) $\alpha = 0.45$. (BERK = Berkovich, CC = cube corner, MT = Mori Tanaka scheme, SC = Self-Consistent Scheme).

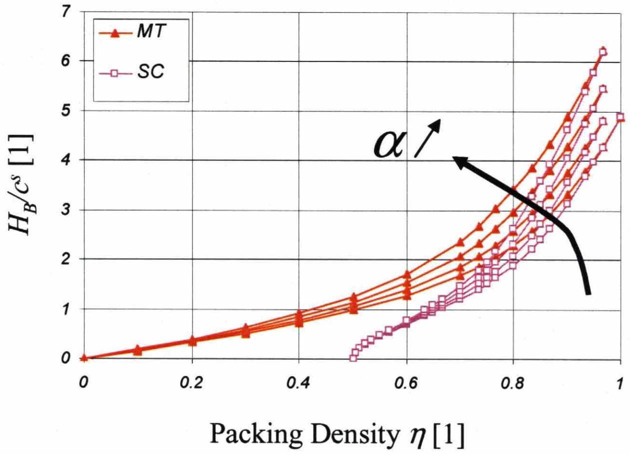

Figure 6-10: Berkovich Hardness–packing density scaling for small values of α, for which the limit packing density of the Mori-Tanaka scheme and of the Self-Consistent Scheme coincide. (Results for $\alpha = 0 - 0.05 - 0.1 - 0.15$).

done as follows:

$$\text{MT:} \qquad \eta \rightarrow \frac{\eta}{\eta^{\text{lim}}} \tag{6.8a}$$

$$\text{SC:} \qquad \eta \rightarrow 0.5\left(1+\frac{2\eta-1}{2\eta^{\text{lim}}-1}\right) \tag{6.8b}$$

These two master-curves of the double-normalized hardness–packing density scaling relation are shown in figure 6-11. We identify for both pore morphologies, MT and SC, a characteristic curve which depends primarily on η/η^{lim}.

6.3 Summary of Results: Fitting Functions

The ultimate goal of indentation analysis is the reverse analysis of material properties of the indented material. In our case, these are the cohesion c^s and the friction coefficient α of the solid phase of the porous material. The aim of this Section is to derive fitting functions that summarize the results in closed form expressions so that these expressions can be used for data analysis. Motivated by the good performance of the lower bound solutions developed in

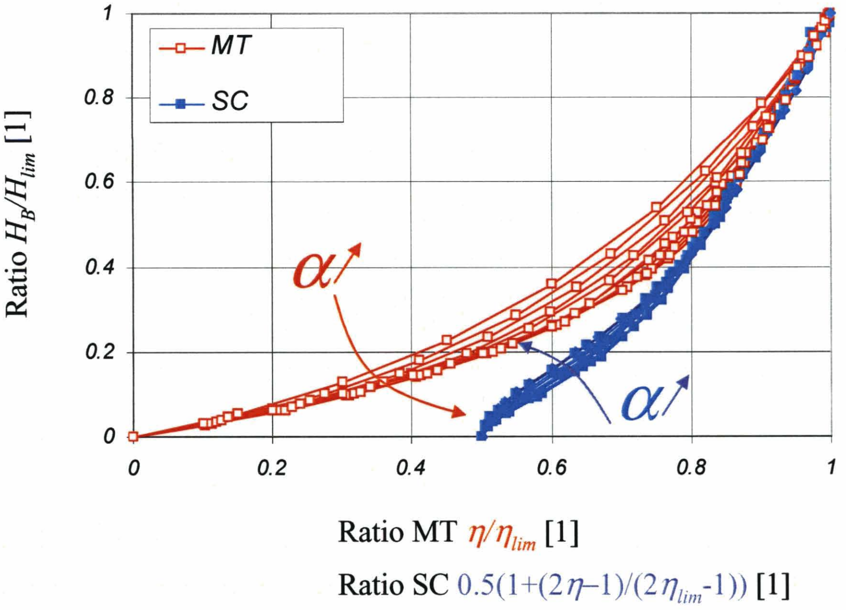

Figure 6-11: Double-normalized hardness–packing density scaling relations: H/c^s is normalized by $\lim_{\eta\rightarrow\eta^{\text{lim}}} H/c^s$ and η by η^{lim} (Eq. (6.8a) for MT; Eq. (6.8b) for SC) (Results for $\alpha = 0, 0.5, 0.1...0.5$).

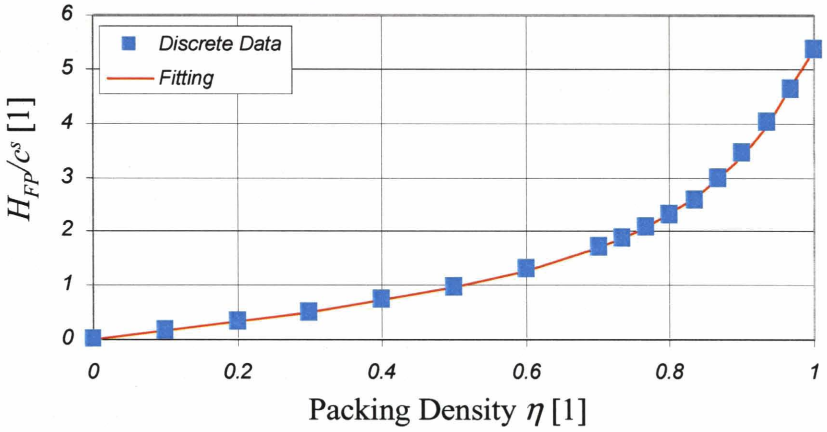

Figure 6-12: Fitting of the flat punch simulation data ($\theta = 90°$) obtained for a Von Mises solid phase ($\alpha = 0$) with a Mori Tanaka scheme ($\eta_0 = 0$).

Chapter 3, we fit our results to mathematical expressions that have a similar shape and limit behavior. We illustrate the fitting procedure for the Von-Mises case, and present the results for the Drucker-Prager solid in a concise form afterwards.

6.3.1 Von-Mises Solid

Choice of Fitting Functions for the Mori-Tanaka scheme

The fitting function we choose for the hardness–packing density scaling relation of a porous material composed of a Von-Mises solid is inspired by the lower bound expression (3.73) for the Mori-Tanaka scheme:

$$\frac{H_{mt}}{c^s} = 12\eta \frac{(7 + a_{mt}\eta)\sqrt{(8 + b_{mt}\eta)}}{184 + c_{mt}\eta + d_{mt}\eta^2} \tag{6.9}$$

where $(a_{mt}, ..., d_{mt})$ are four fitting parameters that minimize for each semi-apex angle the difference between the fitting functions and the discrete simulation data. This minimization is done with the solver of Excel and leads to the values displayed in Table 6.1

An exemple of fitting is displayed in Fig. 6-12.

Choice of Fitting Functions for the Self Consistent Scheme

In a similar manner, the fitting function we choose for the hardness–packing density scaling relation of a porous material composed of a Von-Mises solid is inspired by the lower bound expression (3.73) for the self consistent scheme:

$$\frac{H_{sc}^{-}}{c^s} = \mathcal{F}_{sc}^{-}\left(\varphi, \eta_0 = 1/2\right) = 12\frac{\left(1-\varphi\right)\left(a_{sc}-3\varphi\right)\sqrt{\left(1-2\varphi\right)}}{\left(b_{sc}-3\varphi\right)\sqrt{\left(c_{sc}+d_{sc}\varphi\right)}} \tag{6.10}$$

and the coefficients are given in Table 6.1.

6.3.2 Drucker-Prager Solid

We want to extend these fitting functions to the Drucker Prager case.

Choice of Fitting Functions for the Mori-Tanaka Scheme

We are looking for a fitting which takes into account the analytical form of the lower bound expression (3.78) for the Mori-Tanaka scheme and which is similar to the fitting function (6.9) obtained for the Von-Mises solid. For the Mori Tanaka scheme, we are therefore looking for an expression of the form:

$$\frac{H_{mt}}{c^s} = 12\eta\frac{30\alpha - 12\alpha\eta + 4\alpha^2\sqrt{8-5\eta} + \left(7 + a_{mt}\eta\right)\sqrt{8 + b_{mt}\eta}}{16\alpha^4 - 124\alpha^2 + 64\alpha^2\eta + 184 + c_{mt}\eta + d_{mt}\eta^2} \tag{6.11}$$

In order to give some flexibity to this expression, we introduce a new parameter e_{mt} that depends on α:

$$\frac{H_{mt}}{c^s} = 12e_{mt}\left(\alpha\right)\eta\frac{30\alpha - 12\alpha\eta + 4\alpha^2\sqrt{8-5\eta} + \left(7 + a_{mt}\eta\right)\sqrt{8 + b_{mt}\eta}}{16\alpha^4 - 124\alpha^2 + 64\alpha^2\eta + 184 + c_{mt}\eta + d_{mt}\eta^2} \tag{6.12}$$

For each semi-apex angle, we want to determine the parameter e_{mt} for each α in order to get a general expression for H_{mt}/c^s. Because we want to fit the discrete simulation data with this expression by adapting only e_{mt}, it may be difficult in some cases to obtain a satisfactory fitting over the entire range of α and η values. It is therefore important to study the role of each parameter.

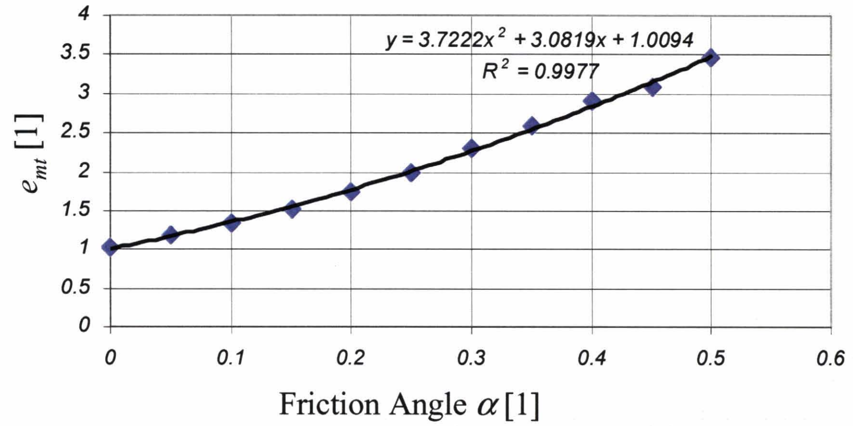

Figure 6-13: Fitting of e_{mt} for a Mori Tanaka scheme ($\eta_0 = 0$) and for a flat punch ($\theta = 90°$).

1. From the expression of the lower bound at limit packing density,

$$\lim_{\varphi=\varphi_{mt}^{\lim}=1-\eta_{mt}^{\lim}} \frac{H_{mt}^{-}}{c^s} = 3\eta \frac{3\sqrt{3}\sqrt{(1-\eta)}+2\sqrt{(8-5\eta)}}{5-2\eta} \tag{6.13}$$

   we realize that the cohesion c^s is directly determined from the limit value $\left(\eta_{mt}^{\lim}, \lim_{\varphi=\varphi_{mt}^{\lim}=1-\eta_{mt}^{\lim}} H_{mt}^{-}/c^s\right)$ once the value of $\eta_{mt}^{\lim}$, i.e. α, is known.

2. The vizualization of the simulation curves showing the evalution of H_{mt}/c^s as a function of the packing density shows that the value of α corresponds to how much the Von Mises curve shifts.

3. The experimental data considered for the fitting are within the range $\eta \in [0.5, 1]$

The fitting of e_{mt} is done for $\eta \in [0.5, 1]$ so that the experimental values lead to a realistic α and then to a realistic c^s estimate from the limit point $\left(\eta_{mt}^{\lim}, \lim_{\varphi=\varphi_{mt}^{\lim}=1-\eta_{mt}^{\lim}} H_{mt}/c^s\right)$.

The parameter e_{mt} is found to be well represented by a second order polynom, as illustrated in Fig. 6-13, so that eventually the final expression for H_{mt}/c^s is:

$$\frac{H_{mt}}{c^s} = 12\left(f_{mt} + g_{mt}\alpha + h_{mt}\alpha^2\right)\eta \frac{30\alpha - 12\alpha\eta + 4\alpha^2\sqrt{8-5\eta} + (7 + a_{mt}\eta)\sqrt{8 + b_{mt}\eta}}{16\alpha^4 - 124\alpha^2 + 64\alpha^2\eta + 184 + c_{mt}\eta + d_{mt}\eta^2} \tag{6.14}$$

	θ	a	b	c	d	f	g	h
$\eta_0 = 0$	90°	−1.3390	149.54	754.43	−779.65	1.0094	3.0819	3.7222
(MT)	70.32°	−1.0593	2.0739	−101.88	−35.9218	0.9833	1.7874	0
	42.28°	−0.9859	−5.7257	−207.2484	48.0926	0.9934	0.1249	0.5162
$\eta_0 = 0.5$	90°	9.1942	162.93	$1.5289 \cdot 10^{-2}$	0.1199	0.9992	−1.1929	4.0825
(SC)	70.32°	10.033	139.87	$2.9810 \cdot 10^{-2}$	0.1790	0.9951	−0.485	3.5491
	42.28°	35.348	78.529	1.5049	7.3505	0.9938	1.8573	3.4578

Table 6.1: Fitting coefficients

The coefficients are given in Table 6.1.

Choice of Fitting Functions for the Self Consistent Scheme

For the self consistent scheme, similar considerations lead to look for an expression of the form:

$$\frac{H_{sc}}{c^s} = 12 e_{sc}\left(\alpha\right)\left(1-\varphi\right) \cdot \frac{\sqrt{(c_{sc}+d_{sc}\varphi)(1-2\varphi)}\left(4(1-2\varphi)\alpha^2-(9+a_{cs})\varphi+3a_{cs}+3\varphi^2\right)+(1-2\varphi)\left(6\varphi^2-24\varphi+18\right)\alpha}{(64\varphi^2+16-64\varphi)\alpha^4+(24\varphi^3-124\varphi^2-60+176\varphi)\alpha^2-(9c_{cs}+b_{cs}c_{cs}-3b_{cs}d_{cs})\varphi+3\varphi^3 d_{cs}-\varphi^2(b_{cs}d_{cs}+9d_{cs}-3c_{cs})+3b_{cs}c_{cs}} \tag{6.15}$$

where e_{sc} has to be determined. For each semi-apex angle, we want to determine the parameter e_{sc} as a function of α in order to get a general expression for H_{sc}/c^s. The fitting of e_{sc} is done on a range $\eta \in [0.65, 1]$ so that the experimental values permit a realistic fitting of α and then c^s from the limit point $\left(\eta_{sc}^{\lim}, \lim_{\varphi=\varphi_{sc}^{\lim}=1-\eta_{sc}^{\lim}} H_{sc}/c^s\right)$.

The parameter e_{sc} is found to be well represented by a second order polynom, so that eventually, the final expression for H_{sc}/c^s can be written in the form:

$$\frac{H_{sc}}{c^s} = 12\left(f_{sc}+g_{sc}\alpha+h_{sc}\alpha^2\right)\left(1-\varphi\right) \cdot \frac{\sqrt{(c_{sc}+d_{sc}\varphi)(1-2\varphi)}\left(4(1-2\varphi)\alpha^2-(9+a_{cs})\varphi+3a_{cs}+3\varphi^2\right)+(1-2\varphi)\left(6\varphi^2-24\varphi+18\right)\alpha}{(64\varphi^2+16-64\varphi)\alpha^4+(24\varphi^3-124\varphi^2-60+176\varphi)\alpha^2-(9c_{cs}+b_{cs}c_{cs}-3b_{cs}d_{cs})\varphi+3\varphi^3 d_{cs}-\varphi^2(b_{cs}d_{cs}+9d_{cs}-3c_{cs})+3b_{cs}c_{cs}} \tag{6.16}$$

where the coefficients are given in Table 6.1.

This process leads to satisfactory fittings, as illustrated in Figures 6-14 and 6-15.

With the fitting functions defined, it is possible to determine the value of the hardness-to-

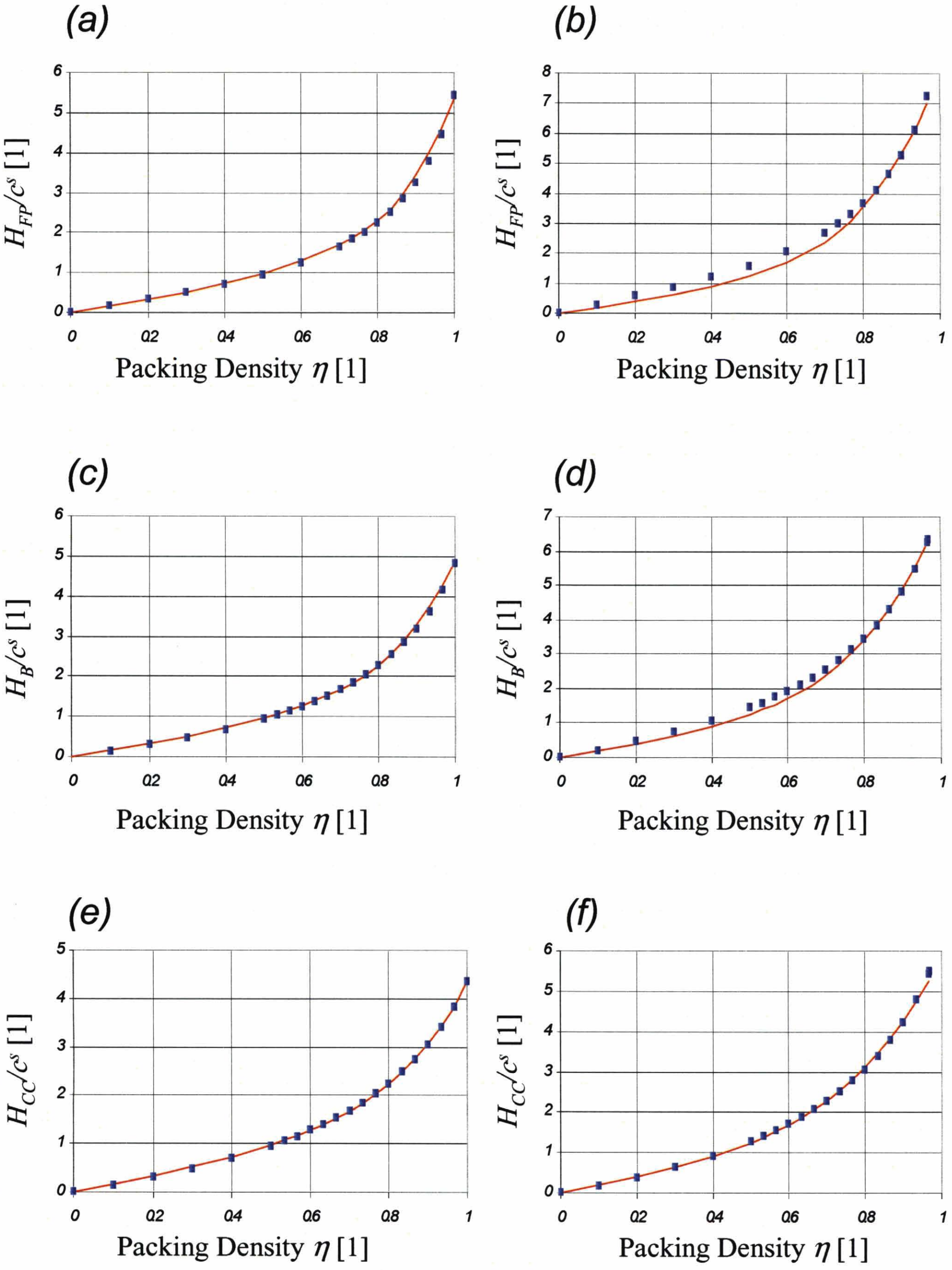

Figure 6-14: Comparaison between the fitting functions and the simulation data for the Mori Tanaka scheme: *Von-Mises Material* ($\alpha = 0$): (a) flat punch, (c) Berkovich and (e) cube corner. *Drucker Prager Material* ($\alpha = 0.15$): (b) flat punch, (d) Berkovich and (f) cube corner.

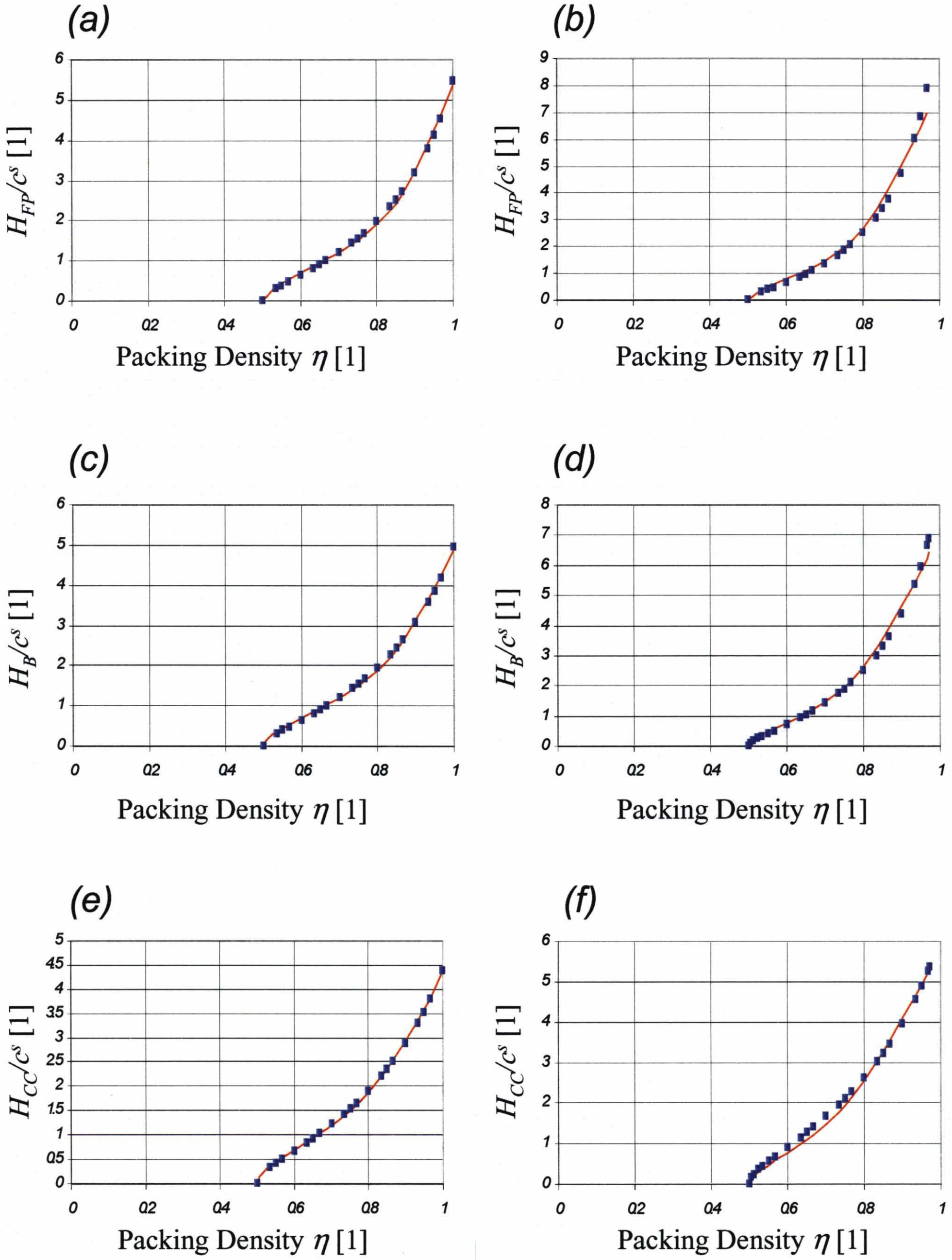

Figure 6-15: Comparaison between the fitting functions and the simulation data for the self consistent scheme: *Von-Mises Material* ($\alpha = 0$)*:* (a) flat punch, (c) Berkovich and (e) cube corner. *Drucker Prager Material* ($\alpha = 0.15$)*:* (b) flat punch, (d) Berkovich and (f) cube corner.

cohesion ratio for any values of friction angle and porosity. Without this fitting, the important number of simulations already carried a lot of information. As an exemple, these discrete data could be exploited to study the dependence of the hardness-to-cohesion ratio on the porosity for different values of friction angle, both for the Mori Tanaka scheme (Fig. 6-16) and for the self-consistent scheme (Fig. 6-17). Vice versa, the dependence of the hardness-to-cohesion ratio on the friction angle for different values of porosity could be plotted, both for the Mori Tanaka scheme (Fig. 6-18) and for the self consistent scheme (Fig. 6-19). The fitting functions enable a better understanding of the link between the hardness-to-cohesion ratio and the two parameters, the friction angle and the porosity. These fitting functions generalize the discrete simulation data and pave the way for experimental applications.

6.4 Conclusion

In order to overcome the non-uniqueness of the reverse analysis of a single indentation test, we found a strong link between the hardness and the packing density of the solid phase, that proved to be a very interesting parameter of the problem. By adapting the mathematical expressions found in Chapter 3, we were able to fit in a satisfactory way the simulation data with some closed form expressions that fit the data reasonably well.

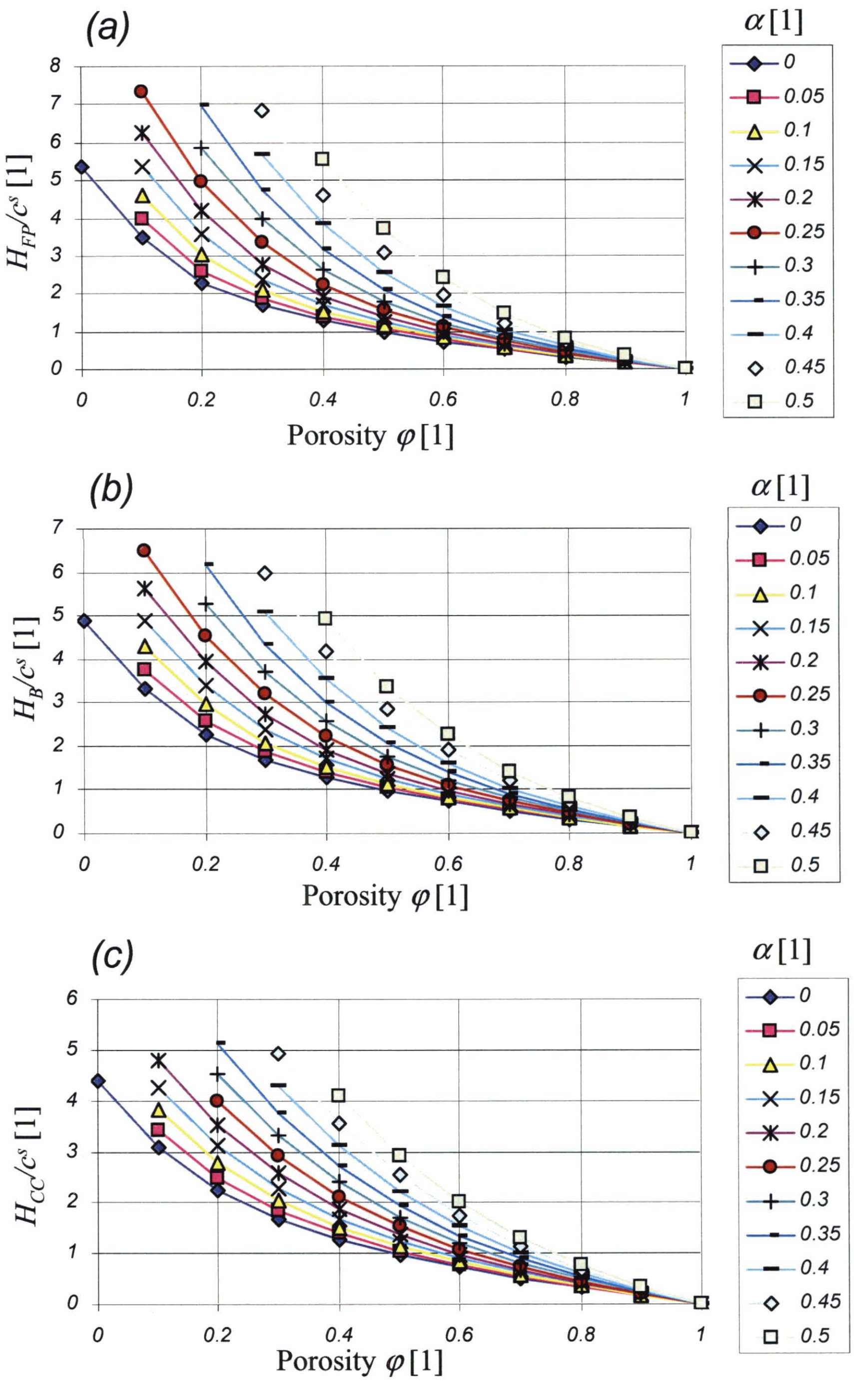

Figure 6-16: Dependence of the hardness-to-cohesion ratio H/c^s on the porosity φ for the Mori Tanaka scheme for different values of the friction coefficient α for (a) the flat punch, (b) Berkovich and (c) cube corner.

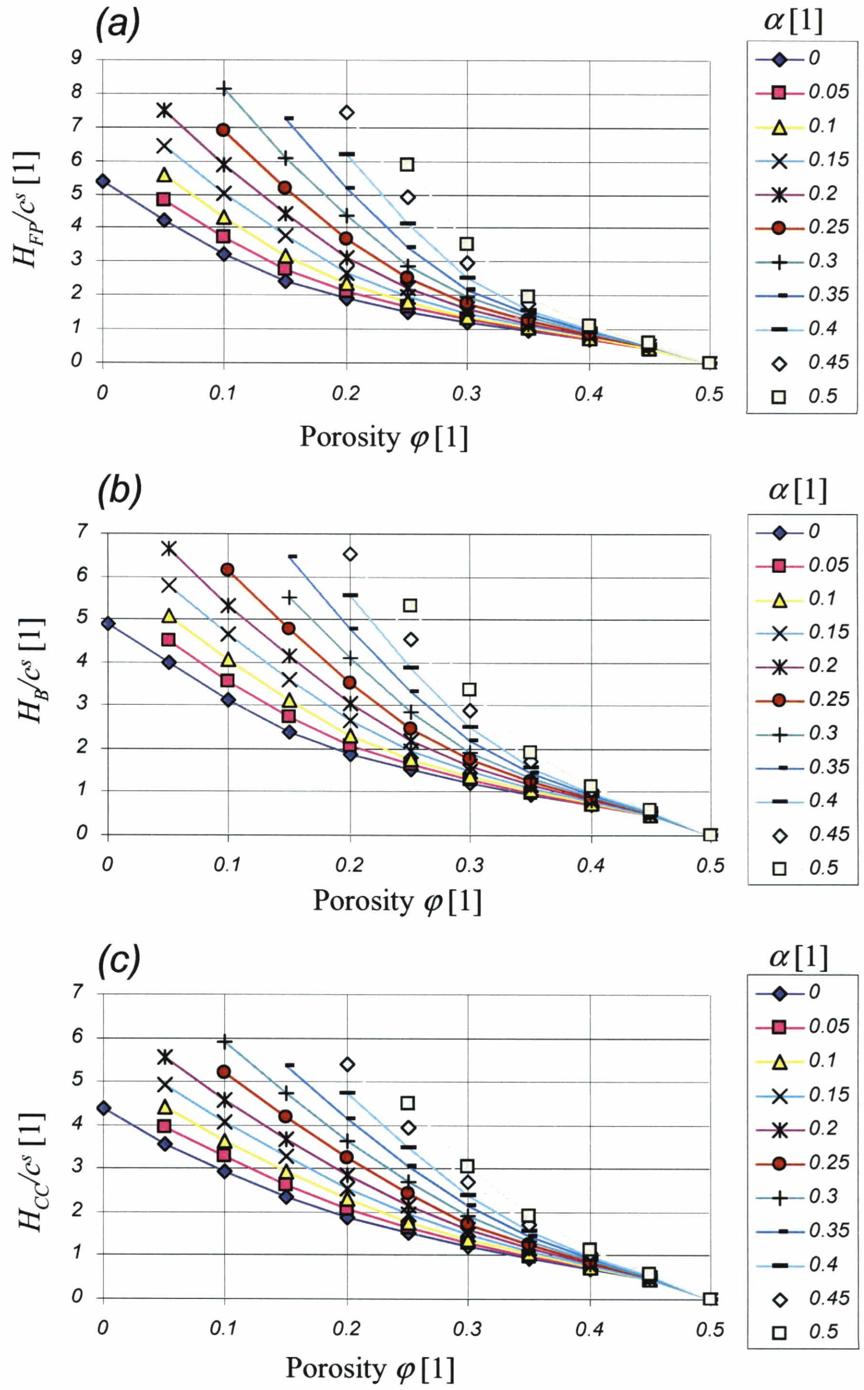

Figure 6-17: Dependence of the hardness-to-cohesion ratio H/c^s on the porosity φ for the self consistent scheme for different values of the friction coefficient α for (a) the flat punch, (b) Berkovich and (c) cube corner.

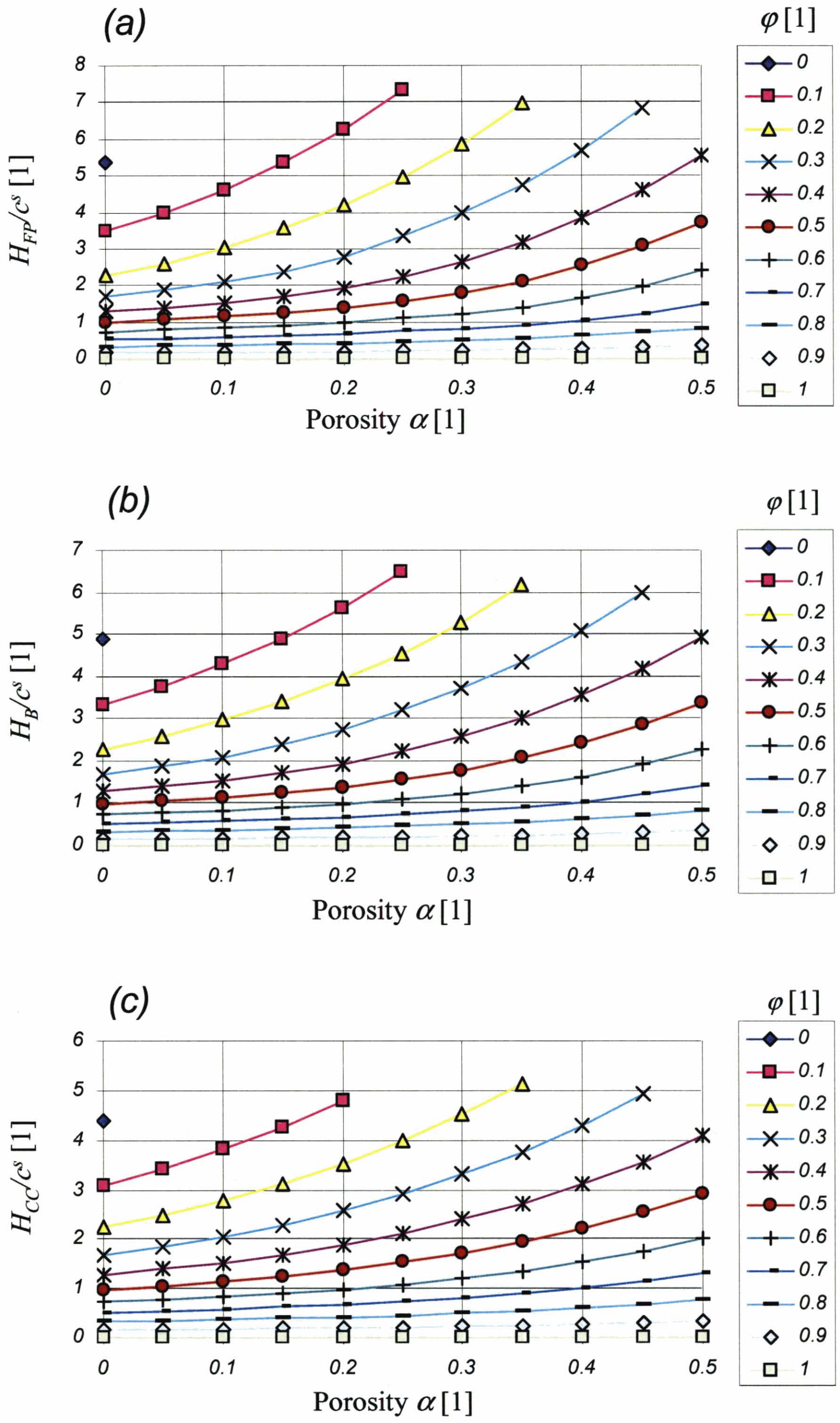

Figure 6-18: Dependence of the hardness-to-cohesion ratio H/c^s on the friction angle α for the Mori Tanaka scheme for different values of porosity φ for (a) the flat punch, (b) Berkovich and (c) cube corner.

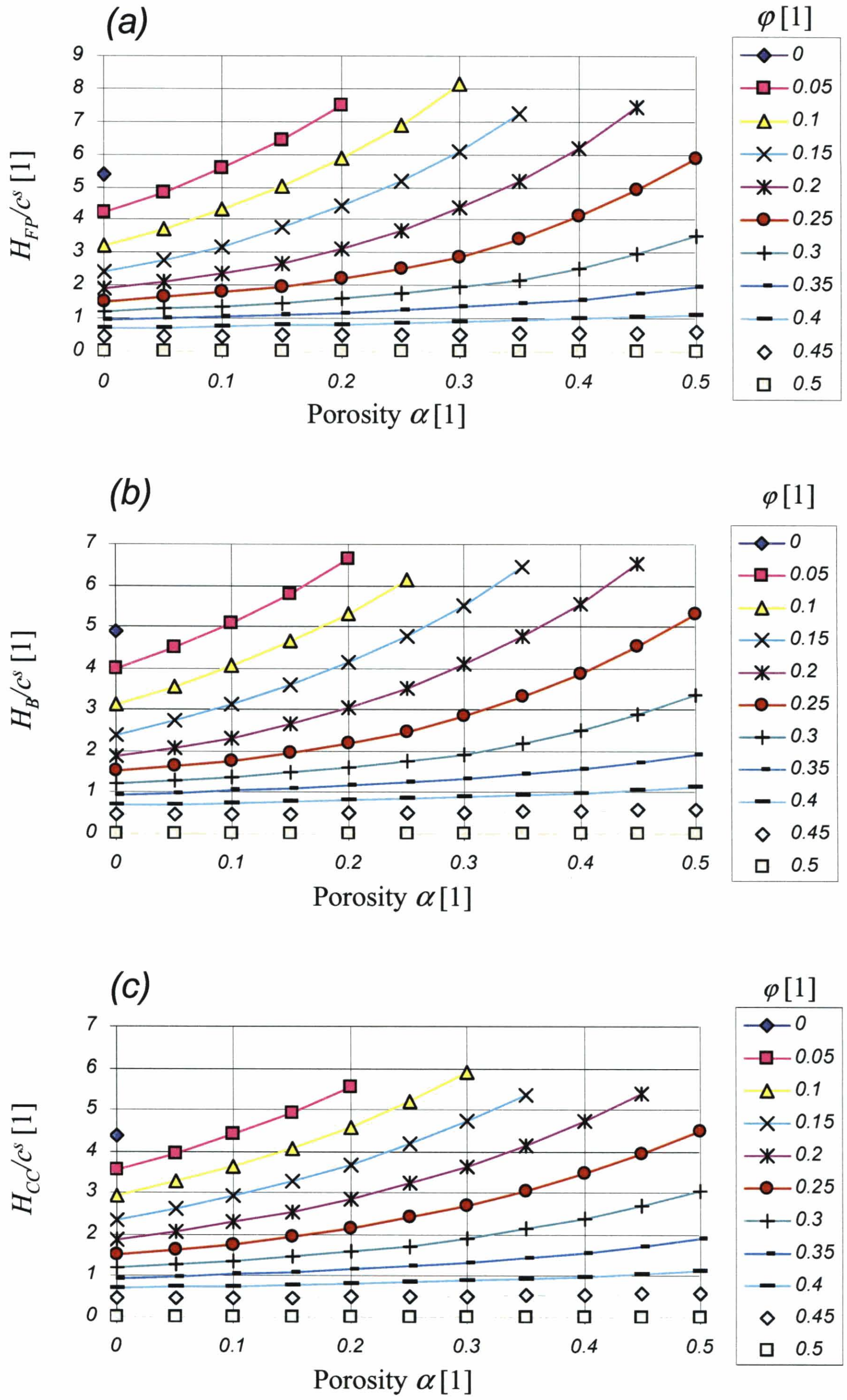

Figure 6-19: Dependence of the hardness-to-cohesion ratio H/c^s on the friction angle α for the Mori Tanaka scheme for different values of porosity φ for (a) the flat punch, (b) Berkovich and (c) cube corner.

Part IV

Application

Chapter 7

Shale Nano-Hardness Analysis

This last part and chapter shows the engineering application of our model to shales. Shales are sedimentary rocks that are ubiquitously present as sealing formations in hydrocarbon bearing reservoirs. They are made of highly compacted clay particles of sub-micrometer size, nanometric porosity and different mineralogy; in short, a challenging application for our hardness–packing density scaling relations. The first part of this Chapter reviews some elements of shale's microstructure with the aim of identifying the scale of application of our model. The particular nanoindenation technique employed to determine the hardness of shale's nano-fabric from nanoindenation is also presented. It extends previous works by Delafargue and Ulm [26] dealing with the nano-elasticity content of shales, to hardness measurements using the 'grid-indentation technique' developed by Constantinides and Ulm [23] (see Section 2.3). The nanoindenation and the statistical indentation analysis was performed by Chris Bobko for six shale materials. In the second part of this Chapter, we analyze the hardness values by means of the fitting functions developed in Chapter 6.

7.1 Multi-Scale Structure of Shale

Shales are probably one of the most complicated and intriguing natural materials present on earth. The multiphase composition is permanently evolving over various scales of length and time, creating in the course of this process the most heterogeneous class of materials in existence.

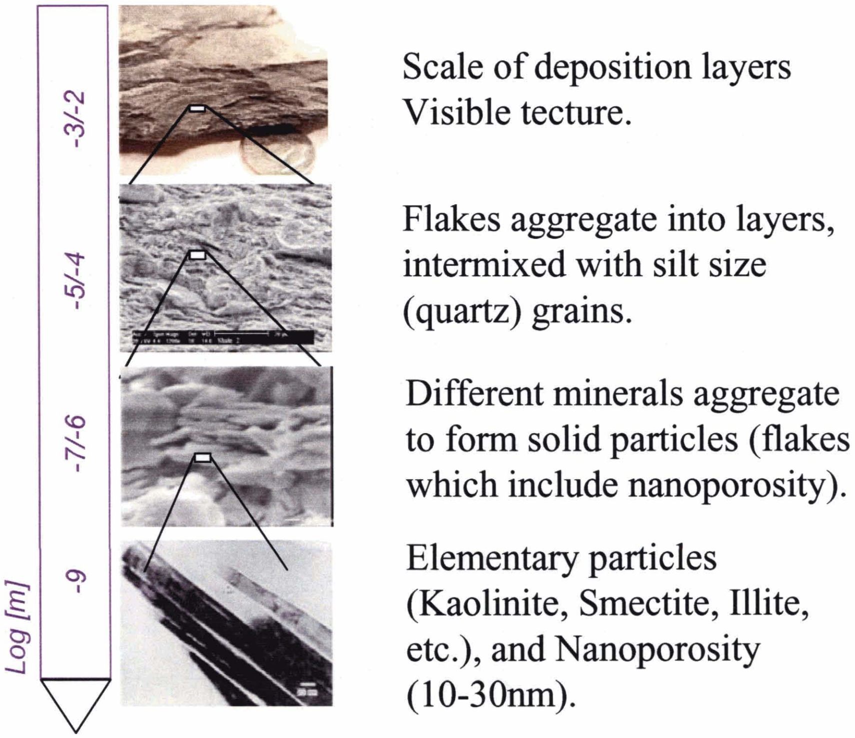

Figure 7-1: Multi-scale structure of shales (adapted from [79]): From top-down: The macroscale is the scale of visible deposition layers and detrital grains. The micro-scale (SEM picture) is the scale of a textured clay composite intermixed with silt size quartz grains. At the nanoscale (SEM picture, bar in right corner = 100 nm), individual clay particles are visible to form a nano-granular material. At a scale still below, one can see the layered structure of the shale particle.

The heterogeneities manifest themselves from the nanoscale to the macroscopic scale (see multiscale structure in Fig. 7-1), which all contribute to a large variety of shale macroscopic behavior.

7.1.1 Nano-Porosity and Clay Packing Density

The most prominent heterogeneity of shale materials is the nano-porosity, which is the pore space left in between clay sheets. It forms almost the totality of the porosity of shales, as poromercury intrusion studies show (Fig. 7-2), displaying a very low characteristic pore access radius of some nanometers. The total porosity of shales is typically determined by Mercury Porosimetry test. It is the pore space per unit of macroscopic volume, which includes not only

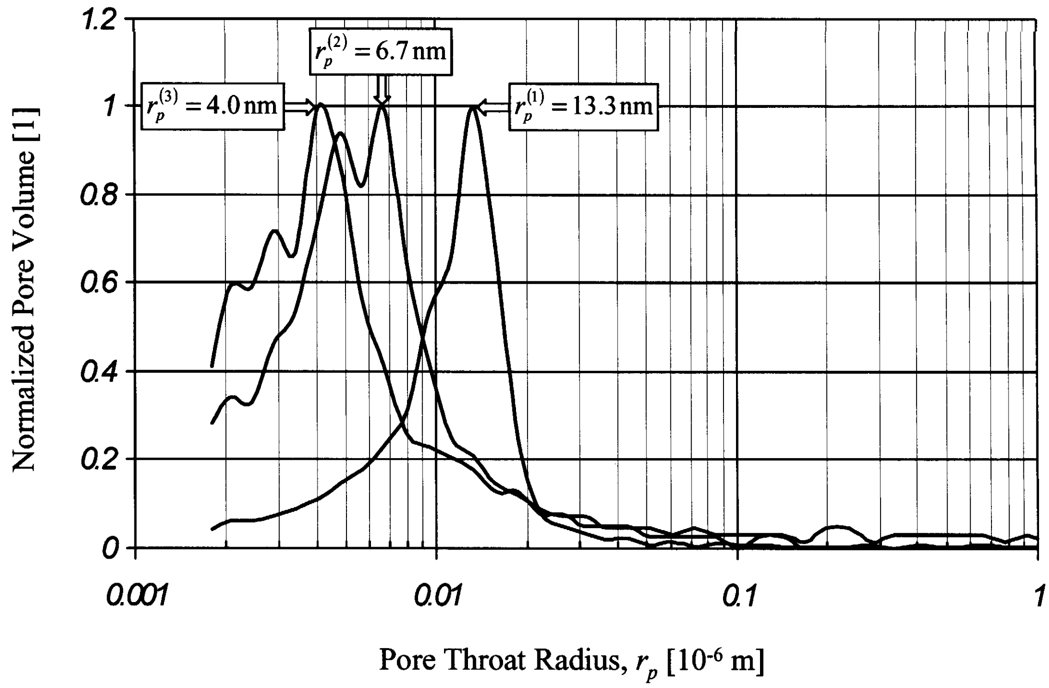

Figure 7-2: Pore throat radius distribution of shale materials obtained by poro mercury intrusion (PMI) (Source: ChevronTexaco, from [26]).

the clay material but as well non-clay silt inclusions. At this macroscopic scale, shale is a macroscopic composite material composed of a porous clay matrix with an in-general abundant population of poorly sorted detrital grains (mainly quartz inclusions), as shown in figure 7-3.

Hence, in order to determine the porosity in a reference volume consisting of the porous clay phase only, one needs to translate the total (measurable) porosity ϕ into the nano-porosity respectively the clay packing density by:

$$\varphi = \frac{\phi}{1 - f_I}; \; \eta = \frac{1 - f_I - \phi}{1 - f_I} \tag{7.1}$$

where f_I is the silt (non-clay) inclusion fraction which is known from mineralogy (namely X-Ray diffraction, for details, see [26]). To illustrate the difference, figure 7-4 plots the *shale* packing density $1 - \phi$ vs. *clay* packing density $\eta = 1 - \varphi$ for the six shale materials investigated here below. The presence of silt inclusions strongly enhances the packing density of these highly compacted materials.

7.1.2 Scale Separability Condition

The focus of our study is on the clay fabric of shale materials defined by the clay packing density η. In order to apply our multi-scale indentation yield design model (see Fig. 2-8), we must ensure that the charactersitic length scale that defines the clay fabric is much smaller than the size of an *rev* (if it can be defined!) which in turn needs to be smaller than the indentation depth (i.e. Eq. (2.22)). This is not an easy task[1], as a closer look on the microstructure of shale materials reveals (Fig. 7-5). The morphology is characterized by clay minerals that aggregate into a large variety of forms and shapes, ranging form highly ordered sheet bundles to wavy flake structures and highly pressed and crushed structures of clay sheets. These mineral aggregates have a characteristic size of 1,000 nm and a thickness of 100 – 250 nm. In short, the clay fabric is highly hetereogeneous. On the other hand, if we remind ourselves that the clay porosity has a charactersitic size of $\sim$ 10 nm (see Fig. 7-2), it is readily understood that the porosity of shales is situated at a scale below the heterogeneous clay composite that manifests itself at a

---

[1] Indeed, the scale separability condition for shale indentation is focus of the ongoing Ph.D. work of Chris Bobko in the Department of Civil and Environmental Engineering at M.I.T.

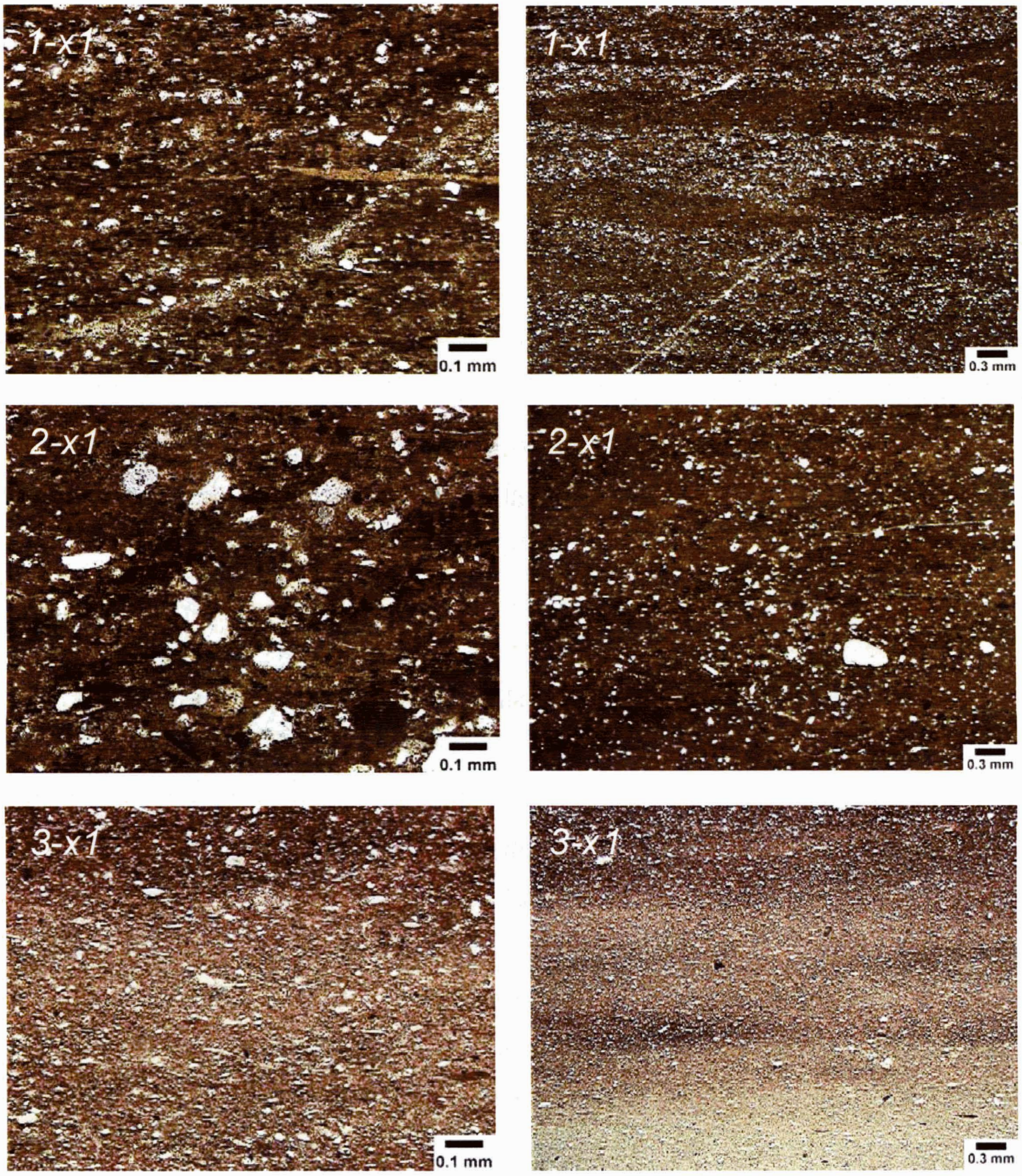

Figure 7-3: Plane polarized light thin-section photomicrographs, of 100X (left) and 25X (right) magnification, for three shale materials (Source: Chevron Texaco, from [26]).

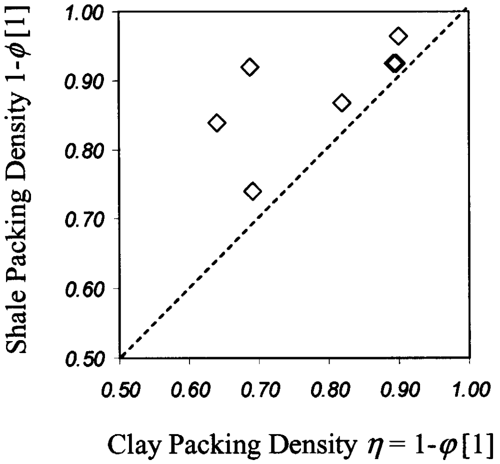

Figure 7-4: Shale packing density $1-\phi$ vs. clay packing density $\eta = 1-\varphi$. The higher shale density is due to silt inclusions.

length scale of $500 - 5,000\,\mathrm{nm}$. There are two important consequence for the application of nano-indentation:

1. The heterogeneous nature of the porous composite suggest the employment of a statistical indentation method, in order to gain access to average indentation properties of the porous clay composite. The grid-indentation technique developed by Constantinides and Ulm [23] (see Section 2.3) takes care of this aspect.
2. The fact that the size of the porosity is much smaller than the characteristic size of the clay fabric, allows us to apply our two-scale yield design approach for the extraction of strength properties of the clay particles.

7.2 Nanoindentation Analysis of Shale

Nanoindentation were performed on six shale materials from different sources, of different porosities and mineralogy. Chris Bobko performed the tests in the NanoMechanical Technology Laboratory of the Department of Materials Science and Engineering at M.I.T. during the Spring 2006, and analyzed the data statistically using the deconvolution method described

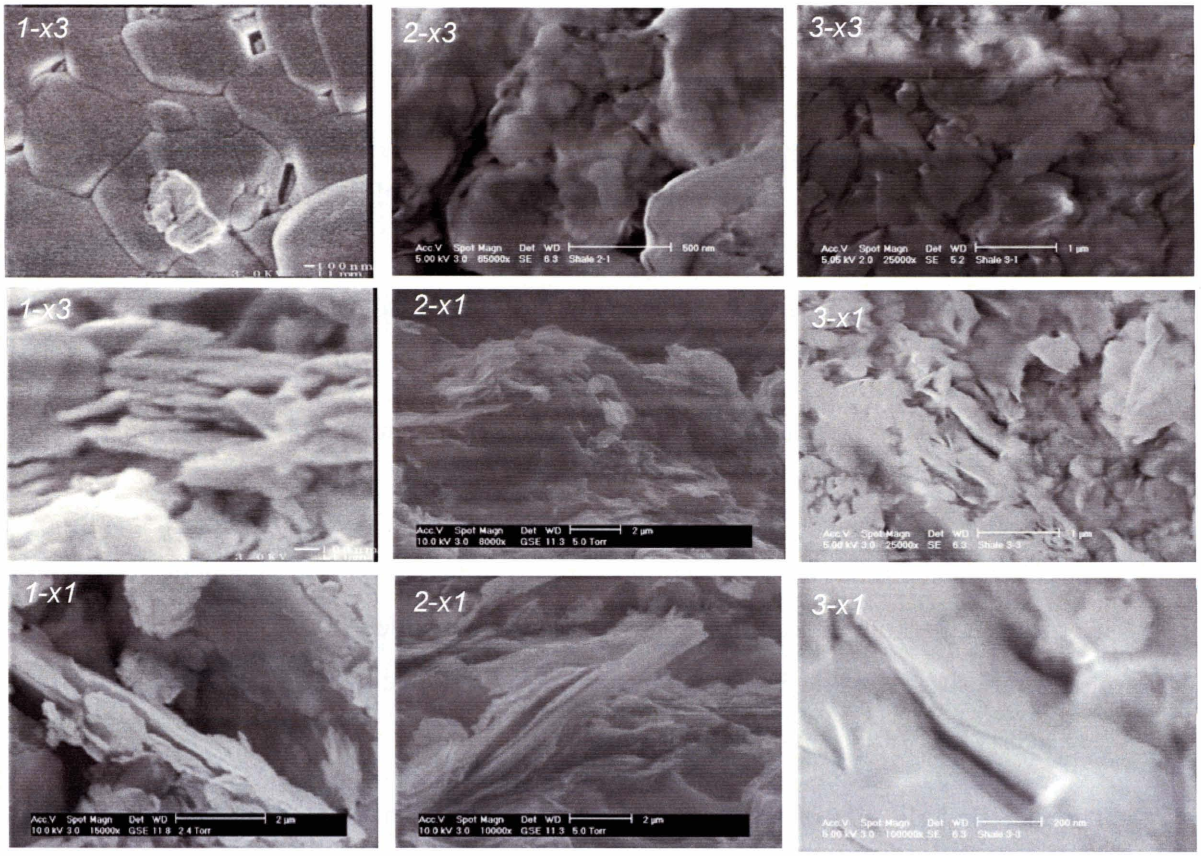

Figure 7-5: Clay fabric for 3 shale materials. Label $N - xi$ stands for shale $\#N$, and xi stands for the observation axis: $x3$ = view onto bedding plane; $x1, x2$ = view into bedding plane. (Source: [79])

in Section 2.3. Our contribution is the analysis of the hardness results.

7.2.1 Materials and Methods

Cylindrical shale specimens were cored in three perpendicular directions of shale cuttings, and stored in desiccators at their natural relative humidity until testing. For the indentation testing, the cylinder specimens were cut into slices of approximate thickness $5 - 10$ mm. The surfaces were ground and polished with silicon carbide papers and diamond particle suspension to obtain flat and smooth surface finish. Force driven nanoindentation tests were performed on the shale materials with a diamond Berkovich indenter using a Triboindenter of Hysitron Inc. By nanoindentation we refer to indentation tests operated to average indentation depths of $h = 100$ nm. Given the highly anisotropy of shales, nanoindenation test series were carried out in two directions: normal to bedding/deposition plane ($x3$) and in the bedding plane ($x1, x2$). Each indentation test series consisted of 300 tests on a surface carried out on three 10 x 10 grids of constant grid-size of $50,000\,\text{nm}$, which is sufficiently large that interactions between adjacent indents (of size $\sim 6h$) are avoided. In each test, the indentation force P and the indentation depth h was recorded for a loading, holding and unloading phase (see Fig. 2-1). The hardness H and the indentation modulus M were determined from the measured maximum force $P_{\max} = 285\,\mu\text{N}$ and the initial unloading slope $S = (dP/dh)_{h=h_{\max}}$ according to relations (2.1) and (2.2). The contact area A_c was estimated using the Oliver and Pharr method [55].

For each test series of 300 tests the indentation properties $(H, M\,(xi))$ were deconvoluted by a multi-Gaussian fit of the experimental frequency density (see Fig. 2-6). The result are characteristic mean values for indentation modulus M and hardness H of the clay fabric of the six shale materials in both normal-to-beddding and in-bedding directions. The repeatibility of the test procedure and statistical analysis method, and thus the statistical representativity of the results, was checked by several series of 100 indentation tests carried out on different specimen surfaces of the same shale sample.

7.2.2 Experimental Stiffness and Hardness Scaling

The results are presented in form of scaling relations of the indentation properties $H, M\left(x1\right), M\left(x3\right)$ vs. the clay packing density defined by (7.1). Figure 7-6 displays these plots and calls for the following comments:

1. The indentation modulus scaling in figure 7-6(a) provides evidence of the elastic anisotropy of the elastic content of the porous clay fabric: the indentation modulus in the bedding direction $M\left(x1\right)$ is consistently greater than $M\left(x3\right)$ corresponding to the indentation modulus normal to bedding. This is not surprising for highly compacted sedimentary rocks given their deposition history; and it is now generally agreed that shales behave elastically as transverse isotropic media [74],[45],[11],[75],[43],[64],[80],[61]. As a consequence the indentation modulus $M\left(x1\right) > M\left(x3\right)$. The link between $M\left(x1\right), M\left(x3\right)$ and the elasticity constants C_{ijkl} is given by Delafargue and Ulm's solution (2.14) and (2.15).
2. In sharp contrast, the experimental hardness scaling relation in figure 7-6(b) exhibits no anisotropy: hardness values (almost) take the same value in the direction of bedding $(x1)$ and normal to bedding $(x3)$. On first sight this result may come as a surprise given the pronounced anisotropy of the elasticity content of the clay fabric. On second thought, however, the isotropy of hardness hints towards the origin of the hardness, which relates exclusively to strength properties. Furthermore, from a more theoretical standpoint, these results validate the use of a yield design approach to link the hardness to strength properties. Indeed, the assumption of yield design theory is that a material system in its plastic limit state has exhausted its capacity to store externally supplied work rate (i.e. $P\overset{\circ}{h}$ in the case of indentation, see Section 3.1) into recoverable (i.e. elastic) energy. As a consequence, the work rate is entirely dissipated into heat form in the material system. This is the property we explored in the development of our upper bound model in Chapter 3 and 4. The isotropy of the hardness–packing density relation for shale, therefore, is a strong argument in favor of the application of yield design solutions for the extraction of strength properties.

3. The experimental scaling relations in figure 7-6 provide some evidence that the porous clay composite exhibits a percolation threshold around $\eta_0 \sim 1/2$, for which both indentation moduli $M(x1), M(x3)$ and the hardness H are expected to be close to zero. This particular behavior is a hallmark of granular materials, for which the random loose-packed limit (RLP) is known to be 52% [44], below which no continuous force path can be established through the granular assembly. In terms of microstructure, we readily find that this nanogranular nature is captured by a polycrystal morphology.

7.2.3 Reverse Analysis of Strength Properties

The aim of indentation analysis is to translate indentation data into meaningful material properties by means of a reverse analysis.

Technique

The indentation data at our disposal are 12 discrete values of the Berkovich hardness for a given clay packing density $\left(\eta_i, H_i^B\right)_{i=1..n}$, where $n = 12$ is the number of experimental hardness values. Furthermore, given the consistent scaling of the stiffness and hardness values in figure 7-6, a first-order engineering approach consists in assuming that all shale materials have the same solid properties (c^s, α) and the same micro-morphology captured by the percolation threshold η_0. Hence, the reverse analysis then consists of an inverse analysis in which the experimental values $\left(\eta_i, H_i^B\right)_{i=1..n}$ are the input and (c^s, α, η_0) the output. As sole tool of the reverse analysis, we use the fitting functions (6.14) and (6.16) of the hardness-to-cohesion ratio for Berkovich indentation for both the Mori-Tanaka scheme ($\eta_0 = 0$) and the Self-Consistent Scheme. The best fit is the one for which the quadratic error between experimental values and model is minimized, that is:

$$\begin{gathered}\min_{(c^s,\alpha,\eta_0)} \sum_{i=1}^{n} \left(H_i^B - H_{\eta_0}^B\left(c^s, \alpha, \eta_i\right)\right)^2 \\ s.t. \\ \max_{i=1,n} \eta_i \leq \eta^{\lim}\left(\alpha, \eta_0\right)\end{gathered} \tag{7.2}$$

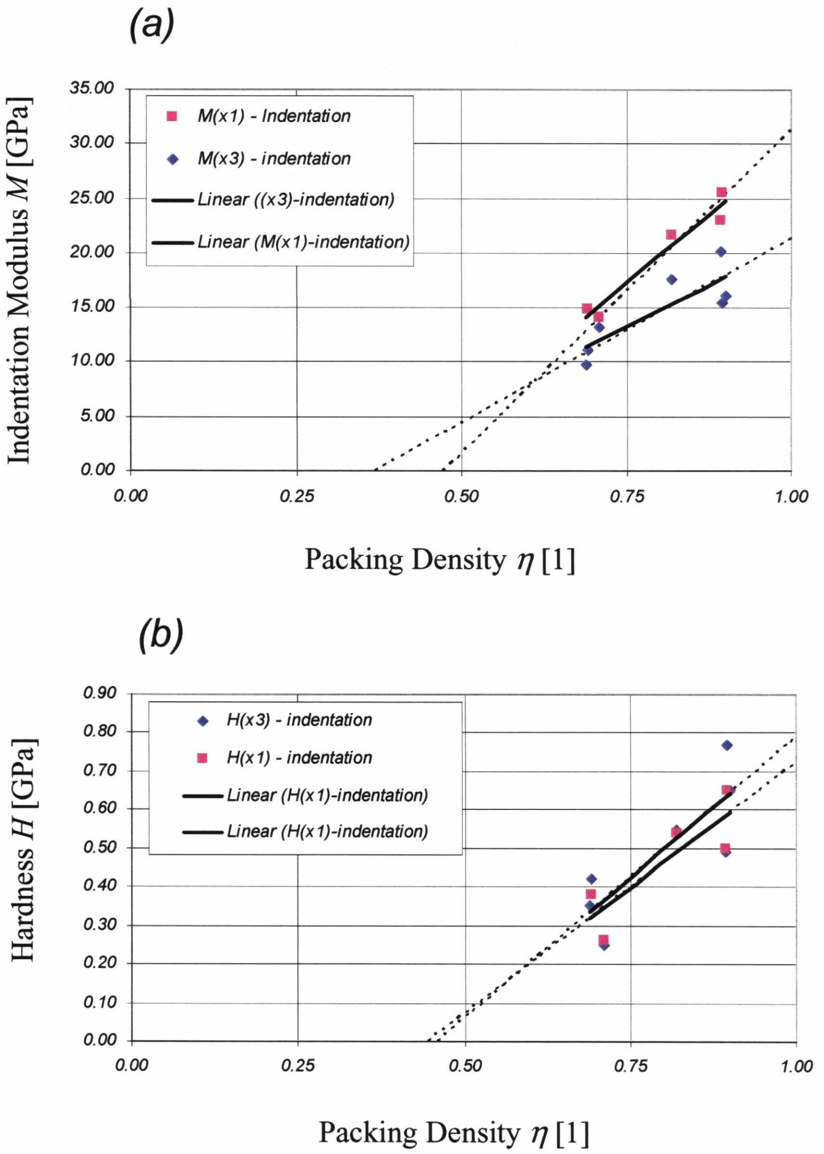

Figure 7-6: Scaling of (a) the indentation modulus, (b) the hardness as a function of the packing density for different shales in the indentation normal to bedding ($x3$) and parallel to bedding ($x1$).

	Mori-Tanaka	Self-Consistent
c^s [MPa]	92	255
α	0.444	0
$\eta^{\text{lim}}(\alpha, \eta_0)$	0.74	1
$\max_{i=1,n} \eta_i$	0.90	

Table 7.1: Geometrical relations between projected area and equivalent half-apex cone angle.

where $H^B_{\eta_0=0} = H^B_{mt}$ is given by (6.14) for the Mori-Tanaka Scheme:

$$H^B_{mt} = 12c^s\,(0.9833 + 1.7874\alpha)\,\eta \frac{30\alpha - 12\alpha\eta + 4\alpha^2\sqrt{8 - 5\eta} + (7 - 1.0593\eta)\sqrt{8 + 2.0739\eta}}{16\alpha^4 - 124\alpha^2 + 64\alpha^2\eta + 184 - 101.88\eta - 35.9218\eta^2} \tag{7.3}$$

and $H^B_{\eta_0=1/2} = H^B_{sc}$ is given by (6.16) for the Self-Consistent Scheme:

$$\begin{aligned} H^B_{sc} &= c^s \frac{12(1-\varphi)\left(3.549\,1\alpha^2 - 0.485\,\alpha + 0.995\,1\right)}{(64\varphi^2+16-64\varphi)\alpha^4 + (24\varphi^3 - 124\varphi^2 - 60 + 176\varphi)\alpha^2 + 557.60\varphi + 0.537\,\varphi^3 - 26.558\varphi^2 + 12.509} \\ &\cdot\left(\sqrt{(1-2\varphi)\,(0.179\,\varphi + 0.029\,81)}\,\left(4\,(1-2\varphi)\,\alpha^2 + 70.672\varphi + 30.099 + 3\varphi^2\right)\right. \\ &\left.+(1-2\varphi)\left(6\varphi^2 - 24\varphi + 18\right)\alpha\right) \end{aligned} \tag{7.4}$$

Results

Figure 7-7 shows the fitting of the experimental results to the Mori-Tanaka expression (7.3) and the Self-Consistent expression (7.4). In this fitting, the constraint condition $\eta \leq \eta^{\text{lim}}(\alpha, \eta_0)$ was not enforced. On first sight, therefore, it appears that both microstructural morphologies could fit the data equally well. The results are summarized in Table 7.1. However, if we check now the constraint condition $\max_{i=1,n} \eta_i \leq \eta^{\text{lim}}(\alpha, \eta_0)$, we readily find that only one of the two solutions can possibly fit the entire data set: the frictionless purely cohesive self-consistent scheme. This shows, for all practical applications, the importance of the limit packing density for the reverse analysis of strength properties of cohesive-frictional porous materials.

Finally, the corresponding uniaxial strength of the Von-Mises solid is $Y^s = 442$ MPa, corresponding to a Tresca (or Mohr-Coulomb) cohesion of $C^s = 221$ MPa.

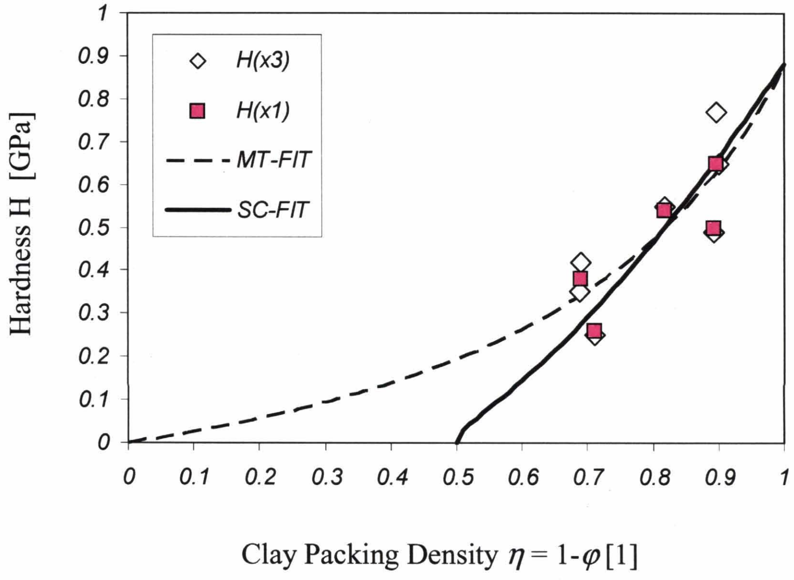

Figure 7-7: Fitting of experimental hardness values to hardness–packing density scaling for 6 shale materials (MT = Mori-Tanaka, SC = Self-Consistent)

7.3 Conclusion

To our knowledge, this is the first time that the clay fabric of shales was identified as a cohesive (no-friction) nanogranular material. On first sight, the no-friction behavior may come as a surprise given the frictional behavior of shale at the macroscale. On second thought, however, these nano-results are very consistent with the absence of anisotropy in the hardness behavior. In fact, if friction was activated at the particle-to-particle interface, the clay particle morphology would be expected to play a role. As we have seen, clay particles are of ellipsoidal to flat shape. In other words, the absence of friction explains why the hardness behavior of the clay fabric is isotropic.

Part V

Conclusions and Perspectives

Chapter 8

Summary of Results and Future Perspectives

Natural composites in general and sedimentary rocks in particular, are highly heterogeneous materials which defy a straightforward implementation of the materials science paradigm of processing (diagenesis)–microstructure–properties–performance correlation. The application of nanoindentation to natural composites has provided the geomechanics community with a new versatile tool to test in situ phase properties and structures of geomaterials that cannot be recapitulated ex situ in bulk form. But it requires a rigorous indentation analysis to translate indentation data into meaningful mechanical properties. The development and implementation of such an indentation analysis for the strength properties of cohesive-frictional porous materials is the overall achievement of our study. This last chapter provides a brief summary of our contributions and findings, and suggests some directions for future research.

8.1 Summary of Main Findings

The main finding of this thesis is that it is possible to condense the (conical) indentation hardness–material properties relation of cohesive-frictional porous materials into a single hardness-packing density scaling relation:

$$H = c^s \times \mathcal{F}\left(\eta, \eta_0, \eta^{\lim}, \theta\right) \tag{8.1}$$

where c^s is the solid's cohesion, $\eta = 1 - \varphi$ is the packing density of the solid phase; η_0 is the solid percolation threshold capturing the microstructure morphology ($\eta_0 = 0$ for a matrix–pore inclusion morphology, $\eta_0 = 1/2$ for a disordered polycrystal morphology); $\eta^{\lim} = \eta^{\lim}(\alpha, \eta_0)$ is the limit packing density, that is, for a given friction angle (α) and morphology of the solid (η_0), the maximum possible solid packing density a cohesive-frictional porous material can achieve; and finally θ is the half-apex angle of the cone. It is instructive to recall the steps we developed to establish and implement the hardness-packing density scaling relation (8.1):

1. Relation (8.1) was derived from an original multi-scale yield design approach to indentation analysis in Chapter 3, which recognizes the separation of scale condition. The approach translates recent progress in non-linear microporomechanics based on micro-yield design theory into a workable model for indentation analysis based on macro-yield design theory. The micro-yield design theory provides analytical expression for a cohesive Cam-Clay type elliptical strength criterion and of the associated dissipation function in functions of constituent properties (c^s, α) and microstructure parameters (η, η_0). The macro-yield design theory embeds this micro-macro dissipation function into the evaluation of the indentation hardness.

2. The computational implementation of the multi-scale yield design approach was based on an original discretization of the upper bound theorem in Chapter 4 and validated in Chapter 5. This novel approach recognizes the dissipation function of the elliptical (Cam-Clay type) strength criterion as a Second-Order Conic optimization problem. This identification opens the way for solving the problem by most advanced solver techniques, such as MOSEK. The originality of our approach lies in the combination of finite element discretization and advanced optimization techniques, which is readily implemented in standard tools of computational mechanics, such as MATLAB.

3. The application of our model in massive computational simulations presented in Chapter

6 showed that the hardness (8.1) of cohesive-frictional porous materials is less sensitive to the cone-angle θ as known for cohesive-frictional solids, and that the dominating feature is the scaling of the hardness with the packing density η. On this basis, it is possible to use the hardness-packing density scaling relation for reverse analysis of the strength parameters of cohesive-frictional porous materials. This was illustrated in Chapter 7 for shales. By fitting experimental nanohardness values for six shale materials of different packing density to the model hardness-packing relations, we showed (1) that the highly compacted porous clay fabric of shale materials is (most likely) composed of a frictionless purely cohesive solid phase which (2) is organized as a nanogranular material.

8.2 Research Contributions

The multi-scale indentation analysis we here propose extends previous approaches limited to the elastic properties to strength properties of cohesive-frictional porous materials. On the way, the following research contributions were made:

1. To the field of yield design, the identification of the upper bound approach for an elliptical strength criterion as a Second-Order Conic optimization problem is highly original. By introducing additional unknowns and additional cones, we developed a method that allows reducing the non-linear yield design problem to a minimization problem of a linear function subject to non-linear constraints and conical constraints. To our knowledge, this the first time that a yield design approach is solved in this manner.

2. To the rapidly developing field of nanoscale mechanical contact approaches such as nanoindentation, the reverse analysis of the indentation hardness by means of a multi-scale micromechanical model to predict constituent microstructure is an important contribution. The importance lies in the fact that it is now possible to separate constituent strength properties (c^s, α) from microstructure (η, η_0) in indentation analysis of porous materials. To our knowledge, this is the first time that the order of magnitude of strength properties of a solid phase can be assessed from an indentation test operated at larger scales. With progress in instrumented nanoindentation, the material scale that becomes accessible to

indentation strength property characterization and assessment is truly nanometric.

3. To the field of geomechanics in general and the GeoGenome project in particular, the identification of the clay fabric in highly compacted sedimentary rocks (such as shales) as a nanogranular frictionless material is of critical importance. On the one side, our contribution confirms that shales are nanogranular materials, an observation that was previously derived from the investigation of the anisotropic elastic behavior of shales. On the other hand, the finding that the clay nanofabric, from a strength perspective, is most likely frictionless thus isotropic opens the way for revisiting the sources of the macroscopic friction of shales.

8.3 Current Limitations and Future Perspectives

There are some inherent limitations of our approach which relate to the application of yield design for indentation analysis: One restriction of our approach relates to the assumption of the normality rule (or principle of maximum plastic work), which is at the very basis of the existence of the limit theorems of yield design, and which cannot capture an eventually non-associated flow behavior. From the perspective of dimensional analysis, the consideration of a non-associated flow rule adds additional independent quantities to the set of parameters in relations (8.1); but cannot be handled by the proposed yield design solution procedure in which the dilatation angle equals the friction angle. For such materials, advanced finite element simulations are required. In this case, the proposed approach can be used to determine initial values of the cohesion and friction angle for the iterative backanalysis. A similar remark can be made for contact friction and strain hardening effects, which we ignore in our yield design solutions. These effects appear to be negligible in the case of our shale material, since the hardness behaves isotropic in contrast to the pronounced elastic anisotropy, which one would expect to influence the hardening behavior as well.

It could also be (and has been) argued that yield design approaches as the one developed here cannot capture piling-up or sinking-in phenomena, as yield design evaluates the dissipation capacity of a materials system for a fixed geometry. Indeed, in our upper-bound simulations, we assumed the surface surrounding the indenter to be flat, which is far from what is observed on topographic images in indentation tests particularly for very sharp indenters like the Corner Cube. However, compared to the material bulk volume that contributes to the overall dissipation capacity, the additional contribution of the pile-up material volume is expected to be of second-order in the evaluation of the maximum dissipation the material system can afford. The good agreement of our yield design result with the ones obtained from comprehesive elastoplastic finite element analysis proofs this observation. Of course, the piling-up or sinking-in phenomena cannot be neglected in the evaluation of the hardness value from its definition (1.1), which is the input to the reverse analysis using hardness–packing density scaling relations of the form (8.1). Hence, like all indentation procedures, the successful determination of the strength properties from indentation tests relies on the determination of the correct projected contact area.

Our contribution is a modest yet important step forward towards a comprehensive multiscale approach to the strength behavior of geomaterials, which still needs to be achieved. For one, our hardness scaling relations need to be validated for some model materials, to fully appreciate their strength and limitations. Once achieved, it will be necessary to revisit the nanobehavior of shales and confirm the order of magnitude of the derived cohesion value of the nano-clay fabric, and foremost its frictionless nature. Immediately, new and innovative questions arise regarding the origin of the cohesive behavior of clay particles, the origin of the frictional behavior at larger scales, and so on. Once those questions will be solved, there is no doubt that progress in nanoscience and nanoengineering will translate into day-to-day engineering applications.

Part VI

Appendices

Bibliography

[1] Y. Abousleiman, F.-J. Ulm, GeoGenome Industry Consortium (G2IC), Research Proposal, Oklahoma University–M.I.T., 2004

[2] E. Anderheggen and H. Knopfel. Finite element limit analysis using linear programming. *International Journal of Solids and Structures*, 8, 1413-1431, 1972.

[3] G. I. Barenblatt. *Scaling.* Cambridge University Press, 2003.

[4] K.J. Bathe. *Finite element procedures.* Prentice Hall, Upper Saddle River, NJ, 1996.

[5] A. K. Bhattacharya and W. D. Nix. Analysis of elastic and plastic deformation associated with indentation testing of thin films on substrates. *International Journal of Solids and Structures*, 24(12), 1287-1298, 1988.

[6] F. M. Borodich, L. M. Keer, and C.S Korach. Analytical Study of Fundamental Nanoindentation Test Relations for Indenters of Non-Ideal Shapes. *Nanotechnology*, 14, 803-808, 2003.

[7] F. M. Borodich and L. M. Keer. Evaluation of elastic modulus of materials by adhesive (no-slip) nano-indentation. *Proceedings of the Royal Society of London. A*, 460, 507-514, 2004.

[8] A. Bottero, R. Negre, J. Pastor, and S. Turgeman.Finite element method and limit analysis theory for soil mechanics problems. *Computer methods in applied mechanics and engineering.* 22, 131-149, 1980.

[9] J. Boussinesq.*Applications des potentiels à l'étude de l'équilibre et du mouvement des solides élastiques.* Gauthier-Villars, 1885.

[10] J. A. Brinell. Mémoire sur les épreuves à bille en acier. In *Congres International des Méthodes d'Essai des Matériaux de Construction*, Paris, Tome 2, 83-94, 1901.

[11] J. Brittan, M. Warner, and G. Pratt. Short Note: Anisotropic parameters of layered media in terms of composite elastic properties. *Geophysics*, 60(4), 1243-1248, 1995.

[12] J.L. Bucaille, S. Stauss, E. Felder, and J. Michler. Determination of plastic properties of metals by instrumented indentation using different sharp indenters. *Acta Materialia.* 51, 1663-1678, 2003.

[13] H. Buckle in J.W. in Westbrook and H. Conrad, eds. The Science of Hardness Testing and its Applications. *American Society for Metals*, Metal Park OH, pp. 453-491, 1973.

[14] S.I. Bulychev, V. P. Alekhin, M. Kh. Shorshorov, A. P. Ternovskii, and G. D. Shnyrev. Determination of Youngs modulus according to an indentation diagram. (Ind. Lab. , Transl: Zavodskaya Laboratoria) 41, 1409-1412, cited from [6], 1975.

[15] N. Challoacoop, M. Dao, and S. Suresh. Depth-sensing instrumented indentation with dual sharp indenters. *Acta Materialia.* 51, 3713-3729, 2003.

[16] X. Chen, and J.J. Vlassak. Numerical study on the measurement of thin film mechanical properties by means of nanoindentation. *Journal of Materials Research* 16 (10): 2974-2982, 2001.

[17] Y. T. Cheng, and C. M. Cheng. Scaling, dimensional analysis, and indentation measurements. *Materials Science and Engineering* R44, 91-149, 2004.

[18] N.R. Chitkara and M.A. Butt. Numerical Construction of axisymmetric slip-line fiels for indentation of thick blocks by rigid conical indenters and friction at the tool-metal interface. *International Journal of Mechanical Science*, 34(11), 849–862, 1992.

[19] E. Christiansen. Computation of limit loads. *International Journal of Numerical Methods of Engineering.* 17: 1547-1570, 1981.

[20] H. Ciria Suarez. Computation of upper and lower bounds in limit analysis using second-order cone programming and mesh adaptivity, MIT-Dept. of Aeronautics and Astronautics, Thesis (S.M.), 2004. http://hdl.handle.net/1721.1/16655

[21] G. Constantinides, F.-J. Ulm, and K.J. van Vliet.On the use of nanoindentation for cementitious materials. *Materials and Structures* 205 (Special issue of Concrete Science and Engineering) RILEM, 191–196, 2003.

[22] G. Constantinides, and F.-J. Ulm. The effect of two types of C–S–H on the elasticity of cement-based materials: Results from nanoindentation and micromechanical modeling. *Cement and Concrete Research*, Vol. 34 (1), 67–80, 2004.

[23] G. Constantinides, and F.-J. Ulm. Invariant mechanical properties of calcium-silicate-hydrates in cement-based materials: instrumented nanoindentation and microporomechanical modeling, MIT-CEE Research Report, R05-03, Cambridge, MA, 2005.

[24] G. Constantinides, and F.-J. Ulm. The nanogranular nature of C-S-H. *Journal of the. Mechanics and Physics of Solids*, in Review, 2006.

[25] A. Delafargue, and F.-J. Ulm. Explicit approximations of the indentation modulus of elastically orthotropic solids for conical indenters. *International Journal of Solids and Structures*, 41, 7351–7360, 2004.

[26] A. Delafargue and F.-J. Ulm. Material invariant properties of shales: Nanoindentation and microporoelastic analysis, MIT-CEE Research Report (SM-Thesis), R04-02, Cambridge, MA, 2004.

[27] A. DiCarlo, H.T.Y. Yang and S. Chandrasekar. On the use of nanoindentation for cementitious materials. *Journal of Mechanics of Materials and Structures.* 36, 191-196, 2003.

[28] M. F. Doerner and W. D. Nix. A Method for Interpreting the Data from Depth-Sensing Indentation Instruments. *Journal of Materials Research* 1, 601-609, 1986.

[29] L. Dormieux, A. Molinari, and D. Kondo. Micromechanical approach to the behaviour of poroelastic materials. *Journal of the. Mechanics and Physics of Solids*, 50, 2203–2231, 2002.

[30] L. Dormieux, D. Kondo, and F.-J. Ulm. *Microporomechanics*, J. Wiley & Sons, In Press, 2006.

[31] K. Durst , M. Goken, and H. Vehoff. Finite element study for nanoindentation measurements on two-phase materials. *Journal of Materials Research* 19 (1): 85-93, 2004.

[32] H.A. Elliot. Axial symmetric stress distributions in aelotropic hexagonal crystals: The problem of the plane and related problems. *Mathematical Proceedings of the Cambridge Philosophical Society*, 45, 621–630, 1949.

[33] M. Fremond and J. Salençon. Limit analysis by finite element methods. In: A.C. Palmer, editor, *Proceedings of the Symposium on Role of Plasticity in Soil Mechanics,* Cambridge, UK, 1973.

[34] M. Futawaka, T. Wakui, Y. Tanabe, and I. Ioka. Indentification of the constitutive equation the indentation technique using plural indenters with different apex angles. *Journal of Materials Research.*16(8), 2283-2292, 2001.

[35] L. A. Galin. *Contact Problems in Theory of Elasticity.* Translated by H. Moss. In: Sneddon, I. N. (Ed.), North Carolina State College, 1951.

[36] F.P. Ganneau and F.-J. Ulm. From nanohardness to strength properties of cohesive-frictional Materials — Application to shale materials. MIT-CEE Research Report (SM-Thesis), R04-01, Cambridge, MA, 2004..

[37] F.P. Ganneau, G. Constantinides, and F.-J. Ulm. Dual-Indentation technique for the assesment of strength properties of cohesive-frictional material. *International Journal of Solids and Structures* 43, 1727-1745, 2004.

[38] H.J. Gao, C.H. Chiu, and J. Lee. Elastic contact versus indentation modeling of multilayered materials. *International Journal of Solids and Structures* 29 (20): 2471-2492, 1992.

[39] M. Gologanu, J.-B. Leblond, G. Perrin and J. Devaux. Recent extensions of Gurson's model for porous ductile metals in *Continuum Micromechanics.* P. Suquet, ed. Springer-Verlag pp. 61-130, 1997.

[40] M.T. Hanson. The elastic field for conical indentation including sliding friction for transverse isotropy. *Journal of Applied Mechanics.* 59, S123–S130, 1992.

[41] J. W. Harding and I. N. Sneddon. The elastic stress field produced by the indentation of the plane surface of a semi-infinite elastic solid by a rigid punch. *Mathematical Proceedings of the Cambridge Philosophical Society* 41, 16-26, 1945.

[42] H. Hertz. *On the contact of elastic solids* (in german), zeitschrift fur die reine und angewandte mathematik. English translation in miscellaneous papers (translated by D.E. Jones and G.A. Schott):99.146-62. Macmillan, London, UK, 1986, 92:156–71, 1881.

[43] B. Hornby. Experimantal laboratory determination of the dynamic elastic properties of wet, drained shales. *Journal of Geophysical Research*, 103 (12), 29945-29964, 1998.

[44] H.M. Jaeger, S. R. Nagel. Physics of granular state. *Science*, Vol. 255, No. 5051, 1523–1531, 1992.

[45] L.E.A. Jones and H.F. Wang. Ultrasonic velocities in Cretaceous shales from the Williston basin. *Geophysics*, 46, 288-297, 1994.

[46] K. L. Johnson. *Contact mechanics.* Cambridge University Press, Cambridge, UK, 1985.

[47] R.B King. Elastic analysis of some punch problems for a layered medium. *International Journal of Solids and Structures*, 23:1657-1664, 1987.

[48] K. Krabbenhoft, A.V. Lyamin, M. Hjiaj, and S.W. Sloan. A new discontinuous upper bound limit analysis formulation. *International Journal of Numerical Methods in Engineering*, 63, 1069-1088, 2005.

[49] J. Li and T.W. Chou. Elastic field of a thin-film/substrate system under an axisymmetric loading. *International Journal of Solids and Structures* 34(35-36): 4463-4478, 1997.

[50] F.J. Lockett. Indentation of a rigid/plastic material by a conical indentation. *Journal of the Mechanics and Physics of Solids*, 11(5), 345–355, 1963.

[51] A.E.H. Love. Boussinesq's problem for a rigid cone. *Quarterly Journal of Mathematics,* 10, 161-175, 1939.

[52] A.V. Lyamin and S.W. Sloan. Lower bound limit analysis using non-linear programming. *International Journal of Numerical Analysis Methods in Geomechanics*, 26, 181–216, 2002.

[53] A.V. Lyamin and S.W. Sloan. Upper bound limit analysis using linear finite elements and non-linear programming. *International Journal of Numerical Methods in Engineering*, 55, 573–611, 2002.

[54] L. Lysmer. Limit analysis of plane problems in soil mechanics. *ASCE Journal of the Soil Mechanics and Foundation Division*, 96, 1311–1334, 1970.

[55] W.C. Oliver and G.M. Pharr. An improved technique for determining hardness and elastic modulus using load and displacement sensing indentation experiments. *Journal of Materials Research*, 7(6), 1564–1583, 1992.

[56] W.C. Oliver and G.M. Pharr. Measurement of hardness and elastic modulus by instrumented indentation: Advances in understanding and refinements to methodology. *Journal of Materials Research*, 19(1), 3–20, 2004.

[57] J. Pastor. Application de l'analyse limite à l'etude de la stabilite des pentes et des talus. Ph.D. dissertation, USMG, Grenoble, France, 1976.

[58] J. Pastor and S. Turgeman. Mise en oeuvre numerique des methodes de l'analyse limite pour les materiaux de Von Mises et de Coulomb standards en deformation plane. *Mechanics Research Communications* 3, 469-476, 1976.

[59] J. Peng, C. Roos, and T. Terlaky. *Self-regularity: a new paradigm for primal-dual interior point algorithms.* Princeton, N.J. ; Oxford: Princeton University Press, c2002.

[60] A. Perriot and E. Barthel. Elastic contact to a coated half-space: Effective elastic modulus and real penetration. J*ournal of Materials Research*, 19 (2): 600-608, 2004.

[61] L.F. Pratson, A. Stroujkova, D. Herrick, F. Boadu, and P. Malin. Predicting seismic velocity and other rock properties from clay content only. *Geophysics*, 68(6), 1847-1856, 2003.

[62] J. Renegar. *A mathematical view of interior-point methods in convex optimization. Philadelphia.* PA: Society for Industrial and Applied Mathematics ; Mathematical Programming Society, 2001.

[63] J. Salençon. *Elasto-plasticité et calcul à la rupture.* Editions de l'Ecole Polytechnique, Palaiseau FR, 2001.

[64] C. Sayers. Stree-dependent seismic anisotropy of shales. *Geophysics*, 64(1), 93-98, 1999.

[65] S.W. Sloan. Lower bound limit analysis using finite elements and linear programming. *International Journal of Numerical Analysis Methods in Geomechanics*, 12, 61–77 1988.

[66] S.W. Sloan. A steepest edge active set algorithm for solving sparse linear programming problems. *International Journal of Numerical Analysis Methods in Geomechanics*, 12, 2671-2685, 1988.

[67] S.W. Sloan and P.W. Kleeman. Upper bound limit analysis with discontinuous velocity fields. *Computational Methods in Applied Mechanics and Engninnering*, 127, 293–314, 1995.

[68] I. Sneddon. The relation between load and penetration in the axisymmetric boussinesq problem for a punch of arbitrary profile. *International Journal of Engineering Science*, 3:47-57, 1965.

[69] P. Suquet. Plasticité et Homogénéisation. Thèse d'Etat, Université de Paris 6, 1982.

[70] P. Suquet. Effective properties of non-linear composites. In: P. Suquet, editor. *Continuum Micromechanics*, New York, Springer Verlag, 1997 (number 377 in CISM Courses and Lectures, pages 197-264).

[71] S. Swaddiwudhipong, K.K. Tho, Z.S. Liu, and K. Zeng. Material characterization based on dual indenters. *International Journal of Solids and Structures* 42, 69-83, 2005.

[72] D. Tabor. A simple theory of static and dynamic hardness. *Proceedings Royal Society*, A192, 247. (cited from [46]), 1948

[73] D. Tabor. *The hardness of metals.* Oxford classical texts in the physical sciences-First published 1951, 2000

[74] L. Thomsen. Weak elastic anisotropy. *Geophysics*, 52(10), 1954-1966, 1986.

[75] I. Tsvankin. P-wave signatures and notation for transversely isotropic media: An overview. *Geophysics*, 61, 467-483, 1996.

[76] S. Turgeman. Etude des fondations sollicitees a l'arrachement par la theorie de l'analyse limite. Ph.D. dissertation, USMG, Grenoble, France, 1976.

[77] F-J. Ulm and O. Coussy. *Mechanics and Durability of Solids, Volume I: Solid Mechanics.* MIT and Prentice Hall series on Civil, Environmental and Systems Engineering, Prentice Hall, Upper Saddle River, New Jersey, 2003.

[78] F.-J. Ulm, G. Constantinides and F.H. Heukamp. Is concrete a poromechanics material? – A multiscale investigation of poroelastic properties. *Materials and Structures* (Special issue of Concrete Science and Engineering), Vol. 37 (265), 43–58, 2004.

[79] F.J. Ulm, A. Delafargue, and G. Constantinides. Experimental microporomechanics. In: L. Dormieux and F.J. Ulm, editor. *Applied micromechanics of porous materials*, New York, Springer Verlag, 2004 (207-288).

[80] Z. Wang. Seismic anisotropy in sedimentary rocks. Part 1: A single plus laboratory method; Part 2: Laboratory data. *Geophysics*, 67(5), 1415-1422 (part I) and 1423-1440 (Part II), 2002.

[81] S.R. Williams. Hardness and hardness measurements. *American society of metals.* Cleveland, Ohio, 1942.

[82] H.Y.Yu, S.C. Sanday, and B.B. Rath. The effect of substrate in the elastic properties of films determined by the indentation test - Axisymmetric Boussinesq problem. *Journal of the Mechanics and Physics of Solids* 38 (6): 745-764, 1990.

[83] A. Zaoui. Continuum micromechanics: Survey. *Journal of Engineering Mechanics (ASCE)*, 128(8). 808–816, 2002.

[84] http://plato.asu.edu/topics/problems/nlores.html

[85] www.mosek.com

Appendix A

Background on Yield Design Theory

A.1 On The ‘Duality’ of the Lower and Upper Bound Approach

A.1.1 Mathematical Formulation

Let Ω denote the domain of study. Let $\underline{U} = \underline{U}(\underline{x})$ be a plastic velocity field that belongs to a space Y^{KA} of kinematically admissible velocity fields. $Y^{KA} \subseteq Y$, where Y is the space of all the velocity fields. Likewise, let $\boldsymbol{\sigma} = \boldsymbol{\sigma}(\underline{x})$ be a stress field belonging to the space of statistically admissible stress tensors X^{SA}. $X^{SA} \subseteq X$, where X is the space of all the symmetric stress tensors. Let $\underline{Q}(\boldsymbol{\sigma})$ be the load vector and $\underline{q}(\underline{U})$ the associated velocity vector, such that the external work rate is $\delta W = \underline{Q}(\boldsymbol{\sigma}) \cdot \underline{q}(\underline{U})$. The generalized divergence theorem informs us that,

$$\begin{gathered} \forall \boldsymbol{\sigma} \in X^{SA}, \forall \underline{U} \in Y^{KA}, \\ \int_{\Omega} (\boldsymbol{\sigma} : \mathbf{d})\, d\Omega + \int_{\Sigma_U} [\underline{U}] \cdot \boldsymbol{\sigma} \cdot \underline{n}\, da = \underline{Q}(\boldsymbol{\sigma}) \cdot \underline{q}(\underline{U}) \end{gathered} \tag{A.1}$$

where Σ_U stands for surfaces of discontinuity, while $\mathbf{d}$ is the strain rate gradient:

$$\mathbf{d} = \frac{1}{2} \left(grad\, \underline{U} + grad^T\, \underline{U} \right) \tag{A.2}$$

The applications

$$\begin{cases} \boldsymbol{\sigma} \rightarrow \underline{Q}(\boldsymbol{\sigma}) \\ \underline{U} \rightarrow \underline{q}(\underline{U}) \end{cases} \tag{A.3}$$

are linear. Let $a(\boldsymbol{\sigma},\underline{U})$ denote

$$a(\boldsymbol{\sigma},\underline{U}) = \int_{\Omega} (\boldsymbol{\sigma} : \mathbf{d})\, d\Omega + \int_{\Sigma_U} [\underline{U}] \cdot \boldsymbol{\sigma} \cdot \underline{n}\, da \tag{A.4}$$

Let G be the convex set of admissible stresses, i.e. the set of statistically admissible stress satisfying the yield criterion. Finally, define

$$C^{KA} = \{\underline{U} \in Y^{KA} \mid \underline{q}(\underline{U})() = \underline{1}\} \tag{A.5}$$

A.1.2 Dual Definition of the Exact Limit Load

The exact limit load results from solving any of the following problems (A.6) [20]:

$$\begin{aligned}
\underline{Q}^{\text{lim}} &= \sup \underline{Q} \text{ s.t.} \left\{ \begin{array}{l} \exists \boldsymbol{\sigma} \in G \\ \int_{\Omega} (\boldsymbol{\sigma} : \mathbf{d})\, d\Omega + \int_{\Sigma_U} [\underline{U}] \cdot \boldsymbol{\sigma} \cdot \underline{n}\, da = \underline{Q}(\boldsymbol{\sigma}) \cdot \underline{q}(\underline{U}), \forall \underline{U} \in Y^{KA} \end{array} \right. && \text{(A.6a)} \\
&= \sup_{\boldsymbol{\sigma} \in G} \inf_{\underline{U} \in C^{KA}} a(\boldsymbol{\sigma},\underline{U}) && \text{(A.6b)} \\
&= \inf_{\underline{U} \in C^{KA}} \sup_{\boldsymbol{\sigma} \in G} a(\boldsymbol{\sigma},\underline{U}) && \text{(A.6c)} \\
&= \inf_{\underline{U} \in C^{KA}} D(\underline{U}) && \text{(A.6d)}
\end{aligned}$$

where $D(\underline{U}) = \sup_{\sigma \in G} a(\sigma,\underline{U})$.

Problem (a) is called static principle of limit analysis and is a lower bound approach. Problem (d) is called kinematic principle of limit analysis and is an upper bound approach. These two problems are dual to each other: the same limit load will be obtained from both the static and the kinematic principles. The limit load $\underline{Q}^{\text{lim}}$ only depends on the choice of the mathematical model of the strength domain with consistent approximations for both methods and does not depend on the method of solution used (lower or upper bound). The limit load will be obtained through the lower approach if the strength criterion is satisfied everywhere and if the external loads are such that equilibrium conditions are nowhere violated. The same limit load will be obtained through the upper bound approach if the velocity field is kinematically admissible. The velocity field describes the collapse mechanism whereas the stress field corresponds to a state of admissible stresses satisfying the strength criterion.

A.1.3 Properties of the Dual Formulations

The two problems (a) and (d) in (A.6) are 'dual' to each other. There are two major results relating the primal and dual problems. The first, called 'weak' duality, states that the primal objective values provide bounds for the dual objective values, and vice versa. The second major result relating the primal and dual problems is called 'strong' duality and states that the optimal values of the primal and dual problems are equal, provided that they exist.

The equality between (b) and (c) in (A.6) precisely follows from strong duality. The proof is given in detail in [19]. The paper also shows that the limit fields $\boldsymbol{\sigma}^{\mathrm{lim}}$ and $\underline{U}^{\mathrm{lim}}$ exist and are a saddle point of $(\boldsymbol{\sigma}, \underline{U}) \rightarrow a(\boldsymbol{\sigma}, \underline{U})$.

Since $(\boldsymbol{\sigma}^{\mathrm{lim}}, \underline{U}^{\mathrm{lim}})$ satisfies the saddle-point condition, then for any $\underline{U}' \in C$ and $\boldsymbol{\sigma}' \in G$

$$a(\boldsymbol{\sigma}', \underline{U}^{\mathrm{lim}}) \leq a(\boldsymbol{\sigma}^{\mathrm{lim}}, \underline{U}^{\mathrm{lim}}) \leq a(\boldsymbol{\sigma}^{\mathrm{lim}}, \underline{U}') \tag{A.7}$$

A.2 The Dissipation Functions 'Π'

In Chapter 3, we have introduced and heavily employed the concept of 'dissipation functions' as a dual definition of the strength domain of a material. This Appendix provides some background on the properties of the dissipation functions. First, let us note the following relation:

$$\Pi(\underline{x}, n(\underline{x}), [\mathbf{U}(\underline{x})]) = \frac{1}{2}\Pi(\underline{x}, n(\underline{x}) \otimes [\mathbf{U}(\underline{x})] + [\mathbf{U}(\underline{x})] \otimes n(\underline{x})) \tag{A.8}$$

As a consequence, $\underline{x} \rightarrow \Pi(\underline{x}, n(\underline{x}), [\mathbf{U}(\underline{x})])$ can be expressed as a function of $\underline{x} \rightarrow \Pi(\underline{x}, \mathbf{D}(\underline{x}))$. Therefore, in the following, we will focus on $\underline{x} \rightarrow \Pi(\underline{x}, \mathbf{D}(\underline{x}))$ and present some properties:

- If the convex strength domain $G(\underline{x})$ is bounded in the $\mathbb{R}^6$ stress space, the 'sup' is in fact a 'max' which means:

$$\Pi(\underline{x}, \mathbf{D}(\underline{x})) = \mathbf{\Sigma}^*(\underline{x}) : \mathbf{D}(\underline{x}) \tag{A.9}$$

  where $\mathbf{\Sigma}^*(\underline{x})$ is a stress field on the boundary of $G(\underline{x})$, where the external normal is

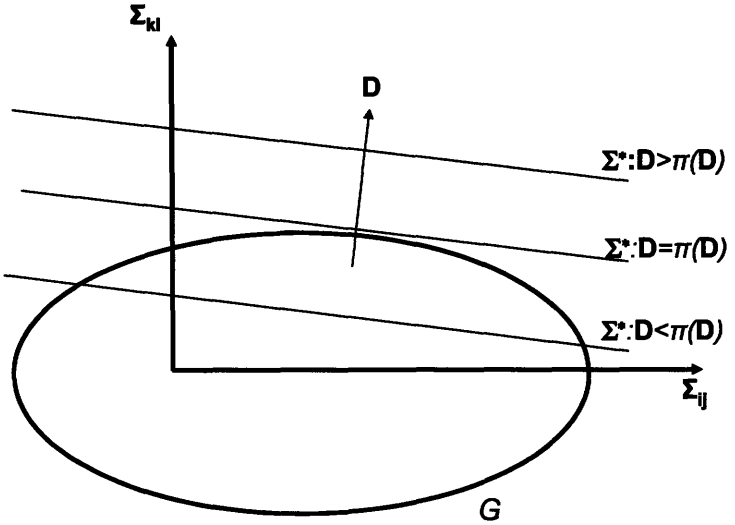

Figure A-1: Presentation of the flow rule.

parallel to **D** and of same direction. The proof is as follows: For a given value of **D**, the condition $\mathbf{\Sigma} : \mathbf{D} = \Pi(\mathbf{D})$ appears as the equation of a hyperplane in the stress space and this hyperplane is tangent to the boundary ∂G at point $\mathbf{\Sigma}^*$ where the normal to ∂G is parallel to **D**, as shown in Fig. A-1. If $G(\underline{x})$ is strictly convex, $\mathbf{\Sigma}^*(\underline{x})$ is unique.

- If the convex domain $G(\underline{x})$ is not bounded in every directions of $\mathbb{R}^6$, $\Pi(\underline{x}, \mathbf{D}(\underline{x}))$ can take an infinite value $+\infty$.
- $\Pi(\underline{x}, .)$ is a convex function of $\mathbf{D}(\underline{x})$.
- $\Pi(\underline{x}, .)$ is non negative since $\mathbf{\Sigma}(\underline{x}) = 0 \in G(\underline{x})$ implies $\forall \mathbf{D}(\underline{x}), \Pi(\underline{x}, \mathbf{D}(\underline{x})) \geq 0$.
- $\Pi(\underline{x}, .)$ is positively homogeneous of degree $\kappa = 1$ with regard to $\mathbf{D}(\underline{x})$ since

$$\forall \mathbf{D}(\underline{x}), \forall \lambda \in \mathbb{R}^+, \Pi(\underline{x}, \lambda \mathbf{D}(\underline{x})) = \lambda \Pi(\underline{x}, \mathbf{D}(\underline{x})) \tag{A.10}$$

We have evoked this property in Section 2.1.2 dealing with the self-similarity of the indentation test.

Appendix B

Some Elements of Optimization Theory

This Appendix provides some background on optimization theory. Our focus is not to be exhaustive, but rather to introduce some vocabulary that complements our developments in Chapter 4, and which turns out useful for our study. First, we will define the notion of primal-dual formulation for a problem. Then, we will see what a primal-dual feasible solution is. And last, we will present two resolution methods: the Simplex Method and the Interior Point Method. The presentation is inspired by Refs. [59] and [62].

B.1 Primal-Dual Formulation of a Problem

In optimization theory, any convex optimization problem has a dual counterpart whose variables are different from those of the original problem but whose solution, i.e. the optimal value of the objective function, is the same as the one of the original problem. The original problem is called 'primal' and the equivalent problem is called 'dual'.

For instance, in the case of a standard SOCO problem (see Section 4.3.2), the primal formulation is:

$$\text{(SOCO)} \qquad \begin{array}{l} \min c^T x \\ Ax = b \end{array}$$

$x \in K$

and its dual form is:

(SOCD) $\max b^T y$

$A^T y + s = c$

$s \in K$

When there is 'strong duality' between these two problems, the solution of the primal problem is equal to the solution of the dual problem.

These two formulations for the same problem are important, especially when there is strong duality, both from a theoretical point of view and from a computational point of view. From a theoretical point of view, the primal-dual formulation implies that an initial problem written in one particular formulation can be written in an equivalent 'dual' formulation, which offers the advantage to suggest another approach, maybe easier, to solve the same problem. From a computing point of view, an optimization solver can use both formulations to converge easier and faster toward the unique solution. This property is used, for example, by the solver MOSEK introduced in Section 4.4.

B.2 Primal-Dual Feasibility of a Solution

Since the solution of the primal problem is not necessarily the solution of the dual problem, it is interesting to define what the term 'solution' means. Indeed, a 'solution' can be characterized in several manners:

First, a solution vector is said 'feasible' when it satisfies the constraints.

Then, a solution vector is said 'optimal' when it is both feasible and optimal (obtaining the largest or smallest objective value).

In the general case, if x is a feasible point for the primal problem, and y a feasible point for the dual problem, then the two problems are said to satisfy a 'weak' duality, which means that:

$$c^T x \geq b^T y \tag{B.1}$$

In some particular cases, the two problems satisfy a 'strong' duality. This states that the optimal values of the primal and dual problems are equal, provided that they exist. In such a situation, the solution is said 'primal-dual feasible'.

To illustrate this vocabulary, consider a standard Linear Optimization problem:

- A point x is said to be feasible (or strictly feasible) for (LPrimal) if $Ax = b$ and $x \geq 0$ (or $x > 0$).
- A point (y, s) is feasible (or strictly feasible) for (LDual) if $A^T y + s = c$ and $s \geq 0$ (or $s > 0$).

In the particular case of a Linear Optimization problem, the following property is always satisfied:

If x and (y, s) are feasible for (LP) and (LD), respectively, then necessarily the point (x, y, s) is primal-dual feasible (i.e. an optimal solution).

A similar property holds for the case of a Second-Order Conic problem:

If both:

- *(SOCO) is strictly feasible, that is, there exists an $x \in \mathbb{R}^n$ such that $Ax = b$, $x \in K$*
- *(SOCD) is strictly feasible, that is, there exists $s \in \mathbb{R}^n$, $y \in \mathbb{R}^m$ such that $A^T y + s = c$, $s \in K$*

then we have a pair of optimal solutions x^*, (y^*, s^*) with $c^T x^* = b^T y^*$.

We keep in mind for both a linear optimization problem and a second-order conic problem, that there is strong duality between the primal and the dual formulations, which means that the optimal values are equal for both formulations, provided that they exist.

B.3 Solution Methods

This Section provides some more details on solution methods. Since we have just defined what a solution is, we are now presenting briefly two methods of convergence toward the solution when it exists.

B.3.1 Simplex Method

Linear Optimization deals with a simple mathematical model that exhibits a combination of two contrasting aspects: it can be considered as both a continuous and a combinatorial problem. The continuity of the problem is to find a global minimizer of a continuous linear function over a continuous convex polyhedral constrained set, and its combinatorial character is to look for optimality over a set of vertices of a polyhedron. The Simplex algorithm, invented by Dantzig in the mid-1940s, explicitly explores its combinatorial structure to identify the solution by moving from one vertex to an adjacent one of the feasible set with improving values of the objective function.

More explicitly, the Simplex Method observes that the solution set of a linear program is convex, which means that the solution set of a linear program of n variables can be represented as a convex polygon in n-space. Furthermore, it observes that if a maximum or minimum value of the solution exists, it will exist at a corner of this polygonal region. Proving this last characteristic can be done as follows. Since each of the n variables has a linear relationship with the solution, each variable has a minimum effect at one extreme of one of its constraints and a maximum at the other extreme, with either a non-decreasing or a non-increasing effect in between. Therefore, any solution found away from a corner can be translated along at least one variable, while either increasing or decreasing the solution's value, until the solution set border is reached. The process can always be repeated until a corner of the solution set is encountered. This process is illustrated in Fig. B-1. Therefore, the Simplex algorithm begins at an arbitrary corner of the solution set. At each iteration, the Simplex Method selects the variable that will produce the largest change towards the minimum (or maximum) solution. That variable replaces one of its compatriots that is most severely restricting it, thus moving the Simplex Method to a different corner of the solution set and closer to the final solution. In addition, the Simplex Method can determine if no solution actually exists. Note that the algorithm selects the best choice at each iteration without needing information from previous or future iterations.

On the other hand, the Simplex Method must visit every corner of the solution set in order to find the minimum or maximum values. In particular, if the solution set involves many variables,

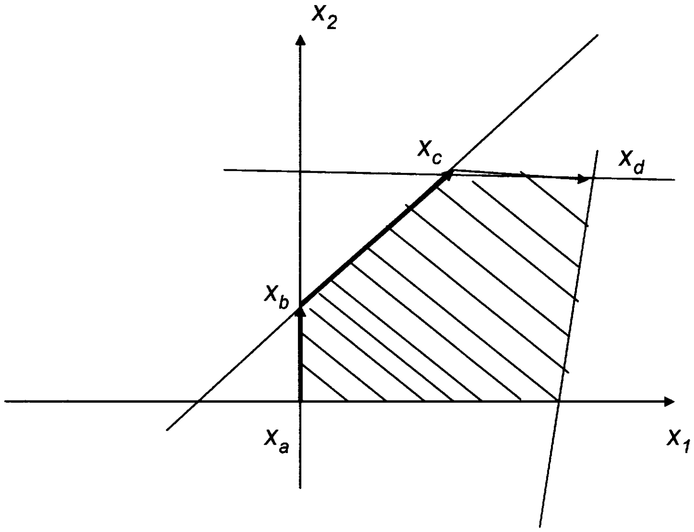

Figure B-1: Simplex procedure.

this search could take an extended period of time and involve a large number of computations.

B.3.2 Interior Point Method

The Simplex Method has been the main method to solve Linear Problem until very recently. The new area of Interior-Point Method started in 1984 when Karmakar proposed his LO algorithm. The theory of IPMs developed into a mature principle during the 1990s, when algorithm for LO were transparently extended to more complex problems such as nonlinear convex programming, semi-definite optimization (SDO) and second-order conic optimization (SOCO). IPMs are now widely considered since, while problems such as LO can also be solved by other methods (an IPM is only one alternative), IPMs appear to be the first and also most efficient approach for SDO. SDO and IPM are today a very active area of mathematical programming.

Appendix C

Simulation Data

This Appendix gathers the simulation data obtained with the solver MOSEK.

$\varphi\backslash\alpha$	0	0.05	0.1	0.15	0.2	0.25	0.3	0.35	0.4	0.45	0.5
0	5.37										
0.1	3.46	3.00	4.61	5.35	6.24	7.33					
0.2	2.30	2.61	3.03	3.57	4.20	4.95	5.85	6.97			
0.3	1.69	1.87	2.10	2.39	2.79	3.33	3.97	4.73	5.65	6.82	
0.4	1.29	1.40	1.54	1.71	1.94	2.23	2.64	3.19	3.82	4.59	5.55
0.5	0.98	1.06	1.15	1.26	1.39	1.56	1.79	2.10	2.54	3.06	3.70
0.6	0.73	0.78	0.84	0.91	0.99	1.10	1.23	1.40	1.64	1.97	2.40
0.7	0.52	0.55	0.59	0.63	0.68	0.74	0.82	0.92	1.04	1.21	1.46
0.8	0.33	0.34	0.37	0.39	0.42	0.45	0.50	0.55	0.61	0.70	0.81
0.9	0.16	0.16	0.17	0.18	0.20	0.21	0.23	0.25	0.28	0.31	0.35

Table C.1: Simulation values of the hardness-to-cohesion ratio for the flat punch and the Mori Tanaka scheme.

$\varphi\backslash\alpha$	0	0.5	0.1	0.15	0.2	0.25	0.3	0.35	0.4	0.45	0.5
0	4.90										
0.1	3.33	3.77	4.29	4.90	5.62	6.49					
0.2	2.28	2.59	2.97	3.42	3.94	4.55	5.29	6.18			
0.3	1.69	1.86	2.08	2.37	2.75	3.19	3.71	4.33	5.08	5.00	
0.4	1.29	1.40	1.53	1.70	1.92	2.21	2.58	3.021	3.54	4.17	4.93
0.5	0.98	1.05	1.14	1.25	1.38	1.55	1.77	2.07	2.43	2.86	3.37
0.6	0.73	0.78	0.84	0.91	0.99	1.09	1.22	1.39	1.62	1.91	2.25
0.7	0.52	0.55	0.58	0.63	0.68	0.74	0.81	0.91	1.03	1.20	1.42
0.8	0.33	0.34	0.37	0.39	0.42	0.45	0.49	0.54	0.61	0.69	0.80
0.9	0.16	0.16	0.17	0.18	0.20	0.21	0.23	0.25	0.27	0.31	0.35

Table C.2: Simulation values of the hardness-to-cohesion ratio for the Berkovich and the Mori Tanaka scheme.

$\varphi\backslash\alpha$	0	0.05	0.1	0.15	0.2	0.25	0.3	0.35	0.4	0.45	0.5
0	4.38										
0.1	3.07	3.42	3.81	4.27	4.80						
0.2	2.24	2.49	2.79	3.13	3.52	3.98	4.51	5.14			
0.3	1.68	1.84	2.05	2.29	2.58	2.91	3.30	3.76	4.29	4.94	
0.4	1.28	1.39	1.52	1.69	1.89	2.12	2.40	2.73	3.11	3.56	4.10
0.5	0.98	1.05	1.14	1.24	1.37	1.53	1.72	1.95	2.22	2.53	2.90
0.6	0.73	0.78	0.84	0.90	0.98	1.08	1.21	1.36	1.54	1.75	2.00
0.7	0.52	0.55	0.58	0.63	0.68	0.74	0.816	0.90	1.01	1.15	1.31
0.8	0.33	0.35	0.37	0.39	0.42	0.45	0.49	0.54	0.60	0.68	0.77
0.9	0.16	0.17	0.17	0.18	0.20	0.21	0.23	0.25	0.27	0.30	0.34

Table C.3: Simulation values of the hardness-to-cohesion ratio for the cube corner and the Mori Tanaka scheme.

$\varphi\backslash\alpha$	0	0.05	0.1	0.15	0.2	0.25	0.3	0.35	0.4	0.45	0.5
0	5.36										
0.05	4.24	4.85	5.57	6.45	7.51						
0.1	3.22	3.74	4.33	5.02	5.86	6.88	8.15				
0.15	2.42	2.74	3.18	3.75	4.40	5.17	6.11	7.23			
0.2	1.90	2.10	2.34	2.66	3.09	3.68	4.37	5.19	6.18	7.42	
0.25	1.52	1.64	1.79	1.97	2.20	2.49	2.89	3.44	4.12	4.93	5.90
0.3	1.21	1.29	1.37	1.48	1.60	1.76	1.94	2.19	2.50	2.94	3.54
0.35	0.94	0.99	1.04	1.101	1.17	1.25	1.34	1.45	1.58	1.74	1.95
0.4	0.70	0.72	0.75	0.78	0.82	0.85	0.899	0.94	0.99	1.05	1.12
0.45	0.45	0.46	0.47	0.48	0.50	0.51	0.52	0.54	0.56	0.57	0.59

Table C.4: Simulation values of the hardness-to-cohesion ratio for the flat punch and the self consistent scheme.

$\varphi\backslash\alpha$	0	0.05	0.1	0.15	0.2	0.25	0.3	0.35	0.4	0.45	0.5
0	4.90										
0.05	3.97	4.48	5.08	5.79	6.65						
0.1	3.14	3.57	4.06	4.64	5.32	6.14					
0.15	2.40	2.72	3.12	3.59	4.13	4.76	5.52	6.44			
0.2	1.89	2.08	2.33	2.64	3.05	3.53	4.10	4.77	5.57	6.55	
0.25	1.51	1.63	1.78	1.96	2.18	2.47	2.86	3.33	3.88	4.53	5.32
0.3	1.20	1.28	1.37	1.47	1.60	1.75	1.93	2.17	2.48	2.89	3.38
0.35	0.94	0.99	1.04	1.10	1.16	1.24	1.33	1.44	1.576	1.73	1.93
0.4	0.70	0.72	0.75	0.78	0.81	0.85	0.89	0.94	0.99	1.05	1.12
0.45	0.45	0.46	0.47	0.48	0.49	0.51	0.52	0.54	0.55	0.57	0.59

Table C.5: Simulation values of the hardness-to-cohesion ratio for the Berkovich and the self consistent scheme.

$\varphi\backslash\alpha$	0	0.05	0.1	0.15	0.2	0.25	0.3	0.35	0.4	0.45	0.5
0	4.38										
0.05	3.57	3.96	4.41	4.94	5.55						
0.1	2.93	3.27	3.65	4.08	4.59	5.18	5.89				
0.15	2.36	2.62	2.93	3.28	3.69	4.17	4.72	5.37			
0.2	1.88	2.07	2.29	2.56	2.87	3.23	3.66	4.15	4.73	5.41	
0.25	1.51	1.63	1.77	1.94	2.15	2.41	2.71	3.06	3.47	3.95	4.51
0.3	1.21	1.28	1.37	1.47	1.592	1.74	1.92	2.13	2.39	2.70	3.06
0.35	0.95	0.99	1.048	1.10	1.17	1.24	1.33	1.44	1.56	1.72	1.90
0.4	0.70	0.73	0.75	0.78	0.82	0.85	0.89	0.94	0.99	1.05	1.12
0.45	0.45	0.46	0.47	0.49	0.50	0.51	0.53	0.54	0.56	0.57	0.59

Table C.6: Simulation values of the hardness-to-cohesion ratio for the cube corner and the self consistent scheme.

η^{lim}	H/c^s
0.999999	4.90
0.9966	5.40
0.9865	5.89
0.9698	6.33
0.9462	6.65
0.9163	7.05
0.8795	7.03
0.8362	7.09
0.7862	6.96
0.7294	6.69
0.6659	6.30

Table C.7: Simulation values of the hardness-to-cohesion ratio at the limit packing density for the Berkovich and the Mori Tanaka scheme.

η^{lim}	H/c^s
0.999999	4.38
0.9966	4.65
0.9866	5.01
0.9699	5.32
0.9465	5.57
0.9166	5.74
0.8799	5.82
0.8366	5.82
0.7866	5.71
0.7299	5.47
0.6666	5.26

Table C.8: Simulation values of the hardness-to-cohesion ratio at the limit packing density for the cube corner and the Mori Tanaka scheme.

η^{lim}	H/c^s
0.999999	4.90
0.9966	5.40
0.9869	5.89
0.9713	6.46
0.9508	6.68
0.9267	6.98
0.9003	7.17
0.8725	7.29
0.8445	7.34
0.8172	7.34
0.7907	7.27

Table C.9: Simulation values of the hardness-to-cohesion ratio at the limit packing density for the Berkovich and the self consistent scheme.

η^{lim}	H/c^s
0.999999	4.38
0.9966	4.64
0.9869	5.01
0.9714	5.33
0.951	5.58
0.927	5.79
0.9005	5.92
0.8728	6.11
0.8448	6.04
0.8174	6.01
0.7912	5.94

Table C.10: Simulation values of the hardness-to-cohesion ratio at the limit packing density for the cube corner and the self consistent scheme.